University of Ioannina

School of Natural Sciences

Physics Department

Optical potential and reaction mechanisms of weakly bound nuclei at near barrier energies

Author:
Konstantina Zerva

Supervisor:
Prof. Athina Pakou

October 2013

ΥΠΟΥΡΓΕΙΟ ΠΑΙΔΕΙΑΣ ΚΑΙ ΘΡΗΣΚΕΥΜΑΤΩΝ
ΕΙΔΙΚΗ ΥΠΗΡΕΣΙΑ ΔΙΑΧΕΙΡΙΣΗΣ

Με τη συγχρηματοδότηση της Ελλάδας και της Ευρωπαϊκής Ένωσης

MINISTRY OF EDUCATION & RELIGIOUS AFFAIRS
MANAGING AUTHORITY

Co- financed by Greece and the European Union

Advisory committee:

1. **Athina Pakou**
   Professor
   Physics Department
   University of Ioannina

2. **Nikolaos Alamanos**
   Professor
   Research Director CEA Saclay (IRFU)
   France

3. **Nikolaos Manthos**
   Associate Professor
   Physics Department
   University of Ioannina

Review committee:

1. **Professor Athina Pakou - Univ. of Ioannina**

2. **Professor Nikolaos Alamanos - CEA Saclay**

3. **Associate Professor Nikolaos Manthos - Univ. of Ioannina**

4. **Proffesor Roza Vlastou - NTUA**

5. **Associate Professor Efstathios Stiliaris - Univ. of Athens**

6. **Associate professor Xenofon Aslanoglou - Univ. of Ioannina**

7. **Assistant professor Konstantinos Ioannidis - Univ. of Ioannina**

Acknowledgement

I would like to express my gratitude to all the people who have supported and assisted me during my PhD studies.

Professor of Nuclear Physics A. Pakou, my supervisor, for her guidance throughout my studies, for suggesting the subject, introducing me to the appropriate experimental and theoretical techniques and for supporting my efforts during my studies. Also the members of the advisory committee Professor Nikolaos Alamanos and Associate professor Nikolaos Manthos for the assistance they provided.

I would like to express the deepest appreciation to all the people for their substantial contribution to these experiments. From NCSR DEMOKRITOS Dr. Anastasios Lagogiannis, from NTUA (National Technical University) Associate professor Michalis Kokoris, from UOI (University of Ioannina) the Associate proffesor Xenofon Aslanoglou and especialy the Assistant professor Nicolas Patronis. I extend my sincere and warm thanks to all the members of the group of Proffesor Lattuada of INFN - LNS and Univesity of Catania and especially to Dr. Pier-Paolo Figueira, Dr. Alecia di Pietro and Dr. Agatino Musumara and to the people of EXOTIC Group Dr. Marco Mazzocco, Dr. Marco La Commara, Dr. Mauro Romoli and especially Dr. Dimitra Pierroutsakou. Also to Dr. Tudor Glodariou and Dr. Dan Filipescu from "Horia Hulubei" National Institute of Physics and Nuclear Engineering of Romania and Dr. Angel M. Sanchez-Benitez from the Uninersity of Huelva, Spain.

I warmly thank the directors of the NCSR DEMOKRITOS and LNS Laboratoties for making available the facilities for the needs of our experiments and especially the LNL for their generous hospitality in the dormitories of the laboratory during our staying. I would also like to thank their technical staff for providing good beams and for the support with electronics and the acquisition. Their help was more than useful.

In addition, my great appreciation to Proffesor K. Rusek for introducing my to the calculations with FRESCO CODE as well as Dr. N. Keeley for the theoretical support.

Also the members of the review committee for reading extensively this work and for the critical comments and corrections that they made.

Last but not least I would like to thank my parents Ioulia and Dimimtios and my sister Persephoni for supporting my efforts all these years and never stopped to have faith on me. My life partner Georgios Sidiropoulos for his support, his love and his patience all these years. My warmest appreciation to my close friends Panagiota Giannaka, Christos Soutzios, Athanasios Eptaimeros and Yvonne Evaggelou who were of great support and proved tolerant of my grumpiness. Many thanks to fellow team members Vasilis Soukeras and Akis Sgouros for their collaborative and friendly spirit.

This research has been co-financed by the European Union (European Social Fund ESF) and Greek national funds through the Operational Program "Education and Lifelong Learning" of the National Strategic Reference Framework (NSRF) - Research Funding Program: Heracleitus II. Investing in knowledge society through the European Social Fund.

Abstract

The main aim of this work is to systematically probe the energy dependence of the optical potential at sub- and near barrier energies for weakly bound projectiles on various targets. It refers to the study of elastic backscattering of the ^{6}Li and ^{7}Li on ^{28}Si, ^{58}Ni, ^{120}Sn and ^{208}Pb targets at near barrier energies, namely at 5 to 11 MeV for ^{28}Si, 9 to 20 MeV for ^{58}Ni, 12 to 26 MeV for ^{120}Sn and 18 to 36 MeV for ^{208}Pb and the establishment of this technique as a tool for probing the optical potential.

The optical potential, at energies well above the barrier, is nearly energy independent. But approaching the vicinity of the Coulomb barrier an anomalous behavior is observed. For well bound nuclei the imaginary part of the optical potential, $W(E)$, sharply decreases while the real part, $V(E)$, presents a localized peak. This effect is described as potential threshold anomaly. Moving to weakly bound nuclei the situation becomes more complicated due to the influence of breakup and/or transfer effects.

The conventional method to determine the optical potential is elastic scattering through angular distribution measurements. But in this energy region the fits to the potential parameters are not adequately sensitive, since the nuclear part of potential is very weak in comparison to the Coulomb part. In order to improve our understanding on the energy dependence of the potential, especially at sub-barrier energies, and the relevant processes involved in the threshold anomaly, other complementary means should be adopted.

As an alternative method, we have proposed in this study the elastic backscattering barrier distribution technique. Barrier distributions of elastic scattering, can be obtained via first derivatives as follows:

$$D_{el}(E) = -\frac{d}{dE}\Big[\sqrt{\frac{\sigma_{el}(\theta)}{\sigma_{Ruth}(\theta)}}(E)\Big] \tag{1}$$

As this quantity depends on the derivative of differential elastic scattering cross sections, even a small change in the potential has a substantial effect on the barrier distribution.

In this work two experiments were performed. The first experiment, for the system $^{6,7}Li + {}^{28}Si$, took place at the Tandem Accelerator Laboratory in the Institute of Nuclear Physics of the National Center for Scientific Research "Demokritos". The second one, for the systems $^{6,7}Li + {}^{58}Ni$, ^{120}Sn and ^{208}Pb, was performed at the Laboratori Nazionali del Sud (LNS) of the Instituto Nazionale di Fisica Nucleare in Catania. A beam of $^{6,7}Li^{3+}$ ions were delivered by the accelerators, bombarded the various targets which were placed perpendicular to the beam direction, and the various ejectiles were collected by detectors at backward angles. In more detail, for the first experiments single silicon detectors were used, mounted at ± 150 and ± 170 degrees

relevant to the beam direction, while for the second two stage telescopes were used, mounted at ±160 and ±170 degrees. Single silicon detectors were mounted at forward angles (±20 degrees), where the scattering is pure Rutherford, and they were used for normalization purposes.

The spectra analysis was performed with the code PAW (Physics Analysis Workstation). The identification of the elastic peak was made by taking into account the energy calibration, the kinematics and the energy loss of the colliding ions in the target. Excitation functions of measured cross sections versus Rutherford were determined by the following formula

$$\frac{\sigma_{backward}(\theta)}{\sigma_{bRuth}(\theta)} = \frac{N_b}{N_f}\frac{\Omega_f}{\Omega_b}\frac{\sigma_{fRuth}(\theta)}{\sigma_{bRuth}(\theta)} \tag{2}$$

where N_f and N_b are the (quasi-)elastic scattering total counts in the forward and backward detectors, Ω_f and Ω_b are their respective solid angles and $\sigma_{fRuth}(\theta)$, $\sigma_{bRuth}(\theta)$ are known Rutherford cross sections at the angle θ. The ratio of solid angles was determined in a separate run with a heavy target and at low energy, where scattering is purely of Rutherford type. Finally, the relevant barrier distributions were formed by relation (1) and were compared with calculated values in an optical model analysis.

The optical-model analysis for probing the optical potential as a function of energy was accomplished by using for the real and imaginary part a BDM3Y1 interaction. It was assumed that the interaction has the same radial dependence for the two parts of the optical potential, but with different normalization factors. For the folding procedure, density distributions for the target nuclei were taken from electron scattering data in a conventional two- or three-parameter Fermi model. A phenomenological model according to Bray and Hartree Fock calculations was adopted for the densities of the projectiles ^6Li and ^7Li, respectively. The code ECIS was used for calculating the differential cross sections at backward angles and for reanalyzing elastic scattering differential cross-sections of previous measurements. The starting point in the optical model theoretical analysis was the imaginary potential which follows the linear segment model (as proposed by Satchler). The real potential is calculated via dispersion relations. Subsequently, the potential was fed in ECIS code and the elastic backscattering excitation functions were determined by forming ratio of elastic scattering cross section over Rutherford. Finally, barrier distributions were calculated according to relation (1) and compared with the experimental data.

Moreover, our potentials were tested on elastic scattering fusion and transfer DWBA (Distorted Wave Born Approximation) calculations. Finally, for the completeness of this work and for probing the reaction mechanisms, Continuum Discretized Coupled Channel (CDCC) calculations are presented for all the systems by using the code FRESCO. These calculations were performed by Professor K. Rusek.

The following conclusions were drawn from this work: The behavior of

weakly bound projectiles like ^6Li and ^7Li at near sub-barrier energies contrasts that of well bound ones. The main difference refers to a strong absorption which occurs till very low sub-barrier energies. A new type of threshold anomaly is observed for ^6Li and another for ^7Li. In the case of ^6Li the imaginary potential presents an increasing trend at the energy range where for well bound ones a potential drop occurs. The rising part has the largest slope for the heavier targets and the smallest slope for the lighter ones, possibly indicating in a qualitative interpretation that the competition between breakup and transfer or some compound procedure at energies at the barrier is in favor of breakup. The imaginary part drops to zero at very low energies creating a big bump in the real part, unexpected under physical conditions. This fact puts on stake the validity of the dispersion relation.

For ^7Li, while the imaginary potential presents a decreasing trend from higher to lower energies similar to the one associated with well bound projectiles, the fall of the potential does not occur at barrier but at very low sub-barrier energies. While our analysis presents strong indication for a breakdown of the conventional threshold anomaly, is not sensitive enough to distinguish between a potential obeying the dispersion relation and one which does not, although the trend is in favor of the second scenario.

From the point of view of reaction mechanisms, breakup seems to be the strong concept for creating the new type threshold anomaly without however to exclude contributions from transfer channels. Full CRC calculations (Coupled Reaction Channel) may clarify this issue but which are beyond the scope of this work.

Contents

Introduction

This work is part of the curriculum of the Postgraduate Program of the Department of Physics, University of Ioannina. The research area belongs to the basic direction of Nuclear Physics and in particular in the area of Nuclear Reactions.

The interaction between two nuclei is one of the most important aspects in nuclear physics. But even in the case of the elastic scattering, the description of this interaction is prohibitively complicated. All the nucleons of the target nucleus interact with each other and with the nucleons of the incident nucleus, and each individual nucleon-nucleon interaction contains central exchange and tensor components. A simplified answer to this problem can be given by the optical model, which approximates the complicated many body problem by a two-body potential between the incident nucleus and the target nucleus. The detailed structures of the target and the incident nuclei are ignored. The optical potential can be expressed by a real and imaginary part, the last describing the absorption of the incident flux from the elastic channel into other nonelastic channels. [1, 2, 3]. Both parts can be described by a simple function of the radial distance r.

At energies well above the Coulomb barrier both terms of the optical potential are nearly energy independent. This picture no longer remains valid when approaching the vicinity of the Coulomb barrier. In this case a rapid variation of the optical model parameters around the Coulomb barrier is observed which is visualized as a localized peak in the strength of the real potential, associated with a sharp decrease in the strength of the imaginary potential as it becomes more and more unimportant to remove flux from the reaction in this low energy region. This behavior, known as potential threshold anomaly [4, 5, 6], is attributed to a strong coupling between the elastic and the other channels. As the collision energy is lowered, reaction channels such as inelastic scattering, nucleon or cluster transfer, fusion and fission become effectively less important. Couplings of these reaction channels may produce polarization potentials of different signs, attractive or repulsive, that dynamically decrease or increase the Coulomb barrier [6, 7, 8, 9]. The link between the real and imaginary parts of the polarization potential is given by dispersion relations which have been shown to be a manifestation of the principle of causality [5, 6, 10].

Over the last decade, considerable interest has been focused on the energy dependence of the optical potential at sub- and near-barrier energies for reactions involving weakly bound stable nuclei [11, 12, 13, 14, 15, 16, 17, 18, 19, 20, 21, 22, 23, 24, 25, 26, 27, 28, 29, 30, 31, 32, 33]. This interest is due to the fact that the study of the energy dependence of the nuclear optical potential at near barrier energies is one of the tools to investigate the influence of the breakup, nucleon transfer and other reaction mechanisms upon the elastic and fusion channels [7, 26, 34, 35, 36, 37, 38, 39, 40]. It

is believed that the polarization potential which is produced by the break up, as it is repulsive in nature, will compensate the attractive term of the potential $\Delta V (V = V_0 + \Delta V)$ which is connected through a dispersion relation with the imaginary part and which is responsible for the anomaly [17, 41]. Otherwise, as it is suggested by Satchler [4], the dispersion relation may be of no use for weakly bound systems, since according to theoretical calculations [42, 43], the repulsive contribution of the real part of the potential, is almost independent of beam energy while the associated imaginary potential is very small.

The presence or a possible absence of the so-called "break-up threshold anomaly" is a question of paramount importance. It may challenge the current theoretical understanding of low-energy reaction dynamics involving weakly bound nuclei and modify the current understanding of the genesis and production rate of some nuclei produced in stellar explosions. Therefore, efforts should be intensified in order to determine the potential till very low energies, the main ingredient for predicting safely reaction cross-sections. However, two are the main inherent difficulties in such studies performed at low energies. The lack of sensitivity for obtaining the optical potential parameters, via conventional techniques, and the strong couplings to transfer and breakup which alter the view of the well-known potential for tightly bound nuclei. Variations on the ratio of transfer versus breakup from target to target for weakly bound projectiles may be reflected as variations on the energy trend of the optical potential. Such a case was already reported as a possibility by Lubian et al. [8] via polarization potential calculations.

The traditional tool for deducing the optical potential is the elastic scattering. However at low energies the sensitivity of the fits on the potential parameter during the minimization process of calculated values to experimental data is very low due to the large Coulomb potential in respect to the nuclear one. For further understanding this subject and being able to energy map the potential, other complementary means to the conventional techniques should be also adopted. As such, the application of elastic backscattering [44] via barrier distributions is proposed in this work. The role of backscattering, via excitation functions, for probing properties of the optical potential and the structure of the involved nuclei has been extensively demonstrated in recent years [45, 46, 47, 48, 49, 50, 51, 52]. It is the first time however that this technique combined with barrier distribution is proposed for energy mapping the optical potential.

In this respect, we study in this work the energy dependence of the optical potential at near and sub-barrier energies. Excitation functions of elastic backscattering are determined and barrier distributions are formed and are used as a tool for probing the new type potential threshold anomaly for weakly bound nuclei, and for extending the energy dependence of the optical potential at sub-barrier energies. The goal of this work is to systematically probe the potential and the importance of coupling effects at near and sub-

barrier energies of weakly bound nuclei, namely $^{6,7}Li$, on light, medium and heavy targets, namely on ^{28}Si, ^{58}Ni, $^{116,120}Sn$ and ^{208}Pb. Two isotopes for Sn were chosen for testing the isotope dependence. Other measurements of elastic and quasi-elastic backscattering barrier distributions for weakly bound nuclei have been reported previously for heavy targets: $^{6,7}Li + ^{208}Pb$ [53], $^{6}Li + ^{144,146}Sm$ [54, 55] and $^{6}Li + ^{232}Th$ [56] with the emphasis however, on the coupling effects rather than the energy dependence of the optical potential. The choice of almost spherical targets in the present case was based mainly on the intention to probe the potential without any strong interference from the structure of the involved nuclei.

The data were collected in the Tandem Accelerator Laboratory in the Institute of Nuclear Physics of the National Center for Scientific Research "Demokritos" and in the Laboratori Nazionali del Sud (LNS) of the Instituto Nazionale di Fisica Nucleare in Catania. The analysis of the experimental data and the theoretical analysis relevant to the optical potential, fusion and transfer calculations, was completed at the Nuclear Physics Laboratory (NPL) - Ioannina. Further more elaborated calculations in the CDCC approach were performed by Prof. K. Rusek from the University of Warsaw and are presented here for reasons of completeness. The present work consists of the following chapters:

- Chapter 1: Includes some theoretical aspects on nuclear reactions. It describes the formal scattering theory by a central potential and the optical model which is used to simplify the scattering problem. Then, the dispersion relations and the barrier distributions are discussed.

- Chapter 2: Includes details of the experimental setup's, the detectors and the electronics which are used.

- Chapter 3: Includes the data reduction, where the experimental excitation functions and the corresponding barrier distributions are presented.

- Chapter 4: Includes the theoretical analysis where they are presented the results of the optical potentials for all the systems. Moreover some fusion, DWBA and CDCC calculations are also presented.

- Chapter 5: Includes conclusive remarks and discussion of the results.

Chapter 1

Theory

1.1 Introduction to Nuclear Reactions

1.1.1 Types of reactions

A nuclear reaction can be defined as a collision between two nuclei that produces a change in the nuclear composition and/or the energy state of the interacting nuclei. In most cases, the formed nuclei are different from the initial ones. In order for the reaction to take place, the interacting particles need to approach each other at distances of the order of the nuclear dimensions ($10^{-15}m$). In the usual experimental situation, nuclear reactions are initiated by energetic particles from an accelerator and in some cases from a reactor which fall upon bulk matter. A typical nuclear reaction is written:

$$a + X \rightarrow Y + b \qquad \text{or} \qquad X(a,b)Y \tag{1.1}$$

where a is the accelerated projectile, X is the target nucleus and Y, b are the reaction products. Usually, Y is a heavy product that stops in the target and is not directly observed, while b is a light particle that can be detected and measured [57].

Reactions can be classified in various ways:

- **Scattering process:** the incident and outgoing particles are the same. This process is taken as *elastic* if Y and b are in their ground states so that $Q = 0$ and *inelastic* if Y or/and b is in an excited state.
- **Knockout reaction:** the reaction may result in more than two products. The projectile remain unchanged ($a = b$) but the reaction causes yet another nucleon (usually neutron or proton) to be ejected separately.
- **Transfer reaction:** one or two nucleons are transfered between projectile and target, therefore adding one nucleon to the target X to form

Y and vice versa.

Reactions can also be classified by the mechanism that governs the process.

- **Direct reactions:** in which only very few nucleons take part in the reaction, with the remaining nucleons and the target serving as passive spectators. The incident particle interacts in a time comparable to the time taken to transit the nucleus, about $10^{-22}s$.
- **Compound nucleus mechanism:** the incoming and target nuclei merge briefly for a complete sharing of energy before the outgoing nucleon is ejected. The average lifetime of a compound nucleus is $10^{-15} - 10^{-16}s$.
- **Resonance reactions:** are between direct and compound reactions, in which the incoming particle forms a "quasi-bound" state before the outgoing particle is ejected.

1.1.2 Q value

Q value, for a nuclear reaction, is the amount of energy released by that reaction. Is defined as the initial mass energy minus the final mass energy.

$$Q = (m_{initial} - m_{final})c^2 = (m_X + m_a - m_Y - m_b)c^2 \tag{1.2}$$

which is the same as the excess kinetic energy of the final products.

$$Q = T_{final} - T_{initial} = T_Y + T_b - T_X - T_a \tag{1.3}$$

The Q value may be positive, negative or zero. A reaction with a positive Q value is exothermic; on this case nuclear mass or binding energy is released as kinetic energy of the final products. A reaction with a negative Q value is endothermic and the initial kinetic energy is converted into nuclear mass or binding energy [57]. An endothermic reaction takes place only if the projectile energy exceeds a threshold

$$E_{th} = Q\frac{m_X + m_a}{m_Y} \tag{1.4}$$

1.1.3 Coulomb barrier

All the particles involved in a usual nuclear reaction are positively charged and hence repel each other, with the exception of neutrons. The Coulomb barrier, is the energy barrier due to electrostatic interaction, that

projectile needs to overcome or to tunnel through in order to undergo a nuclear reaction. This energy barrier is given by the electrostatic potential energy:

$$U_{coul} = \frac{1}{4\pi\epsilon_0}\frac{Z_1 Z_2 e^2}{r} \tag{1.5}$$

where Z_1, Z_2 are the corresponding atomic numbers of the projectile and the target, e is the elementary charge and r is the interaction radius.

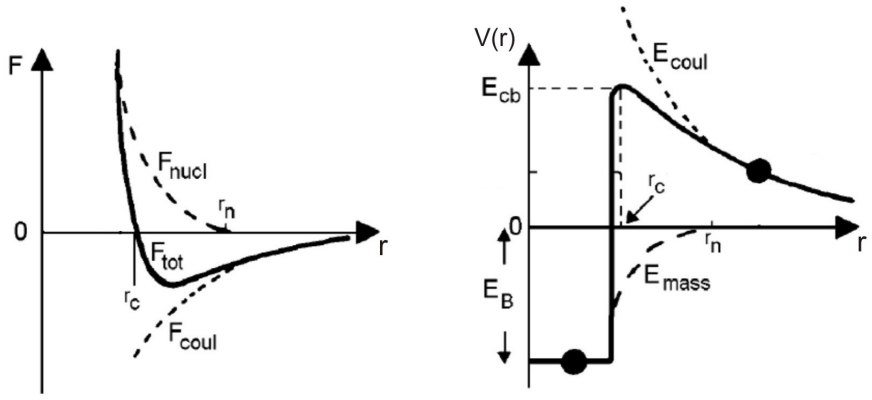

Figure 1.1: *Forces and energy conditions when a charged projectile reacts with a target nucleus*

As shown in figure 1.1 at a distance greater than r_n only the Coulomb repulsive force is in operation; however, for distances less than r_n both the attractive nuclear force F_{nucl} and the repulsive Coulomb force act upon the system. At some particular distance designated r_c, the forces balance each other and at shorter distances the attractive nuclear force dominates. The distance r_c is known as the Coulomb radius; is the sum of the projectile and target radii.

1.1.4 Reaction cross section

The reaction probability is expressed in terms of a quantity known as cross section and denoted by σ. The quantity σ, which has the dimension of an area (1 barn= $10^{-24} cm^2$), is measured by the experimental ratio:

$$\sigma = \frac{\text{Rate of emitted reaction particles}}{(\text{number of beam particles / unit time})(\text{number of target nuclei / unit area})} \tag{1.6}$$

Consider a typical reaction $A(a,b)B$. If there is a flux of I_a projectile particles per unit time incident on a target containing N nuclei per unit area of type A, then the number of particles b emitted is proportional to both I_a and N. The constant of proportionality is the cross-section σ. If the outgoing

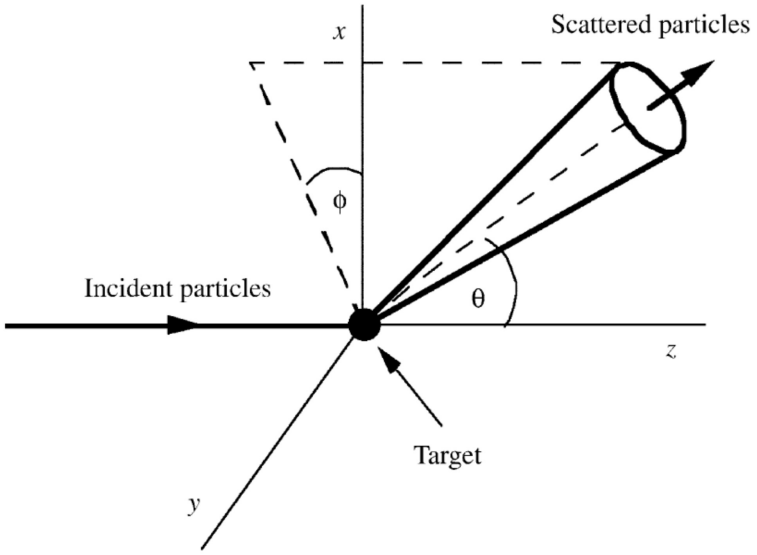

Figure 1.2: *Geometry of the differential cross section: a beam of particles is incident along the z-axis and collides with a stationary target at the origin; the differential cross-section is proportional to the rate of particles to be scattered into a small solid angle $d\Omega$ in the direction (θ, ϕ)*

particles appear at a rate R_b, then the reaction cross section is:

$$\sigma = \frac{R_b}{I_a N} \tag{1.7}$$

If a detector is placed in a fixed place in order to record particles b emitted in a direction (θ, ϕ), with respect to the beam direction, as shown in figure 1.2, it defines a small solid angle $d\Omega$ at the target nucleus. Therefore, it does not observe all of the outgoing particles, but only a small fraction dR_b are actually counted and only a fraction of cross section $d\sigma$ will be deduced. Moreover, the outgoing particles will not in general be emitted uniformly in all directions, but will have an angular distribution that will depend on the spherical coordinates θ and ϕ. Representing the angular distribution by $r(\theta, \phi)$ then:

$$dR_b = \frac{r(\theta, \phi) d\Omega}{4\pi}$$

so from (1.7) it yields:

$$\frac{d\sigma}{d\Omega} = \frac{r(\theta, \phi)}{4\pi I_a N} \tag{1.8}$$

The quantity $\frac{d\sigma}{d\Omega}$ is called the differential cross section.

The reaction cross section σ_r can be found by integrating the quantity $\frac{d\sigma}{d\Omega}$ over all angles with $d\Omega = sin\theta d\theta d\phi$ so:

$$\sigma_r = \int \frac{d\sigma}{d\Omega} d\Omega = \int_0^{\pi} sin\theta d\theta \int_0^{2\pi} \frac{d\sigma}{d\Omega} d\phi \tag{1.9}$$

The total cross section σ_t is a sum of the reaction cross sections σ_r for all possible different outgoing particles b, no matter what their direction or energy is.

$$\sigma_t \equiv \sum_r \sigma_r \tag{1.10}$$

Such a determination gives the probability for an incident particle to have any reaction with the target and thus be removed from the beam of incident particles [57, 58].

In an actual experiment it is measured the rate (events/s) at which a certain reaction occurs under certain conditions. The measurable experimental parameters are:

- Incident beam current I (in Amperes)
- Number n of target nuclei per unit volume
- Target thickness x (in cm)
- Solid angle $\Delta\Omega$ of detector (in sr)
- Reaction events counted (N particles detected) during time t

The fraction N/N_0 of all incident particles (N_0) that will result in particles N scattered at θ within a solid angle $\Delta\Omega$ is $nx(d\sigma/d\Omega)\Delta\Omega$ or:

$$\frac{N}{N_0} = nx\frac{d\sigma}{d\Omega}\Delta\Omega \tag{1.11}$$

The beam current is $I(A)$. By using $n = \frac{\rho(\frac{gr}{cm^3})A_0(\frac{nuclei}{mol})}{M(\frac{g}{mol})}$ it can be rewritten:

$$N = N_0 nx\frac{d\sigma}{d\Omega}\Delta\Omega = \frac{I(A)t(s)}{q(C)}\frac{\rho A_0}{M}\Big(\frac{nuclei}{cm^3}\Big)x(cm)\frac{d\sigma}{d\Omega}\Big(\frac{cm^2}{sr}\Big)\Delta\Omega(sr) \tag{1.12}$$

By using $Q(C) = I(A)t(s)$ the equation can be solved for:

$$\frac{d\sigma}{d\Omega} = \frac{NqM}{Q\rho A_0 x\Delta\Omega} \tag{1.13}$$

By replacing $\tau(\frac{mg}{cm^2}) = \rho x$ and $A_0 = 6.023 \cdot 10^{23}\ \frac{nuclei}{mol}$ it yields:

$$\sigma = \frac{0.267 \cdot A \cdot \text{charge state} \cdot 10^{-6}N}{Q \cdot \tau \cdot \text{efficiency} \cdot \Omega}mb \tag{1.14}$$

where Q is in μCb, τ is the target thickness in mg/cm^2, A is the target mass number, Ω is the solid angle and N are the reaction events.

1.2 Scattering process

Many important discoveries in nuclear and atomic physics have been made by scattering experiments. Such examples are the discovery of the nucleus by Rutherford and the discovery of subatomic particles. Information on the structure of these bodies can be obtained by bombarding them with particles and measure the number of particles scattered in various directions. The energy and angular distribution of scattered particles will depend on the shape of the target and the nature of forces between the particles and the target. The study of scattering process can be made by classical or quantal approaches.

1.2.1 Classical scattering theory

Classical trajectories and cross-sections

Consider a particle incident on some scattering center with energy E and impact parameter b. It emerges at some scattering angle θ. More generally, all particles in a beam incident in a hatched region of area $d\sigma = 2\pi b\, db$ are scattered into the angular region $(\theta, \theta + d\theta)$ which corresponds to a solid angle $d\Omega$ as shown in figure 1.3. In terms of the impact parameter and the

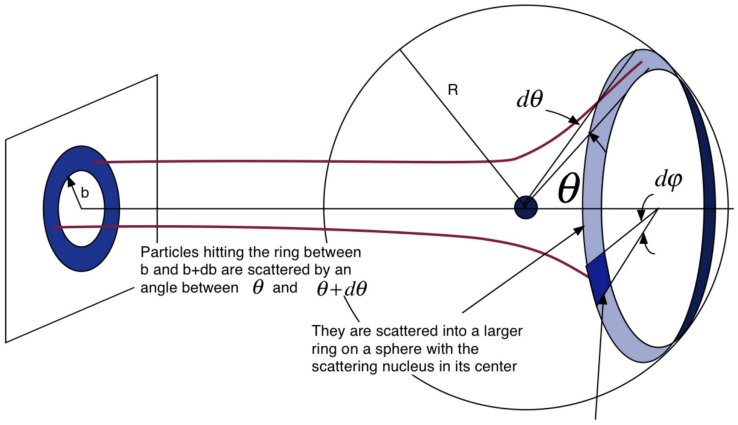

Figure 1.3: *Particles incident in the area $d\sigma$ scatter into the solid angle $d\Omega$.*

azimuthal angle ϕ, $d\sigma = bdbd\phi$ and $d\Omega = \sin\theta d\theta d\phi$ so

$$\frac{d\sigma(\theta)}{d\Omega} = \frac{b}{\sin\theta}\left|\frac{db}{d\theta}\right| \tag{1.15}$$

The equations of motion for the incident particle, $m\ddot{r}(t) = F(r)$ and the initial conditions, define the trajectory of the particle. For a particle obeying classical mechanics it holds that:

- The trajectory for the unbound motion, corresponding to a scattering event, is deterministically predictable, given by the interaction potential and the initial conditions.
- The path of any scatterer in the incident beam can be followed and its angular deflection is determined as precisely as required.

For the scattering from nontrivial central forces, the trajectory can be obtained from the equations of motion by using energy and angular momentum conservation methods. One can rewrite

$$E = \frac{1}{2}m\dot{r}^2 + \frac{L^2}{2mr^2} + V(r) \tag{1.16}$$

in the form

$$\sqrt{\frac{2}{m}\Big(E - \frac{L^2}{2mr^2} - V(r)\Big)} = \frac{dr}{dt} = \frac{dr}{d\theta}\frac{d\theta}{dt} \tag{1.17}$$

The angular momentum can be written via the angular velocity $L = mr^2\dot{\theta}$ From equation (1.17) it yield that:

$$d\theta = \Big(\frac{L}{r^2\sqrt{2m(E - L^2/2mr^2 - V(r))}}\Big)dr \tag{1.18}$$

The angle through which the particle moves between two radial distances r_1 andr_2 is:

$$\Delta\theta = \int_{r_1}^{r_2} \frac{L}{r^2\sqrt{2m(E - L^2/2mr^2 - V(r))}}dr \tag{1.19}$$

In case of a central potential and in the distance of closest approach r_{min} it can be defined the deflection angle Θ as $2\Theta + \theta = \pi$. By using the initial angular momentum $L = b\sqrt{2mE}$ it yields that:

$$\Theta = \int_{r_{min}}^{\infty} \frac{b}{r^2\sqrt{1 - b^2/r^2 - V(r)/E}}dr \tag{1.20}$$

Rutherford scattering

In a nuclear reaction the nuclei of the projectile and the target are positively charged. When the distance between the two nuclei is greater than the sum of their radii only the Coulomb force acts. This situation is known as *Rutherford scattering* or *Coulomb scattering* [57]. The basic geometry for the Rutherford scattering is shown in figure 1.4

The Coulomb force between a projectile with mass m and charge Z_1e and a target nucleus with charge Z_2e is:

$$F_C = \frac{Z_1Z_2e^2}{r^2}$$

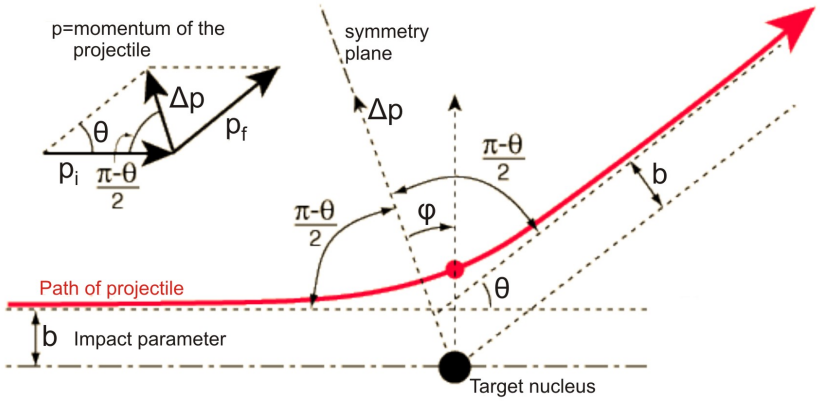

Figure 1.4: *Coordinates for describing Rutherford scattering of a charged particle by a target T with a charge of the same sign.*

where r is the distance between them. If the target is much heavier than the projectile, it is supposed to remain at rest and the nuclear recoil may be neglected. If the collision between the incident particle and the nucleus was head on, the distance of closest approach r_0 is obtained by equating the initial kinetic energy E of the projectile to the Coulomb energy at closest approach, so

$$r_0 = \frac{Z_1 Z_2 e^2}{E} \tag{1.21}$$

at which point the projectile would reverse direction and the scattering angle θ would be equal to π. If the particle approaches the target nucleus along a straight line witch stand off a distance b from the nucleus then the scattering angle will be smaller and the projectile will describe an orbit which will be a branch of an hyperbola. The distance b is called the *impact parameter*.

Let the projectile velocity be v at a very great distance from the nucleus where the potential is negligible and let its velocity be v_0 at the point of closest approach, r_{min}. The conservation of energy gives:

$$\frac{1}{2}mv^2 = \frac{1}{2}mv_0^2 + \frac{Z_1 Z_2 e^2}{r_{min}} \qquad \text{or} \qquad \left(\frac{v_0}{v}\right)^2 = 1 - \frac{r_0}{r_{min}} \tag{1.22}$$

Conservation of angular momentum implies:

$$mvb = mv_0 r_{min} \tag{1.23}$$

Using the equation (1.22) is taken a relation between b and r_{min}:

$$b^2 = r_{min}(r_{min} - r_0) \tag{1.24}$$

It is property of the hyperbola that $b = r_{min} \tan\left(\frac{a}{2}\right)$ so in this case, since $\theta = \pi - 2\alpha$, is found:

$$\tan\left(\frac{\theta}{2}\right) = \frac{r_0}{2b} \tag{1.25}$$

If a flux of I_0 particles per unit area cross a plane perpendicular to the beam as shown in figure 1.4, the flux pases through the annulus with radii $b, b + db$ is:

$$dI = 2\pi I_0 b db \tag{1.26}$$

Differentiating eq (1.25) gives

$$db = -\frac{r_0}{4\sin^2(\theta/2)} d\theta \tag{1.27}$$

and from which eq (1.26) results that:

$$dI = \frac{1}{4}\pi I_0 r_0^2 \frac{cos(\frac{\theta}{2})}{sin^3(\frac{\theta}{2})} \tag{1.28}$$

with $d\Omega = 2\pi sin\theta d\theta$ for the ring geometry the differential cross-section is:

$$\frac{d\sigma}{d\Omega} = \frac{1}{I_0}\frac{dI}{d\Omega} = \left(\frac{Z_1 Z_2 e^2}{2mv^2}\right)^2 \frac{1}{sin^4(\frac{\theta}{2})} \tag{1.29}$$

This is the differential cross section for Rutherford scattering, usually called the *Rutherford cross section.* [57, 58]

1.2.2 Quantum scattering

Scattering by a central potential

The scattering of one particle off another at nonrelativistic energies is described by a time-dependent Schrodinger equation:

$$i\hbar\frac{\partial}{\partial t}\Psi(r,t) = H\Psi(r,t) \tag{1.30}$$

In the center of mass of the two particles, the Hamiltonian has the form:

$$H = -\frac{\hbar^2}{2\mu}\nabla^2 + V \tag{1.31}$$

where μ is the reduced mass of the particles and V is the potential representing the interaction between the two particles. If H is independent of time t, the time dependence in the wave function may be separated from the rest,

$$\Psi(\mathbf{r},t) = \psi(\mathbf{r})e^{-iEt/\hbar} \tag{1.32}$$

The usual scattering arrangement involves a collimated beam of projectile particles traveling along the positive z axis and incident on a target placed

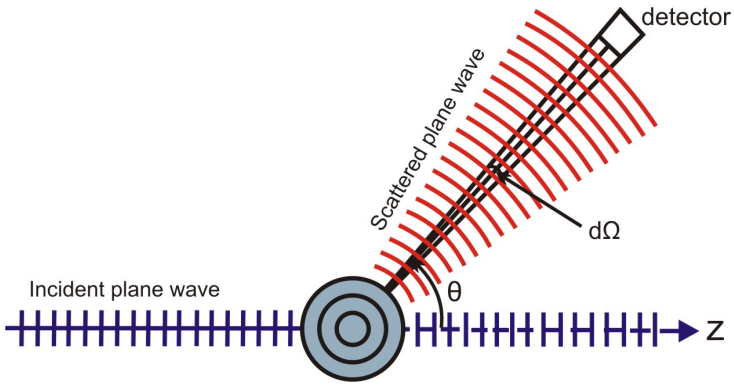

Figure 1.5: *Geometry of the scattering plane*

at the origin, as shown in figure 1.5. Outside the range of the interaction $V = 0$. The incident's beam wave function may be represented by plane waves e^{ikz} corresponding to momentum $p = \hbar k$, where $k = \sqrt{2\mu E}/\hbar$ is the wave number. The scattered particle outside the interaction region is described by a spherical wave e^{ikr}/r radiating outward from the center of the interaction region. The wave function at large r is a linear combination of a plane wave, made of the incident beam and particles not scattered by the potential, and a spherical wave, made of scattered particles [59]. The result may be expressed as:

$$\psi(\mathbf{r}) \longrightarrow \psi_{inc} + \psi_{scat}$$

$$\psi(\mathbf{r}) \longrightarrow e^{ikz} + f(\theta,\phi)\frac{e^{i\mathbf{k}\cdot\mathbf{r}}}{r} \qquad r \to \infty \tag{1.33}$$

Here, $f(\theta,\phi)$ is the *scattering amplitude* which measures the fraction of incident wave scattered in the direction with polar angle θ and azimuthal angle ϕ. It is convenient to take the origin of the coordinate system at the center of the region where the two particles come into contact. The z-axis is chosen to be along the direction of the line joining the two particles outside the interaction zone and the xy plane is fixed by requiring it to be perpendicular to the z-axis. However, there is no natural way to define the orientation of the x- or y-axis in the plane. So the system is invariant under a rotation around the z-axis and the azimuthal angle ϕ cannot be determined uniquely. The wavefunction of the system must be independent of ϕ and the scattering amplitude becomes a function of the polar angle θ only.

Partial Wave Analysis

If the interaction potential is a central one, $V = V(r)$, that depends only on the relative distance r , angular momentum is a constant of motion. In this case, it is convenient to decompose the wave function $\psi(\mathbf{r})$ into a product of radial and angular parts and write it as a sum over components

with definite orbital angular momentum l, or *partial waves*,

$$\psi(r,\theta) = \sum_{l=0}^{\infty} b_l R_l(r) Y_{l0}(\theta) \tag{1.34}$$

where the coefficients b_l are the amplitudes of each partial wave. Only spherical harmonics $Y_{lm}(\theta,\phi)$ with $m = 0$ are involved here, as is considered system independent of the azimuthal angle ϕ. So the incident wave-functions as well as the scattered wave-functions can be similarly decomposed into these partial waves, each having a definite value of l. By conservation of angular momentum the l value of each partial wave cannot change during the scattering process.

The incident plane waves can be expanded into partial waves as:

$$\begin{aligned} \psi_{inc} &= Ae^{ikz} = A\exp(ikr\cos\theta) \\ &= A\sum_{l=0}^{\infty} i^l(2l+1)j_l(kr)P_l(\cos\theta) \end{aligned} \tag{1.35}$$

where A is an appropriately chosen normalization constant. The radial functions $j_l(kr)$ are spherical Bessel functions, they are solutions to the radial part of the Schrödinger equation in a region far from the target where the nuclear potential vanishes. The angular functions $P_l(\cos\theta)$ are the Legendre polynomials. When the wave is far from the nucleus, the $j_l(kr)$ have the following convenient expansion:

$$j_l(kr) \longrightarrow \frac{1}{kr}\sin\Big(kr - \frac{l\pi}{2}\Big) = i\frac{e^{-i(kr-l\pi/2)} - e^{+i(kr-l\pi/2)}}{2kr} \tag{1.36}$$

so that

$$\psi_{inc} = \frac{A}{2kr}\sum_{l=0}^{\infty} i^{l+1}(2l+1)\Big[e^{-i(kr-l\pi/2)} - e^{+i(kr-l\pi/2)}\Big]P_l(\cos\theta) \tag{1.37}$$

The first term in brackets, involving e^{-ikr}, represents an incoming spherical wave converging on the target, while the second term e^{+ikr}, represents an outgoing spherical wave emerging from the target nucleus. The scattering can affect only the outgoing wave in two ways: through a change in phase and through a change in amplitude (in case of inelastic scattering).

By replacing $j_l(kr)$ in its asymptotic form, equation (1.33) can be rewritten as:

$$\sum_{l=0}^{\infty} b_l \frac{1}{kr}\sin\Big(kr - \frac{l\pi}{2} + \delta_l\Big)P_l(\cos\theta) =$$

$$\sum_{l=0}^{\infty}(2l+1)i^l\frac{1}{kr}\sin\Big(kr - \frac{l\pi}{2})P_l(\cos\theta) + f(\theta)\frac{e^{ikr}}{r} \tag{1.38}$$

By expanding each of the sine functions in terms of exponentials it results:

$$e^{ikr}\sum_{l=0}^{\infty} b_l e^{-il\pi/2}e^{i\delta_l}P_l\cos(\theta) - e^{-ikr}\sum_{l=0}^{\infty} b_l e^{il\pi/2}e^{-i\delta_l}P_l\cos(\theta) =$$

$$e^{ikr}\Big\{2ikf(\theta)+\sum_{l=0}^{\infty}(2l+1)i^l e^{-il\pi/2}P_l(\cos\theta)\Big\} - e^{-ikr}\sum_{l=0}^{\infty}(2l+1)i^l e^{il\pi/2}P_l(\cos\theta) \tag{1.39}$$

By equating the coefficients of e^{-ikr} and e^{ikr} on both sides of the above equation it results:

$$b_l = (2l+1)i^l e^{i\delta_l} \tag{1.40}$$

and

$$f(\theta) = \frac{1}{k}\sum_{l=0}^{\infty}(2l+1)e^{i\delta_l}\sin\delta_l P_l(\cos\theta) \tag{1.41}$$

The parameter δ_l is called the phase shift since it determines the difference in phase of the scattered solution from the asymptotic solution [60].

The differential cross section is the number of particles scattered into $d\Omega$ divided by $d\Omega$ times the incident flux. Hence:

$$\frac{d\sigma}{d\Omega} = \frac{k'}{k}f(\theta)^2 \tag{1.42}$$

For elastic scattering $k = k'$, so this is reduced to

$$\frac{d\sigma}{d\Omega} = f(\theta)^2 \tag{1.43}$$

Combining this with the previous results it yields:

$$\frac{d\sigma}{d\Omega} = \frac{1}{k^2}\Big|\sum_{l=0}^{\infty}(2l+1)e^{i\delta_l}\sin\delta_l P_l(\cos\theta)\Big|^2 \tag{1.44}$$

Integrating this result over $d\Omega$ yields the total cross section:

$$\begin{aligned}\sigma = \int d\sigma &= \frac{2\pi}{k^2}\int_0^{\pi}\Big|\sum_{l=0}^{\infty}(2l+1)\sin\delta_l P_l(\cos\theta)\Big|^2\sin\theta d\theta \\ &= \frac{4\pi}{k^2}\sum_{l=0}^{\infty}(2l+1)\sin^2\delta_l\end{aligned} \tag{1.45}$$

The scattering Matrix: S-Matrix

In the formal theory of scattering it is convenient to introduce the S-matrix (scattering matrix). The matrix elements of the S-matrix between

initial and final plane wave states in the infinite past and the infinite future, correspond to the probability amplitudes for a transition of the system from the initial state to the final state.

The outgoing wave after the interaction with the potential $V(r)$ can be written as:

$$\psi(\mathbf{r}) = \frac{A}{2kr}\sum_{l=0}^{\infty} i^{l+1}(2l+1)\Big[e^{-i(kr-l\pi/2)} - S_l(k)e^{+i(kr-l\pi/2)}\Big]P_l(\cos\theta) \quad (1.46)$$

where $S_l(k)$ is given by:

$$S_l(k) = exp[2i\delta_l(k)] \quad (1.47)$$

As it is clear from equation (1.47) the S-matrix is unitary: $S^{\dagger} = S^{-1}$, where $S^{\dagger}$ is the Hermitian conjugate of S. In terms of $S_l(k)$ the scattering amplitude $f(\theta)$, the differential cross sections $d\sigma(\theta)$ and the total cross section σ are given by:

$$f(\theta) = \frac{1}{2kr}\sum(2l+1)(S_l - 1)P_l(\cos\theta) \quad (1.48)$$

$$\frac{d\sigma(\theta)}{d\Omega} = \Big|\frac{1}{2kr}\sum(2l+1)(S_l - 1)P_l(\cos\theta)\Big|^2 \quad (1.49)$$

$$\sigma = \frac{1}{k^2}\sum(2l+1)|1 - S_l|^2 \quad (1.50)$$

1.3 The Optical Model

The interaction between a nucleon and a nucleus, or between two nuclei, is one of the most important aspects in nuclear physics. It governs the elastic and inelastic scattering and determines the behavior of the various channels in nuclear reactions [1, 2, 3]. This interaction is a complicated many body problem even for the analysis of elastic scattering. All the nucleons of the target nucleus interact with each other and with the incident nucleon, and each individual nucleon-nucleon interaction contains central exchange and tensor components. The *optical model* approximates of this complicated interaction by a two-body potential between the incident particle and the target nucleus. The detailed structure of the target nucleus and incident nucleus are ignored. The optical model takes that name as the scattering of nucleons by nuclei parallels the scattering of light waves by a refracting sphere ("cloudy" crystal ball). In that model the elastic scattering may be compared with refraction of optical waves and the inelastic scattering with absorption due to the fact that the crystal ball is cloudy [58].

The origin of the optical model potential is the average interaction between the nucleons in the projectile with those in the target nucleus. The scattering is represented in terms of a complex potential $U(r)$

$$U(r) = V(r) + iW(r) \tag{1.51}$$

where the real functions V and W are selected to give to the potential its proper radial dependence. The real part $V(r)$ is responsible for the elastic scattering; it describes the ordinary nuclear interaction between target and projectile and may be very similar to the shell-model potential. The imaginary part $W(r)$ is responsible for the absorption, that is the reaction process which removes flux from the elastic scattering channel.

Basically, there are two approaches to the problem of defining this potential. The first approach is that of a fundamental theory of nuclear structure in terms of the interactions of the constituent nucleons. The alternative approach is the phenomenological one of adjusting the potential systematically until optimum agreement with the experimental data is obtained. A satisfactory optical potential can be found by combining these approaches. First using fundamental theories to give the overall form of the potential and then using the phenomenological method to determine the optimum parameters of the potential of this form.

1.3.1 Macroscopic optical model potential

The simplest form of optical potential is the square-well potential [60]

$$U(r) = -V_0 - iW_0 \qquad \text{for} \qquad r < a \tag{1.52}$$

This form of potential gives too large cross section for the elastic scattering process in backward angles. The most common form of the optical potential is the Woods-Saxon form, in which the radial dependence of an optical model potential follows closely the density distribution in a nucleus

$$f(r, r_0, a) = \frac{1}{1 + exp(\frac{r-R}{a})} \tag{1.53}$$

where $R = r_0 A^{1/3}$. So:

$$U_{vol}(r) = -\frac{V_0}{1 + exp(\frac{r-R_v}{a_v})} - i\frac{W_0}{1 + exp(\frac{r-R_w}{a_w})} \tag{1.54}$$

where V_0 and W_0 are the depths of the real and imaginary part of the potential well, R_v and R_w the radii and a_v, a_w the surface diffuseness. These six quantities are taken as free parameters to be determined by fitting experimental elastic scattering data.

The potential given by equation (1.54) is only the volume term, in the sense that it depends on the distribution of matter in the whole nucleus.

In addition, optical model potentials are known to have a spin dependence. When a nucleon is scattered from a nucleus, the result is sensitive to the relative orientation of the nucleon spin before and after the scattering. A *spin-orbit* term may be used to represent such an effect,

$$U_{S.O.}(r) = \sigma \cdot l\Big(\frac{\hbar}{m_\pi c}\Big)^2 \frac{1}{r}\Big\{V_s \frac{d}{dr} f(r, r_{sv}, a_{sv}) + iW_s \frac{d}{dr} f(r, r_{sv}, a_{sv})\Big\} \quad (1.55)$$

Again there are six parameters, V_s, r_{sv}, a_{sv}, W_s, r_{sw} and a_{sw} to be adjusted to fit the scattering data.

For charged particle scattering, a Coulomb term should be included in the optical model potential. The form is usually obtained by approximating the target nucleus as a uniformly charged sphere,

$$U_C(r) = \begin{cases} \Big[\frac{1}{4\pi\epsilon_0}\Big] \frac{zZe^2}{2R_C}\big(3 - \frac{r^2}{R_C^2}\big) & \text{for } r < R_C \\ \Big[\frac{1}{4\pi\epsilon_0}\Big] \frac{zZe^2}{r} & \text{for } r \geq R_C \end{cases} \quad (1.56)$$

where R_C, is the Coulomb radius. The quantities z and Z are, respectively, the charge numbers of the projectile and the target nucleus [59].

The complete phenomenological optical model potential is the sum of volume, spin-orbit and Coulomb terms:

$$U_{opt}(r) = U_{vol}(r) + U_{S.O.}(r) + U_C(r) \quad (1.57)$$

1.3.2 Microscopic optical model potential and M3Y interaction

An optical model potential for nucleus-nucleus scattering (even if one of them is a single nucleon) represents the average interaction between the nucleons of the projectile and the nucleons in the target nucleus. It is, therefore, a many body problem approximated by an effective nucleon-nucleon interaction. A microscopic model of the potential may be constructed by convoluting the fundamental nucleon-nucleon interaction with the nuclear density. Except for a possible dependence on the spins of the two nuclei, this potential is assumed to depend only upon the distance $\mathbf{r_a}$ between the centers of mass of the two nuclei. The folding models, represent a move in this direction of incorporating more nuclear structure information [3, 58, 59].

Nucleon-nucleus scattering: If an incident nucleon a interacts with each target nucleon i through a nucleon-nucleon potential, or effective interaction $u(|\mathbf{r_a} - \mathbf{r_1}|)$, where $|\mathbf{r_a} - \mathbf{r_1}|$ is the distance between them, then the overall potential it experiences due to the target nucleus is

$$U(\mathbf{r_a}) = \int \rho_A(\mathbf{r_1}) u(\mathbf{r_a} - \mathbf{r_1}) d\mathbf{r_1} \quad (1.58)$$

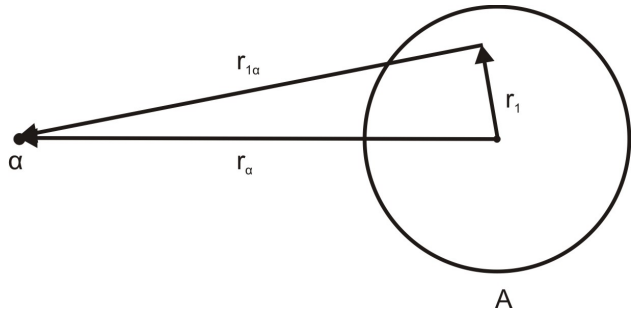

Figure 1.6: *Coordinates used for single-folding potential*

where $\rho_A(\mathbf{r_1})$ is the density of the nucleus A at the position i.

This single folding potential describes the scattering of two particles, where the target is undisturbed and elastic scattering is the only process. So, the folding models are a good approach for the calculation of the real part of the potential. If non-elastic processes take place, their absorption can be represented by adding an imaginary term to the optical potential.

Nucleus-nucleus scattering: If the projectile is not a single nucleon but a composite particle like deuteron, a-particle and heavy ions, the integration must be done over the nucleons in the projectile as well as in the target. If the density distribution in the target is $p_A(\mathbf{r})$ and in the projectile is $p_a(\mathbf{r})$, equation (1.58) is replaced by the following formula

$$U(\mathbf{r_a}) = \int\int \rho_A(\mathbf{r_1})\rho_a(\mathbf{r_2})u(\mathbf{r_{12}})d\mathbf{r_1}d\mathbf{r_2} \tag{1.59}$$

where $\mathbf{r_{12}} = \mathbf{r_a} - \mathbf{r_1} + \mathbf{r_2}$. Because the integration is over two densities this is called double folding model.

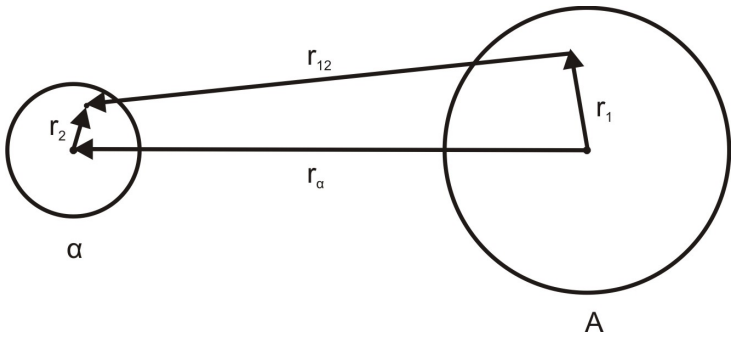

Figure 1.7: *Coordinates used for double-folding potential*

The density distributions $\rho_A(r)$ and $\rho_a(r)$ are normalized so that

$$\int \rho_A(\mathbf{r})d\mathbf{r} = A \quad , \quad \int \rho_a(\mathbf{r})d\mathbf{r} = a \tag{1.60}$$

where A, a are the number of nucleons in the respective nuclei.

The effective nucleon-nucleon interaction may be written as a sum of central (C), spin-orbit (LS) and tensor (T) terms [61]:

$$\begin{aligned} u_{12} = u_{00}^{C} &+ u_{01}^{C}\tau_{\mathbf{1}}\cdot\tau_{\mathbf{2}} + u_{10}^{C}\sigma_{\mathbf{1}}\cdot\sigma_{\mathbf{2}} + u_{11}^{C}\tau_{\mathbf{1}}\cdot\tau_{\mathbf{2}}\sigma_{\mathbf{1}}\cdot\sigma_{\mathbf{2}} \\ &+ (u_{0}^{LS} + u_{1}^{LS}\tau_{\mathbf{1}}\cdot\tau_{\mathbf{2}})\mathbf{L_{12}}\cdot(\sigma_{\mathbf{1}}\cdot\sigma_{\mathbf{2}}) \\ &+ (u_{0}^{T} + u_{1}^{T}\tau_{\mathbf{1}}\cdot\tau_{\mathbf{2}})S_{12} \end{aligned} \tag{1.61}$$

In an approach, appropriate for low energies, the effective interaction can be represented by a sum of Yukawa functions (M3Y interactions), the strengths of which were adjusted to reproduce the G-matrix elements. From their origin in G-matrices for bound nucleons, M3Y effective interactions are real and have to be supplemented by phenomenological imaginary parts. In the M3Y approach the u_{00} and u_{01} components of equation (1.61) have the form

$$u_{00}(r) = \left[7999\frac{e^{-4r}}{4r} - 2134\frac{e^{-2.5r}}{2.5r}\right] \qquad \text{MeV} \tag{1.62}$$

and

$$u_{01}(r) = -\left[4886\frac{e^{-4r}}{4r} - 1176\frac{e^{-2.5r}}{2.5r}\right] \qquad \text{MeV} \tag{1.63}$$

1.4 Dispersion Relations

The study of the energy dependence of the nuclear optical potential at near barrier energies is one of the tools to investigate the influence of the breakup, nuclear transfer and other reaction mechanisms. One of the most important properties of the potential is the Dispersion relations, which relate the energy dependences of its real and imaginary parts.

1.4.1 Threshold anomaly

When studying nuclear reactions at energies well above the Coulomb barrier, a slow variation of the real and imaginary part of the optical potential is observed. These features no longer remain true when the bombarding energies approach the vicinity at the top of the Coulomb barrier [6]. The first indications of this unexpected behavior were provided by optical potential analysis of elastic scattering measurements with heavy nuclei ^{16}O+^{208}Pb and ^{32}S + ^{40}Ca [62, 63]. As shown in figure 1.8 both the real and the imaginary parts of the optical potential are nearly energy independent at energies above the Coulomb barrier, but as the energy decreases toward the barrier, the imaginary part $W(E)$ sharply decreases while the real part $V(E)$ presents a localized peak. To that behavior was given the term *threshold anomaly*.

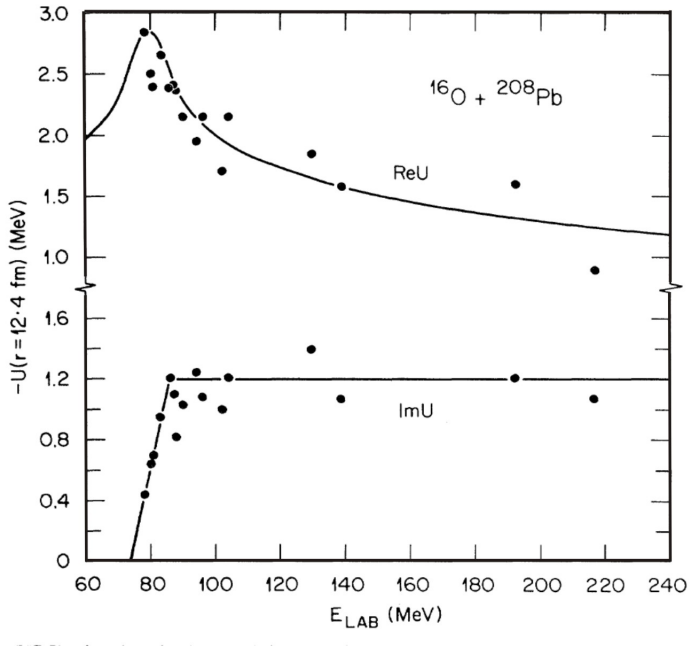

Figure 1.8: *Variation with bombarding energy of the real and imaginary parts of the optical potential U for* $^{16}O + ^{208}Pb$ *[5].*

This behavior is ascribed to the effects of couplings to the nonelastic channels, which can produce changes in the real potential even below the threshold, where they are energetically closed. Such couplings are included in a very general way in the **dispersion relation** which connects the real and the imaginary parts of the generalized optical potential.

1.4.2 Causality and the dispersion relation

Considering the single particle wave equation

$$\left[-\frac{\hbar^2}{2m}\nabla^2 + M(E) \right] \Phi_E(\mathbf{r}) = E\Phi_E(\mathbf{r}) \tag{1.64}$$

where the one-body operator $M(E) = V(E) + iW(E)$ is constructed in such a way that the asymptotic behavior of $\Phi_E(\mathbf{r})$ for large $|\mathbf{r}|$ yields the exact complex elastic scattering phase shift of a nucleus-nucleus or nucleon-nucleus collision. By introducing the Fourier transforms

$$U(t) = (2\pi)^{-1} \int M(E) e^{iEt/\hbar} dE$$

$$\psi(\mathbf{r}, t) = \Phi_E(\mathbf{r}) e^{iEt/\hbar}$$

the wave equation (1.64) becomes:

$$-\frac{\hbar^2}{2m}\nabla^2\Psi(\mathbf{r},t)+\int_{\infty}^{\infty}U(t-t')\psi(\mathbf{r},t')dt'=i\hbar\frac{\partial}{\partial t}\Psi(\mathbf{r},t) \tag{1.65}$$

The causality principle corresponds to the requirement that $U(t-t')=0$ for $t<t'$ which means that a scattered wave is never emitted before the arrival of the incident wave [64, 4].

The effect of the causality principle leads to the dispersion relation between the real and the imaginary parts of the optical potential. By ignoring some pole terms which arise from quasibound states of the system the dispersion relation has the form:

$$V(\mathbf{r},\mathbf{r}';E)=V_0(\mathbf{r},\mathbf{r}')+\frac{P}{\pi}\int_{\infty}^{\infty}\frac{W(\mathbf{r},\mathbf{r}';E)}{E'-E}dE'=V_0(\mathbf{r},\mathbf{r}')+\Delta V(\mathbf{r},\mathbf{r}';E) \tag{1.66}$$

where P denotes principal value. This potential is nonlocal in coordinate space. The first term, V_0, is real and independent of energy and represents the average interaction of the two nuclei in the absence of any excitation and can be interpreted as a generalized "folded" potential which includes all the exchange terms that arise from anti-symmetrization between the two ions. The imaginary potential, W, only receives contributions from the open, energy-conserving channels, into which some flux is actually lost [6].

1.4.3 The linear segment model for W(E)

The dispersion integral for ΔV in equation (1.66) involves $W(E)$ at all energies E. In general $W(E)$ is not known and especially its high-energy behavior. Different hypothetical extrapolations may provide very different values for ΔV at the energies of interest. Furthermore, also the "bare" potential V_0 is not known empirically. However, the interest lies in the behavior of V with a rapid variation of $W(E)$ over a limited energy range. This may be singled out by using a subtracted version of the relations which was first suggested by Satchler [6]. The real part, V, is normalized to its empirical value at some reference energy E_S and are studied the dispersive effects relative to that. The subtracted form can be obtained from equation (1.66):

$$\Delta V(E)-\Delta V(E_S)=(E-E_S)\frac{P}{\pi}\int\frac{W(E)}{(E'-E_S)(E'-E)}dE \tag{1.67}$$

The simplest method to calculate this quantity is using an algebraic expression of a linear schematic model where $W(E)$ is composed of three linear segments as shown in figure 1.9. Each line segment associated with an increment $W_{ij}=W(E_i)-W(E_j)$ yields the following contribution to $\Delta V(E)$:

$$\Delta V_{ij}(E)=\frac{W_{ij}}{\pi}(\epsilon_i\ln|\epsilon_i|-\epsilon_j\ln|\epsilon_j|) \tag{1.68}$$

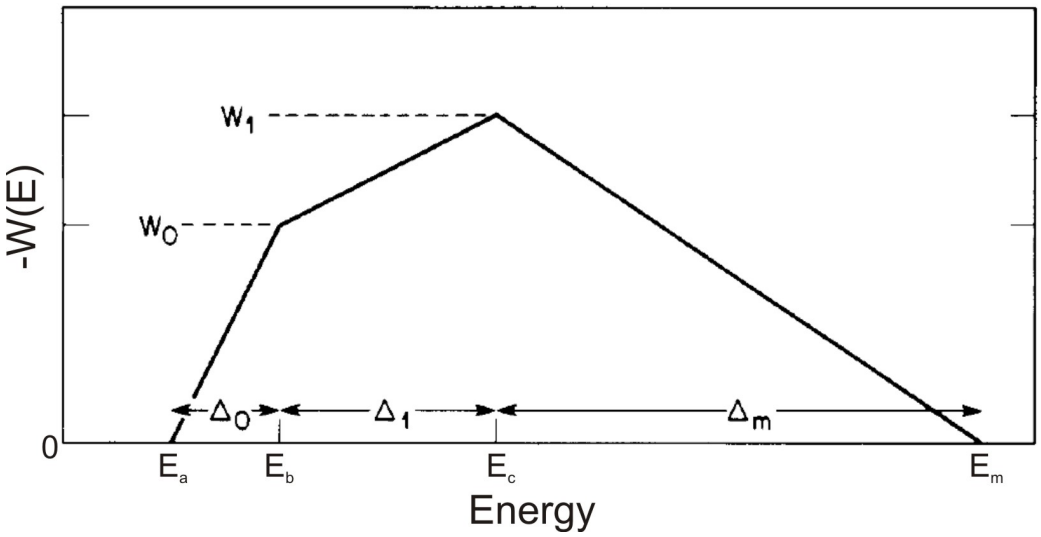

Figure 1.9: *The schematic model for $W(E)$ consisted of three straight segments.*

where $\epsilon_i = (E - E_i)\Delta_{ij}$, $\epsilon_j = (E - E_j)\Delta_{ij}$ and $\Delta_{ij} = E_i - E_j$ The full result is:

$$\pi\Delta V(E) = W_0(\epsilon_a \ln|\epsilon_a| - \epsilon_b \ln|\epsilon_b|) + (W_1 - W_0)(\epsilon'_b \ln|\epsilon'_b| - \epsilon'_c \ln|\epsilon'_c|) -$$

$$W_1(\epsilon''_c \ln|\epsilon''_c| - \epsilon''_m \ln|\epsilon''_m|) + W_1(\eta \ln|\eta| - (\eta+1)\ln|(\eta+1)|) \qquad (1.69)$$

where $W_0, W_1 \geq 0$ and $\epsilon_i = (E - E_i)/\Delta_0$, $\epsilon'_i = (E - E_i)/\Delta_1$, $\epsilon'_i = (E - E_i)/\Delta_m$, $\eta = \Delta_1/\Delta_m$.

1.5 Barrier distribution

In the scattering of heavy ions at energies close to the Coulomb barrier, the dynamics of both fusion and elastic scattering are influenced by coupling to direct-reaction channels, which can be described either by elaborate coupling channel theories or by the distribution of potential barriers [34, 65, 44]. Therefore, the barrier distribution is a fingerprint of the reaction characterizing the important channel couplings [66, 67]. A representation of barrier distribution can be extracted from fusion excitation functions or from (quasi)-elastic excitation functions.

There are many experimental advantages for measuring the (quasi)-elastic cross section rather than the fusion cross sections and use it in order to extract a representation of the barrier distribution. These are: i) less accuracy is required in the data for taking the first derivative rather than the second derivative, ii) whereas measuring the fusion cross section requires specialized recoil separators (electrostatic deflector / velocity filter) usually of low acceptance and efficiency, the measurement of (quasi-) elastic cross section

needs only very simple charged-particle detectors, not necessarily possessing good resolution either in energy or in charge, and iii) several effective energies can be measured at a single-beam energy, since, in the semiclassical approximation, each scattering angle corresponds to scattering at a certain angular momentum, and the cross section can be scaled in energy by taking into account the centrifugal correction [68].

1.5.1 Fusion excitation functions and barrier distributions

Nuclear fusion is the process, where two or more atomic nuclei join together or "fuse", to form a single heavier nucleus, as described in the following equation:

$$a + X \rightarrow Y \tag{1.70}$$

During this process, matter is not conserved because some of the mass of the fusing nuclei is converted to energy which is released. In order to fuse, projectile and target need to overcome a barrier for fusion, which arises due to the competition between Coulomb force, which is long-ranged and repulsive, and nuclear force, which is short-ranged and attractive. The sum of Coulomb and nuclear potentials is, in the simplest approximation, the total potential, which maximum value is called barrier height. A single barrier is expected to be observed clasically but due to quantal tunneling the barrier height is smeared and a distribution of barrier heights $D(B)$ is obtained.

A particle may overcome a potential barrier either classically or quantum mechanically. Classically a particle can overcome a potential barrier when its total energy exceeds the barrier height. In this case, the transmission probability over the barrier is zero, for energies below the barrier height and 1, for energies above the barrier. In quantum mechanic, however, energy conservation can be violated, so the particle has a probability to tunnel through the potential barrier. Because the incident flux is either reflected or transmitted, the conservation of flux can be expressed as:

$$T(E) + R(E) = 1 \tag{1.71}$$

where $T(E)$ is the transmission coefficient and $R(E)$ is the reflection coefficient. The transmission coefficient measures the penetration probability and the reflection coefficient measures the probability that the barrier reflects the flux. For an angular momentum dependent potential the transmission function becomes also angular momentum dependent with $T(E) = T_l(E)$ and for each l the fusion probability can be expressed as the differential cross section

$$\sigma_{fus}^{l} = \pi\lambda^2(2l+1)T_l(E) \tag{1.72}$$

where $\lambda = \hbar/p$ is the reduced de Broglie wavelength. By summing over all

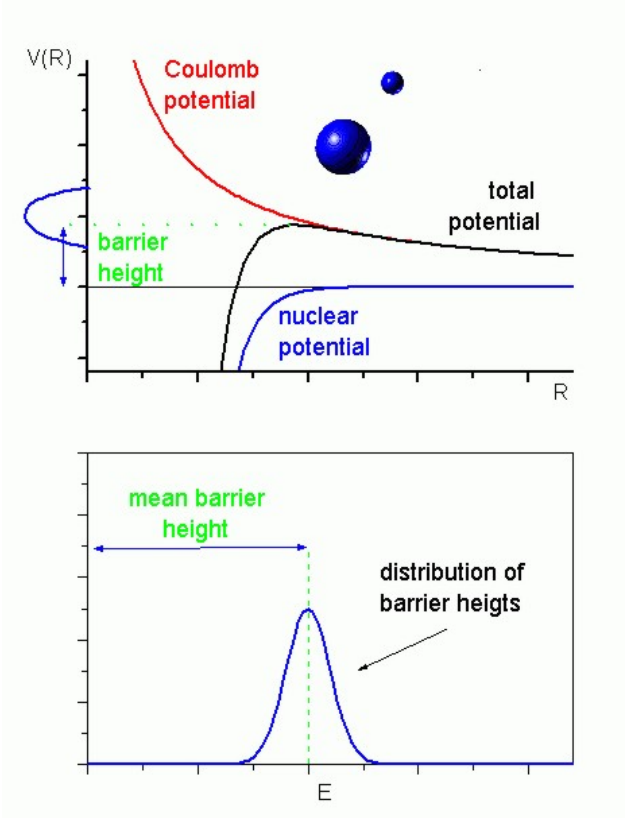

Figure 1.10: *The schematic model for fusion barrier distribution [69].*

angular momenta, the total fusion cross-section is obtained as:

$$\sigma_{fus} = \pi\lambda^2 \sum_l (2l+1) T_l(E) \tag{1.73}$$

By using the scattering matrix the transmission coefficient can be written as:

$$T_l(E) = 1 - |S_l|^2 \tag{1.74}$$

So the total fusion cross-section can be given by:

$$\sigma_{fus} = \pi\lambda^2 \sum_l (2l+1)(1 - |S_l|^2) \tag{1.75}$$

The simplest shape of a barrier is that of an inverted parabola. In this case the transmission functions $T_l(E)$ are given by:

$$T_l(E) = \left(1 + \exp\left[\frac{2\pi}{\hbar\omega_l}(B_l - E)\right]\right) \tag{1.76}$$

where B_l is the barrier for angular momentum $l\hbar$ By replacing that in equation (1.73) it yields the following analytical expression for the fusion excitation function

$$\sigma_{fus}(E) = \frac{\hbar\omega R^2}{2E} \ln\left(1 + \exp\left[\frac{2\pi}{\hbar\omega}(E - B)\right]\right) \tag{1.77}$$

where R is the position of the barrier, E the beam energy, B the barrier height and $\hbar\omega_0$ the barrier curvature for $l = 0$. Thus, the expression for a single barrier is:

$$\sigma(E,B) = \begin{cases} \pi R^2\left(1 - \frac{B}{E}\right) & \text{for } E > B \text{ (classical)} \\ \frac{\hbar\omega R^2}{2E}\exp\left[\frac{2\pi}{\hbar\omega}(E-B)\right] & \text{for } E < B \end{cases} \tag{1.78}$$

For reactions involving rotational nuclei the one-dimensional Coulomb barrier is replaced by a continuous distribution of fusion barriers $D(B)$. The fusion cross section at energy E is assumed to be given by:

$$\sigma_f(E) = \int_0^\infty \sigma(E,B)D(B)dB \tag{1.79}$$

where $\sigma(E,B)$ is the cross section (summed over all partial waves l) for a single barrier B, and $\int D(B)dB = 1$ [34].

When the contribution to the fusion cross section from each barrier is given by the classical formula of equation (1.78), the transmission coefficient can be deduced from the fusion excitation function

$$T(E) = \frac{1}{\pi R^2}\frac{d}{dE}\Big[E\sigma_{fus}(E)\Big] \tag{1.80}$$

Further differentiation with respect to energy results in a δ-function which represents the single barrier position and height:

$$\frac{dT(E)}{dE} = \frac{1}{\pi R^2}\frac{d^2(\sigma_{fus}E)}{dE^2} = \delta(E-B) \tag{1.81}$$

It is fundamental property of the δ-function that:

$$f(a) = \int_{-\infty}^{\infty} f(x)\delta(x-a)dx \tag{1.82}$$

Comparison with equation (1.79) shows that the δ-function is equivalent to the barrier distribution $D(E,B)$.

When tunneling is included, the fusion cross sections for a single barrier are given by the second part of equation (1.78). Double differentiation of $E\sigma_{fus}(E)$, with respect to energy gives:

$$\frac{1}{\pi R^2}\frac{d^2[E\sigma_{fus}(E)]}{dE^2} = \left[\left(\frac{2\pi}{\hbar\omega}\frac{e^x}{(1+e^x)^2}\right)\right] \equiv G_{fus}(E,B) \tag{1.83}$$

where $x \equiv \frac{2\pi}{\hbar\omega}(E-B)$ and $G_{fus}(E,B)$ is a peaked function.

1.5.2 Barrier distribution from quasi-elastic scattering

Single barrier: In a purely classical picture, for a single potential barrier and head-on collisions ($\theta = 180^o$), there is a direct relationship between the differential fusion cross section, $d\sigma_{fus}(E)$, and the quasi elastic scattering differential cross section, $d\sigma_{qel}(E)$, since any loss from the quasi-elastic channel contributes directly to fusion [65, 70, 71]. The reflection coefficient $R(E)$ is equal to the ratio $d\sigma_{el}/d\sigma_R$ for angular momentum $l\hbar = 0$ and therefore:

$$R(E) = \frac{d\sigma_{qel}}{d\sigma_R}(E) \tag{1.84}$$

It was proved that the transmission coefficient $T(E)$ can be expressed in terms of the fusion cross section:

$$T(E) = \frac{1}{\pi R^2}\frac{d}{dE}[E\sigma_{fus}(E)] \tag{1.85}$$

and that:

$$\frac{dT(E)}{dE} = \frac{1}{\pi R^2}\frac{d^2}{dE^2}[E\sigma_{fus}(E)] = \delta(E-B) = D(E,B) \tag{1.86}$$

The function $D(E,B)$ is the barrier distribution of the system which in case of a single barrier is a δ-function at the barrier height B. Since $T(E) = 1-R(E)$ it follows that:

$$D(E,B) = \frac{dT}{dE} = -\frac{dR}{dE} = -\frac{d}{dE}\Big[\frac{d\sigma_{qel}}{d\sigma_R}(E)\Big] \tag{1.87}$$

In the previous section it was shown that the fusion barrier distribution is:

$$D_{fus}(E) = \frac{d^2}{dE^2}\Big[E\sigma_{fus}(E)\Big] \tag{1.88}$$

is a narrowly peaked function. Since the function

$$D_{qel}(E) = -\frac{d}{dE}\Big[\frac{d\sigma_{qel}}{d\sigma_{ruth}}(E)\Big] \tag{1.89}$$

is also narrowly peaked, it defines an alternative representation of the barrier distribution in the case of a single barrier.

Multiple barriers: Multiple barrier penetration is described in a coupled-channel model which considers coupling to a finite number of states, but neglects their excitation energies (adiabatic approximation) and spins (isocentrifugal approximation).

The physical S-matrix elements are transformations of the eigenchannel S-matrix elements: $S^{phys}_{i;0} = U_{i\alpha}U_{0\alpha}S_\alpha$. The scattering amplitudes $f_j(E,\theta)$

for the physical reaction channels can be expressed as:

$$f_j(E,\theta) = \frac{1}{2ik}\sum_l (2l+1)P_l(\cos\theta)\exp(2i\sigma_\alpha^l)S_\alpha^l \quad (1.90)$$

$$= \frac{1}{2ik}\sum_{l,\alpha} (2l+1)P_l(\cos\theta)\exp(2i\sigma_\alpha^l)U_{i\alpha}U_{0\alpha}S_\alpha^l \quad (1.91)$$

where σ_α^l are the Coulomb phases in the eigenchannels. So the quasi-elastic scattering cross section relative to the Rutherford scattering can be expressed as:

$$\frac{d\sigma_{qel}}{d\sigma_{ruth}}(E,\theta) = \frac{1}{d\sigma_{ruth}}\sum_{\alpha=0}^{n} W_\alpha \Big|\frac{1}{2ik}\sum_l (2l+1)P_l(\cos\theta)\exp(2i\sigma_\alpha^l)S_\alpha^l\Big|^2 \quad (1.92)$$

For a particular angle θ,

$$\frac{d\sigma_{qel}}{d\sigma_{ruth}}(E) = \sum_{\alpha=0}^{n} W_\alpha \frac{d\sigma_\alpha}{d\sigma_{ruth}}(E) \quad (1.93)$$

In the eigen-channel model the quasi-elastic differential cross section is a weighted sum of the eigen-channel differential cross sections. The previous equation is equivalent to equation (1.75) for the fusion cross section. The difference between them is the phase term $\exp(2i\sigma_\alpha^l)$. The differentiation of equation (1.93), with respect to energy yields the distribution of barriers:

$$D_{qel}(E) \equiv -\frac{d}{dE}\Big[\frac{d\sigma_{qel}}{d\sigma_{ruth}}(E)\Big] = -\sum_{\alpha=0}^{n} W_\alpha \frac{d}{dE}\Big[\frac{d\sigma_\alpha}{d\sigma_{ruth}}\Big] \quad (1.94)$$

1.5.3 Barrier distribution from elastic scattering

The barrier distribution representation from quasi-elastic scattering shows a reduction of sensitivity to the barrier structure at energies above the average barrier. This may be due to "dephasing" of the various scattering amplitudes which contribute to the quasi-elastic scattering. As shown in the previous section, the scattering amplitudes $f_j(\theta,E)$ are given by the relation:

$$f_j(E,\theta) = \frac{1}{2ik}\sum_{l,\alpha} (2l+1)P_l(\cos\theta)\exp(2i\sigma_\alpha^l)U_{i\alpha}U_{0\alpha}S_\alpha^l \quad (1.95)$$

Introducing the eigenchannel weights $W_\alpha \equiv U_{0\alpha}^2$, with $\sum W_\alpha = 1$, the physical elastic scattering amplitude can be written:

$$f_{el}(E,\theta) = \sum_\alpha W_\alpha f(\theta,E,B) \equiv \sum_\alpha W_\alpha |f_\alpha^{el}| e^{i\phi_\alpha} \quad (1.96)$$

where ϕ_α are the phases of the complex eigen-channel amplitudes $f_\alpha(\theta, E, B)$.

For the elastic scattering the function

$$G_{el}(E, B) \equiv -\frac{d}{dE}\Big|\frac{f_\alpha}{f_{ruth}}\Big|$$

defines a peaked function similar to the $G_{fus}(E, B)$ and $G_{qel}(E, B)$. If the phases $\phi_\alpha(E)$ did not depend too strong on the eigen-channels α equation (1.96) would yield:

$$D_{el}(E) \equiv -\frac{d}{dE}\Big[\frac{d\sigma_{el}}{d\sigma_{ruth}}(E)\Big]^{1/2} = -\frac{d}{dE}\sum_\alpha W_\alpha\Big|\frac{f_{el}}{f_{ruth}}e^{i\phi_\alpha}\Big| \approx \sum_\alpha W_\alpha G_\alpha^{el} \tag{1.97}$$

The distribution

$$D_{el}(E) \equiv -\frac{d}{dE}\Big[\frac{d\sigma_{el}}{d\sigma_{ruth}}(E)\Big]^{1/2} \tag{1.98}$$

represents the weights and heights of the barriers B_α [72, 73]

Chapter 2

Experimental Details

For the accomplishment of this thesis, two experiments were performed. The first experiment was devoted to the study of the system ^{6,7}Li + ^{28}Si and took place at the *Tandem Accelerator Laboratory* in the Institute of Nuclear Physics (INP) of the *National Centre for Scientific Research "Demokritos"* (NCSRD). The accelerator is an electrostatic Van de Graaff Tandem accelerator with a nomimal maximum operational voltage 5.5 MV, so it is classified as a low energy ion-beam facility. It can accelerate ions from Hydrogen to Oxygen and in the energy range from 1.5 MeV to 40 MeV, depending on the type and the charge state of the ion. It is characterized by high accuracy in the energy of the ion but a relatively small current (a few enA for heavy projectiles and 30 mA protons) [74].

The second experiment was devoted to the study of the systems ^{6,7}Li + ^{58}Ni, ^{116,120}Sn, ^{208}Pb and was performed at the *Laboratori Nazionali del Sud* (LNS) of the *Instituto Nazionale di Fisica Nucleare* in Catania. The accelerator is an electrostatic Van de Graaff HVEC MP Tandem accelerator with a maximum operational voltage 15 MV. Essentially all elements can be accelerated by the SMP Tandem, with the exception of noble gases. The beam has a very good emittance (5p mm mrad) and its energy can easily and continuously be varied. The maximum energy can reach 200 MeV for heavy ions. The maximum current depends on the kind of the ion and the charge states required. It ranges typically from 10 to 200 nA [75].

2.1 The experiment ^{6,7}Li + ^{28}Si

In the present experiment, beams of ^{6,7}Li^{3+} ions were delivered by the TN11/25 HVEC 5.5 MV Tandem accelerator at several bombarding energies from 5 to 12 MeV and intensities of the order of 1-5 nA.

A view of the reaction chamber is shown in Figure 2.1. It has a 2π geometry with two rotational tables and the detectors can be placed in positions

which differ by 10 degrees. The beam from the accelerator entered along the axis of the beam tube and passed through the $0.75m$ diameter scattering chamber into a Faraday cup. The size of the beam was defined by a set of vertical and horizontal slits. The beam spot had a radius of 0.4 cm.

The detector arrangement for the present experiment is presented in figure 2.1. It consists of six silicon detectors, two at forward angles and four at backward angles. The forward detectors were placed at ± 30 degrees and the distance between them and the target holder was approximately 17 cm. The backward detectors were placed at ± 150 and ± 170 degrees in a distance of 18.7 cm from the target holder. In front of each detector a circular mask was placed with inner diameter 8 mm. Detectors were set up in couples at symmetrical positions, both to increase the statistics and mainly to correct any beam diversities.

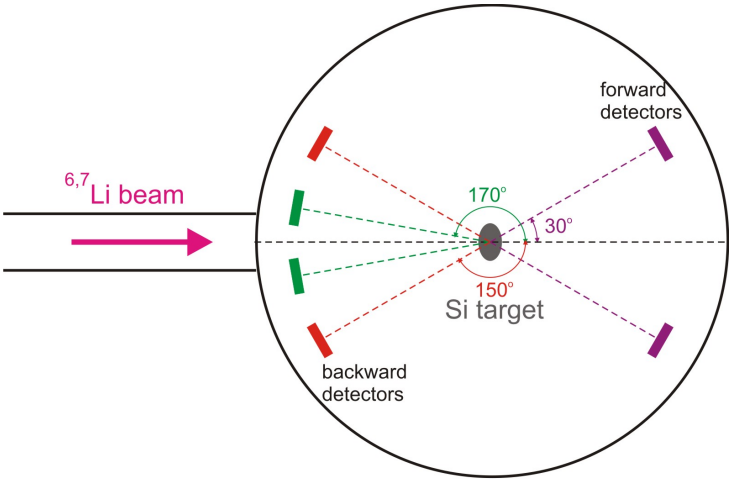

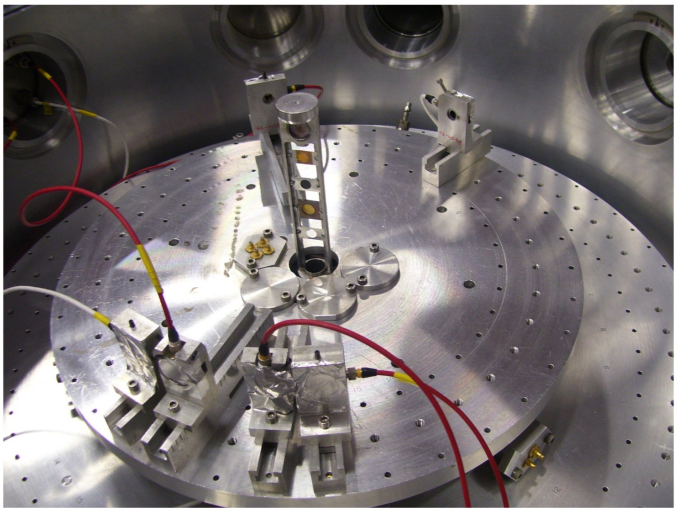

Figure 2.1: *Schematic view and photo of the scattering chamber at Demokritos.*

The Si targets were mounted in a target ladder, at the center of the chamber, which holds the targets vertically aligned above one another as shown in figure 2.2. The ^{28}Si and Au targets placed in the chamber were 200 $\mu g/cm^2$ thick self-supporting foils. The Au target was used for the determination of solid angle, as it will be described in the next chapter. The last place of the target holder was left empty in order to achieve better alignment of the beam and avoid scattering in the target holder. By changing the height of the ladder, any of the targets can be positioned in the beam. The target frame can be also rotated about its own vertical axis to select the target angle with respect to the beam direction, but in that experiment it was fixed perpendicular to the beam direction.

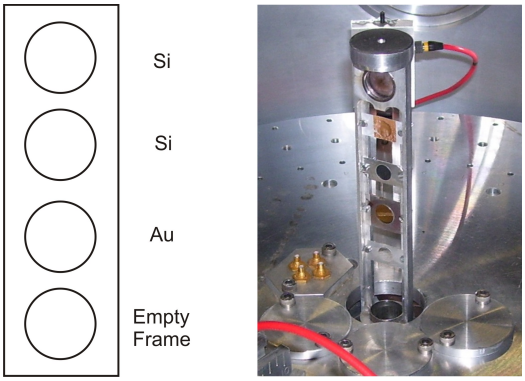

Figure 2.2: *Schematic representation of the target holder and photo with the targets.*

The detectors used in that experiment were surface barrier silicon detectors (see Appendix B), which were obtained from Oak Ridge Technical Enterprises Corporation (ORTEC). The characteristics of the 6 silicon detectors are given in the Table 2.1

Table 2.1: *Characteristics of the 6 silicon detectors used in the first experiment at Demoktitos center.*

Detector	Active Area (mm^2)	Sensitive thickness (μm)	Noise width FWHM (keV)	Bias Voltage (V)
EBR150 [1]	50	72.4	19.8	20
EBR170 [1]	50	87	21	30
EBL150 [1]	50	90.5	21.54	30
EBL170 [1]	50	50	0.42	30
EFR [2]	150	100	105	20
EFL [2]	150	200	9.0	100

[1]EBR150 stands for a detector set backward at 150 degrees, right to the beam direction and so on.

[2]EFR stands for a detector set forward, right to the beam direction and EFL for a detector stands forward, left.

Detectors provide a variety of information on detected radiation in the form of electrical pulse signals. In order to extract the information provided by the detectors, the signal must be further processed by an electronic system. In figure 2.3 it is shown a simplified illustration of the electronic chain used in this experiment.

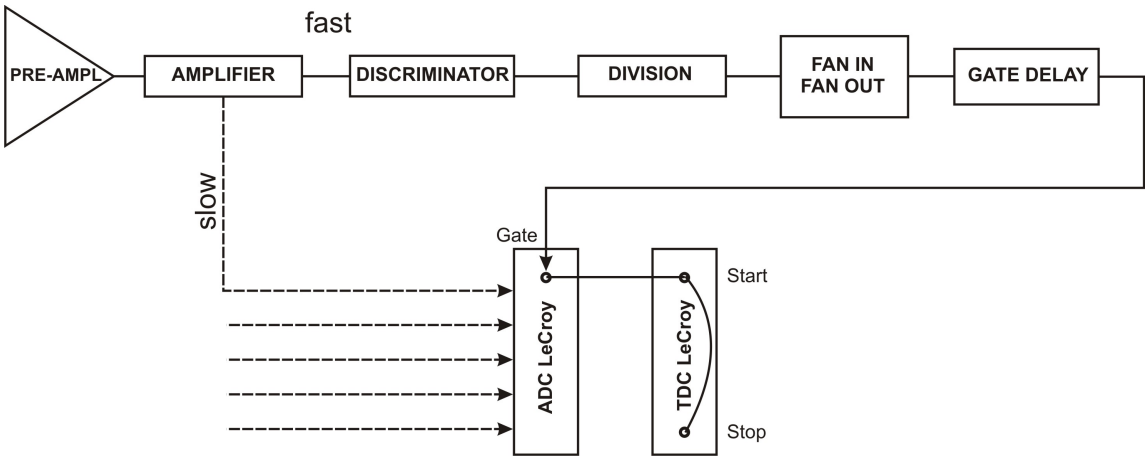

Figure 2.3: *Schematic representation of the electronic modules used in the experiment.*

The outputs of the six silicon detectors were connected to a preamplifier (ORTEC 142). The function of the preamplifier is to provide an interface between the detector and the pulse processing electronics, amplifing weak signals from the detectors and to shape the subsequent output pulses. In order to reduce electronic noise, the preamplifiers were placed just out of the scattering chamber and covered with an aluminum foil for better contact with earth.

The linear output signals from the silicon preamplifier were fed to an amplifier (CAEN N979) which used to supply both energy and timing signals. The energy signals from the amplifier were digitized by a LECROY NIM ADC (2249A 12 channels ADC). The timing signals were fed to a CAEN low threshold discriminator (CAEN N845), then to a division and to a FAN IN - FAN OUT (CAEN N454). Subsequently, this OR signal was fed to an ORTEC Gate and Delay Generator and the output was used as a gate to the ADC. The data were recorded in the PC controlled acquisition system, CAMDA [76] and were analyzed off line. For the stability of the particular acquisition system the LAM (Look At Me) signal was assigned to a dummy unit, a TDC, where the Gate itself was used to start and stop this unit (see figure 2.3).

2.2 The experiment ^{6,7}Li + ^{58}Ni, ^{116,120}Sn, ^{208}Pb

The present experiment was performed in the 2 m diameter multi-purpose vacuum chamber along the 60 degree beam line in Catania. Beams of ^{6,7}Li were delivered by the SMP Tandem accelerator at 0.5 MeV steps in the energy range from 9 to 36 MeV. Specifically for the nickel target the energy range was from 9 to 20 MeV, for the tin targets from 12 to 26 MeV and for the lead target from 18 to 36 MeV. Beam currents were of the order of 5 to 20 nA depending on energy. The size of the beam was defined by a set of vertical and horizontal slits.

The target ladder at the center of the chamber was able to hold three different targets and an empty frame (see figure 2.4) vertically aligned and it was fixed perpendicular to the beam direction. The targets placed in the chamber were 200 $\mu g/cm^2$ thick self-supporting pure isotopic ^{58}Ni,^{116,120} Sn and ^{208}Pb foils.

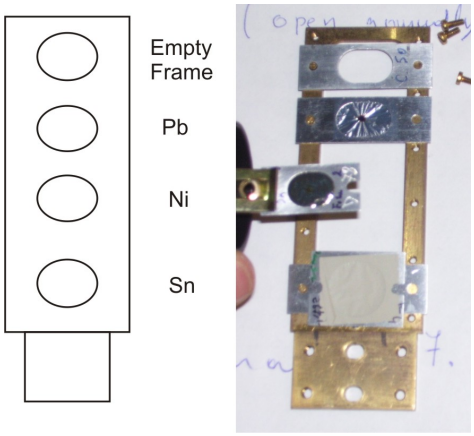

Figure 2.4: *Schematic representation and photo of the target holder.*

The detection system consisted of two monitors (single detectors) at forward angles and four telescopes at backward angles. The detection system is shown in figure 2.5. The monitors were 2000 μm silicon detectors set at $\pm$20 degrees. The four telescopes were set at $\pm$160 and $\pm$170 degrees and were consisted of two parts. The first part was a thin silicon detector of about 10 μm thickness (ΔE) and the second part was a thick detector of 3000 μm thickness (E). The first part of the telescope absorbs a part of the recoil ions, allowing a Z separation via the $\Delta E - E$ technique. The monitors abstained from the target holder 80 cm and in front of each one was placed a circular tantalum mask with diameter 4 mm. The 160 degrees telescopes abstained from the target holder 21 cm and the 170 degrees 16.5 cm. In front of each telescope was placed a copper mask with diameter 7 mm. All the detectors used in this experiment were Silicon Surface Barrier Detectors (SSB) from Oak Ridge Technical Enterprises Corporation (ORTEC). The characteristics of the ten silicon detectors are given in Table 2.2

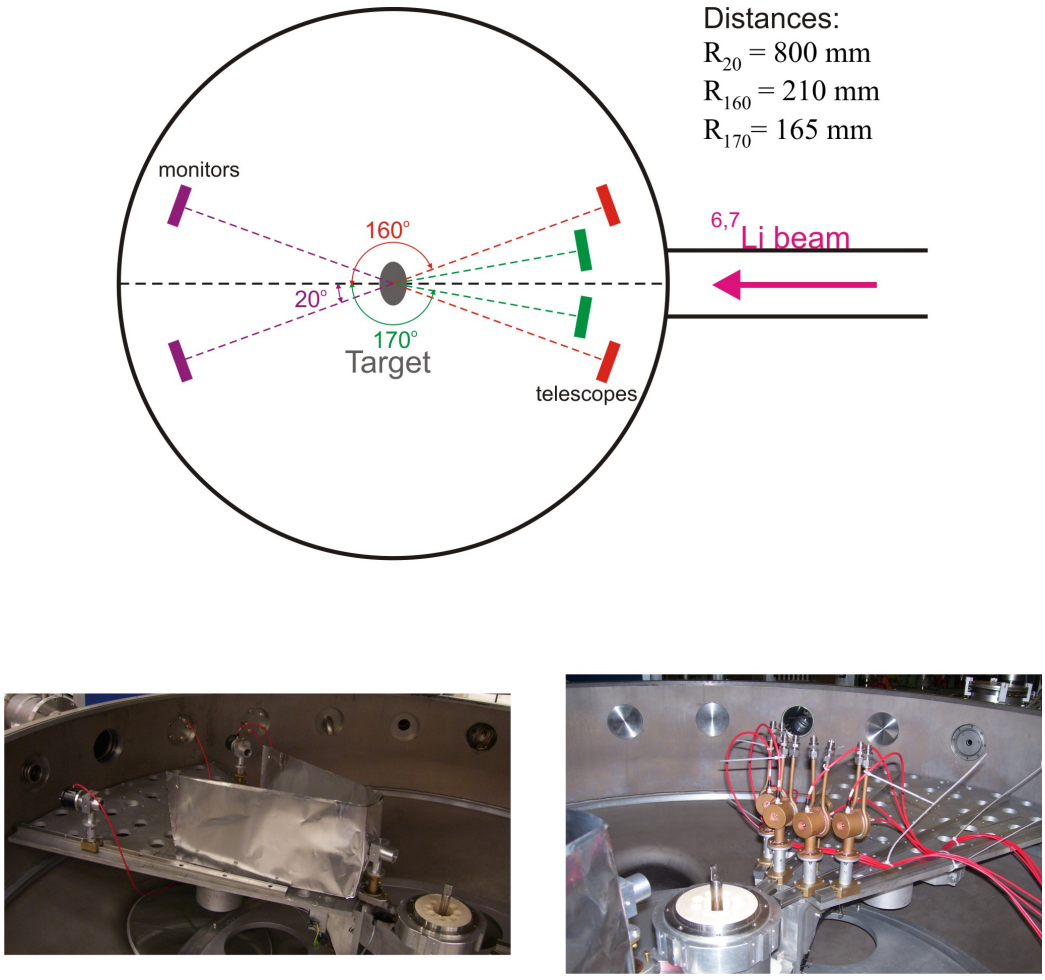

Figure 2.5: *Schematic view and photos of the scattering chamber in Catania.*

In figure 2.6, it is shown a simplified illustration of the electronic modules. The outputs of the ten silicon detectors (two monitors, four double stage telescopes) were connected to their own preamplifier. With E are noted the outputs of two monitors and the first part of the telescopes while with ΔE the outputs of the second parts of the telescopes. The linear output signals from the silicon preamplifier were fed to a Silena 761 amplifier which were used to supply both energy and timing signals.

The energy signals from the amplifier were digitized by a Silena ADC. The timing signals were fed to a CAEN discriminator (CAEN 8 channels discriminator N413A), an OR is made of the 6 discriminator outputs and is then duplicated by a FAN IN/OUT. These 2 equal signals represent the valid event, one is going to the SCALER and the other to a homemade Acquisition trigger module. This module gives an output every time there is an input and the acquisition is not in dead time. The output of the acquisition trigger module is duplicated in a FAN IN/OUT and goes to a scaler (acquired events) and to the Gate and Delay Generator which provides the ADC gate.

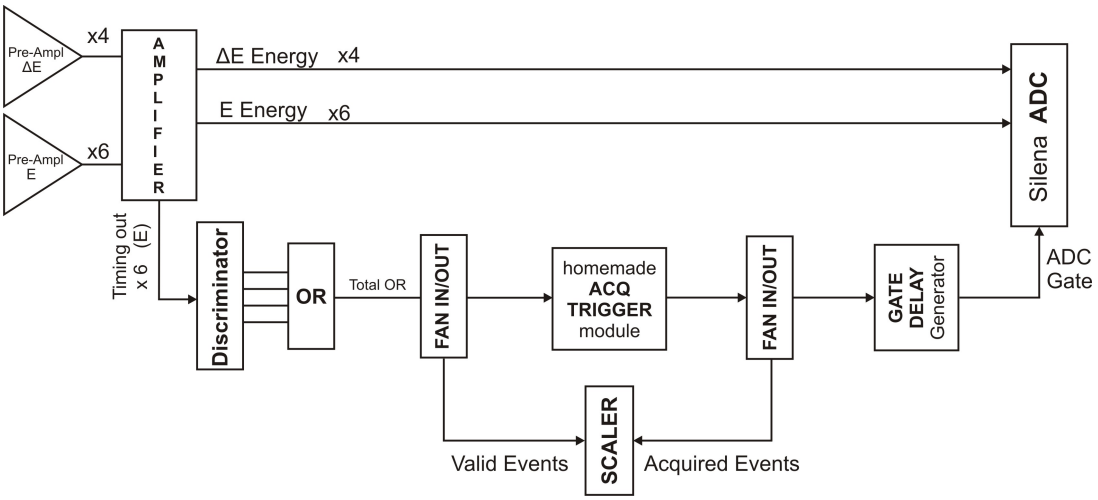

Figure 2.6: *Schematic representation of the electronic modules used in the experiment performed at LNS.*

Table 2.2: *Characteristics of the 10 silicon detectors used in the second experiment at LNS.*

Detector	Active Area (mm^2)	Sensitive thickness (μm)	Noise width FWHM (keV)	Bias Voltage (V)
EFR [3]	50	2000	12	300
EFL [3]	50	2000	12	300
EBR160 [4]	200	3000	16	300
ΔEBR160 [5]	50	6.5	7	5
EBR170 [4]	200	3000	20	400
ΔEBR170 [5]	50	7.9	10	5
EBL160 [4]	200	3000	20	400
ΔEBL160 [5]	50	10.6	35	5
EBL170 [4]	200	3000	17	300
ΔEBL170 [5]	50	9.6	35	5

[3]EFR stands for a detector set forward, right to the beam direction and EFL for a detector stands forward, left.

[4]EBR160 stands for the silicon detector at the second part of the telescope, set backward at 160 degrees, right to the beam direction and so on.

[4]ΔEBR160 stands for the silicon detector at the first part of the telescope, set backward at 160 degrees, right to the beam direction and so on.

Chapter 3

Data Reduction

For the application of the new technique, proposed in this study, excitation functions of elastic backscattering are determined and barrier distributions are formed. The last will be used as a tool for probing the potential threshold anomaly for weakly bound nuclei, and for extending the energy dependence of the optical potential at sub-barrier energies. In the following we present details for the data reduction, leading to barrier distributions of $^{6,7}Li$ elastic backscattering on various targets.

3.1 Energy calibration

The main step of an accurate data reduction is a good energy calibration of the detectors. In general, calibration is performed by using the peaks of a known source. As the channel number is proportional to energy, the channel scale can be converted into an energy scale by assuming the following linear relatinship:

$$Energy = A * (channel) + B \tag{3.1}$$

where A, B are parameters which are identified by the fit.

In both experiments, the energy calibration of each detector was made by using a triple alpha source and a pulser. The pulser was calibrated through the alpha source and the detectors via the pulser in a wide energy range. The triple alpha source was composed of ^{244}Cm, ^{241}Am and ^{240}Pu. The main α-peaks of this source, coming from the first excited states of the daughter nuclei, correspond to 5.805 MeV, 5.486 MeV and 5.168 MeV respectively. The pulser generates a pulse of certain voltage. Assuming a linear relationship between the channel number and the energy of a particle deposited in the detector, one can vary the voltage of the pulses and gets the energy calibration of the detectors. In figures 3.1 and 3.2 are shown the spectra which are taken from the calibration of forward and backward detectors with the triple source, during the second experiment. The spectra of the first experiment

have the same structure.

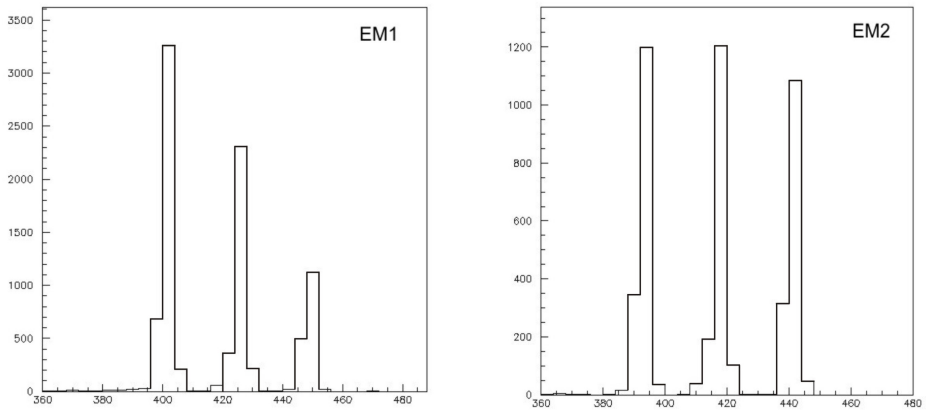

Figure 3.1: *Calibration spectra collected with a triple alpha-source (^{244}Cm, ^{241}Am and ^{240}Pu) from the monitors.*

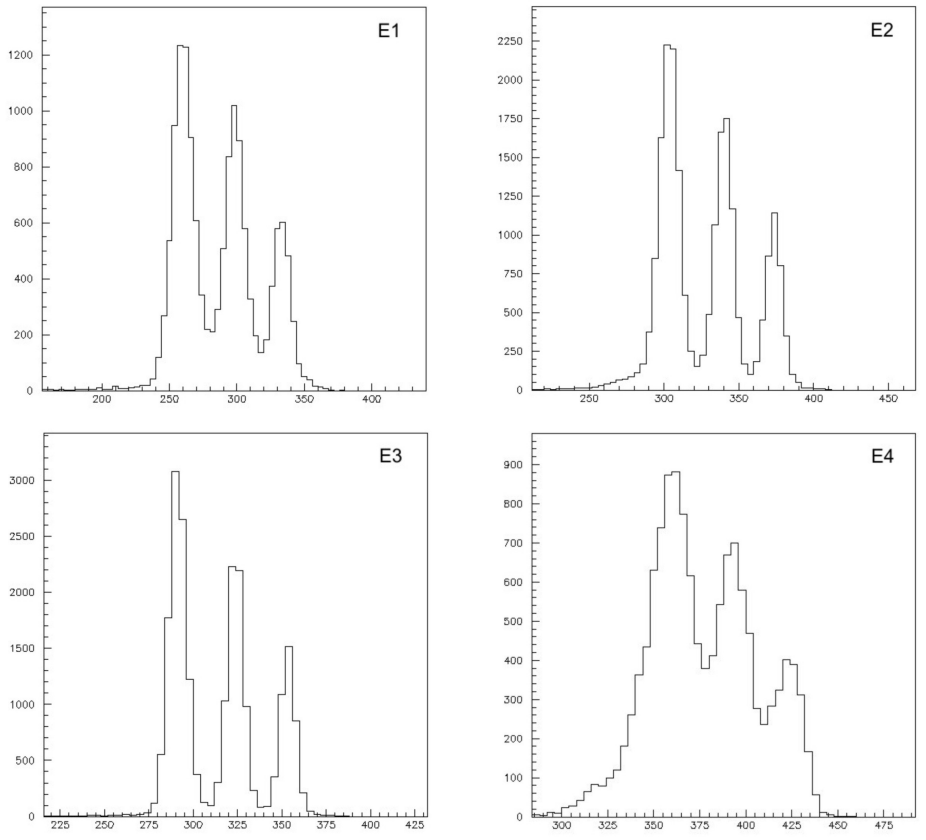

Figure 3.2: *Calibration spectra collected with a triple alpha-source (^{244}Cm, ^{241}Am and ^{240}Pu) from the backward detectors.*

In tables 3.1 and 3.2 it is shown the calibration of all the detectors which were used in both experiments. For each detector the energy as a function of the channel number is calculated.

Table 3.1: *Calibration of the detectors used for the* $^{6,7}Li + ^{28}Si$ *experiment.*

Detector	$Energy = A * (channel) + B$
EFR [1]	$E = 0.0245 * ch - 1.4472$
EFL [1]	$E = 0.02271 * ch - 1.2436$
EBR 150 [2]	$E = 0.0138 * ch - 1.0869$
EBR 170 [2]	$E = 0.0134 * ch - 0.9986$
EBL 150 [2]	$E = 0.014 * ch - 1.1615$
EBL 170 [2]	$E = 0.0143 * ch - 1.1295$

Table 3.2: *Calibration of the detectors used for the* $^{6,7}Li + {}^{58}Ni$, $^{116,120}Sn$, ^{208}Pb *experiment.*

Detector	$Energy = A * (channel) + B$
EFR [1]	$E = 0.0133 * ch - 0.1551$
EFL [1]	$E = 0.0131 * ch + 0.0048$
EBR 160 [2]	$E = 0.0108 * ch + 0.6403$
EBR 170 [2]	$E = 0.0118 * ch + 0.4867$
EBL 160 [2]	$E = 0.0109 * ch + 0.3367$
EBL 170 [2]	$E = 0.0116 * ch + 0.0014$

3.2 Identification of reaction channels

The data analysis was performed with the program PAW (Physics Analysis Workstation). Taking into account the kinematics of the colliding ions and the energy losses, in the target and in the detectors, the identification of the various reaction channels was performed. Furthermore, in the second experiment the identification of the various channels was based on the $\Delta E - E$ technique.

In the first experiment the systems $^{6}_{3}Li + {}^{28}_{14}Si$ and $^{7}_{3}Li + {}^{28}_{14}Si$ were studied. Since the energies were low $(5 - 11 MeV)$, it was not possible to use telescopes and the identification of elastic peak was achieved by the calibration. In figure 3.3, they are presented typical 1-dimension spectra of one monitor and one backward detector in low beam energy $(E = 6\, MeV)$. As it can be seen in the figure, at the left of the elastic peak of the monitors, a smaller peak is distinguished which is due to the scattering of Li by the oxygen contamination of the target. This peak is not observed at the backward detectors because the resolution is not so good but it was estimated from the forward detectors and subtracted accordingly. This correction was not more

[1] EFR stands for a detector set forward, right to the beam direction and EFL for a detector stands forward, left.

[2] EBR160 stands for the silicon detector at the second part of the telescope, set backward at 160 degrees, right to the beam direction and so on.

than 2 per cent.

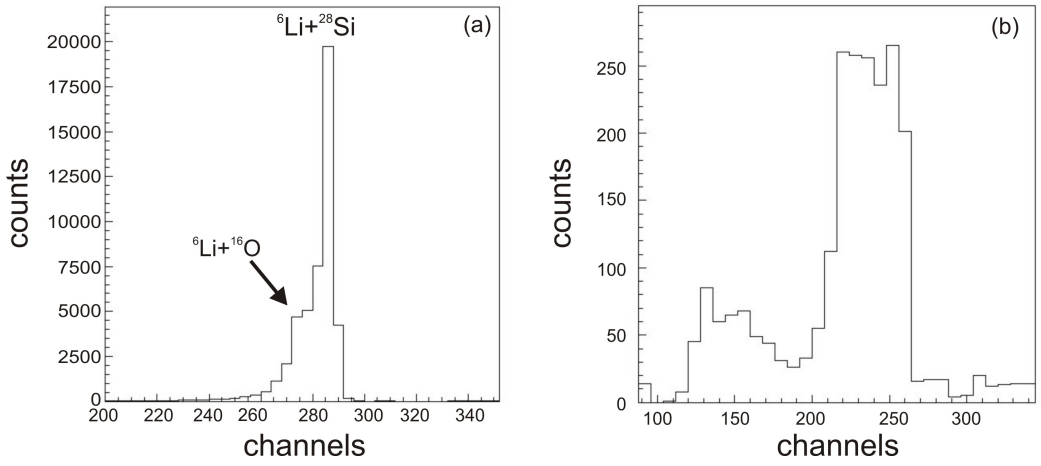

Figure 3.3: *Typical spectra for the system* $^6_3Li + ^{28}_{14}Si$ *at* $E = 6MeV$ *a) for monitor b) for backward detector.*

In figure 3.4, 1-dimension spectra are also presented, for a higher beam energy ($E = 8\,MeV$). Due to the lower cross section, a large background under the elastic peak is now obvious which mainly originates from scattering and other reaction processes. In the particle spectra obtained in the reaction $^6_3Li + ^{28}_{14}Si$ 11. no peak is observed which can be attributed to inelastic scattering. For $^7_3Li + ^{28}_{14}Si$ the 0.478 MeV $1/2^-$ inelastic peak was not resolved and the results are quasi-elastic rather than elastic.

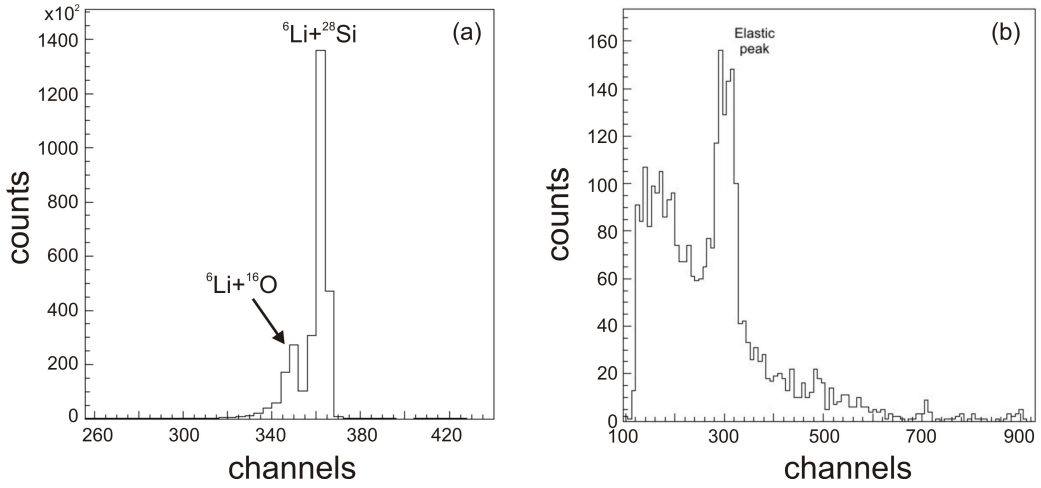

Figure 3.4: *Spectra for the system* $^6_3Li + ^{28}_{14}Si$ *at* $E = 8MeV$ *a) for monitor b) for backward detector.*

In the second experiment the systems: $^6_3Li + ^{58}_{28}Ni$, $^6_3Li + ^{120}_{50}Sn$, $^6_3Li + ^{208}_{82}Pb$, $^7_3Li + ^{58}_{28}Ni$, $^7_3Li + ^{116,120}_{50}Sn$ and $^7_3Li + ^{208}_{82}Pb$ were studied. In figure 3.5 it is presented a typical 2-dimensions spectrum of one backward detector. Results of the different atomic numbers are easily distinguished. In figure 3.6 it is shown the projection of the elastic peak in 1-dimension.

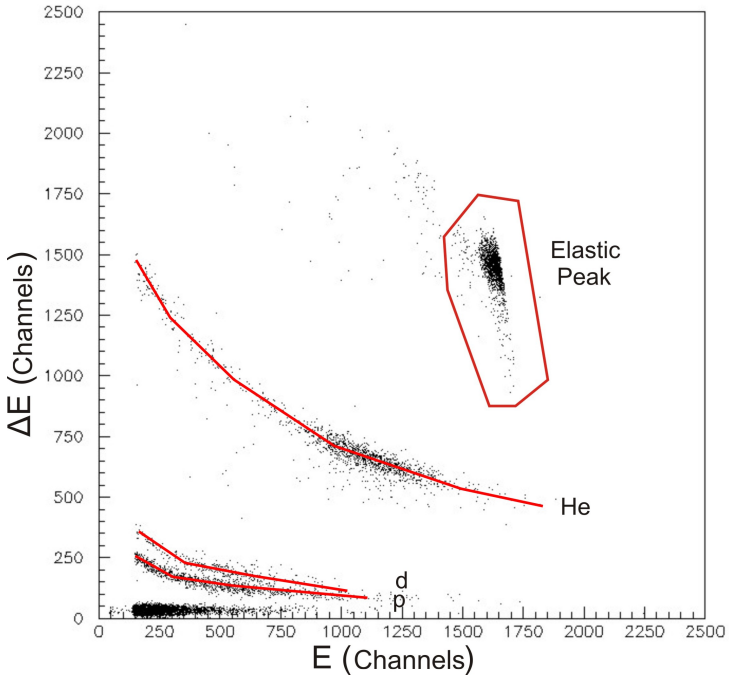

Figure 3.5: *Typical 2-dimension spectrum for* ${}^{6}_{3}Li + {}^{208}_{82}Pb$ *at* $24\ MeV$.

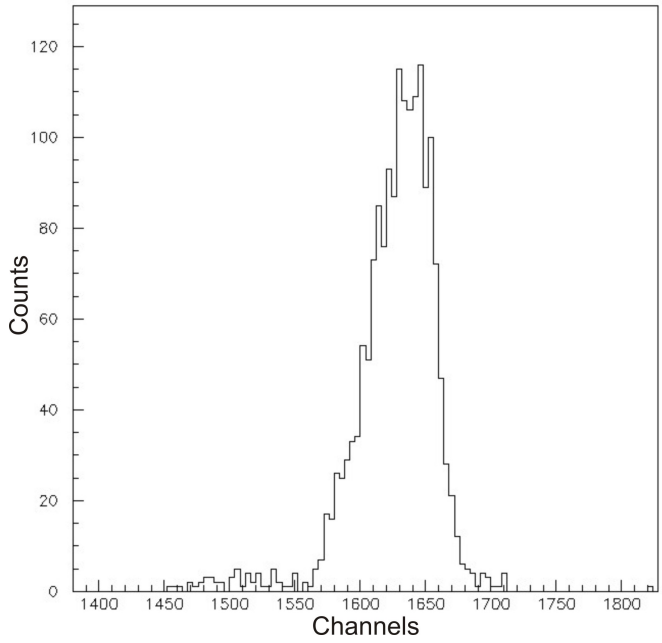

Figure 3.6: *Projection of the previous contour on 1-dimension.*

3.3 Determination of solid angle using gold and lead

In principle, for ideal conditions of point source, the solid angle is given by the relation:

$$\Omega = \frac{S}{R^2} \tag{3.2}$$

where S is the surface of the detector and R the distance between the detector and the target. The error in solid angle is:

$$\delta\Omega = \sqrt{\Big(\frac{1}{R^2}\delta S\Big)^2 + \Big(-\frac{2S}{R^3}\Big)^2} \tag{3.3}$$

In the present study, an alternative, more accurate way was used to measure the ratio Ω_f/Ω_b, where Ω_f is the solid angle of the forward detector (monitor) and Ω_b is the solid angle of the backward detector, via the known Rutherford scattering of $^{6,7}Li$ on heavy targets like gold and lead. The ratio of solid angles was determined, during the first experiment, by the scattering of $11\,MeV$ lithium ions from a thin gold target. The elastic scattering of gold at this energy is pure Rutherford for both forward and backward detectors, and the ratio of solid angles can be determined with negligible errors. The ratio is given by the relation:

$$\frac{\Omega_f}{\Omega_b} = \frac{N_{Gf}\cdot\sigma_{GRuth(b)}}{N_{Gb}\cdot\sigma_{GRuth(f)}} \tag{3.4}$$

where N_{Gf}, N_{Gb} stands for the the counting rate of the forward and backward detectors. The σ_{Ruth} calculations were performed with the LISE++ program assuming that the reaction took place at the middle of the target.

In the previous relation the only contributing errors come from the counting rate. These errors are very small because the scattering to the gold foil is weak. The errors of this ratio are:

$$\delta(\frac{\Omega_f}{\Omega_b}) = \sqrt{\Big(\frac{1}{N_{Gb}}\frac{\sigma_{GRuth(b)}}{\sigma_{GRuth(f)}}\delta N_f\Big)^2 + \Big(-\frac{N_{Gf}}{N_{Gb}^2}\frac{\sigma_{GRuth(b)}}{\sigma_{GRuth(f)}}\delta N_b\Big)^2} \tag{3.5}$$

In the second experiment, instead of gold, data were collected with a lead target at low beam energy, $E = 18,\ 20,\ 21\,MeV$ where the scattering is pure Rutherford for both forward and backward detectors.

Tables 3.3 and 3.4 contain solid angle ratios with both methods for the Demokritos and Catania experiments respectively. It can be seen that the results of the two methods are compatible, however for this study ratios obtained with the Rutherford method were adopted.

Table 3.3: *Ratio of solid angles calculated taking into account the setup geometry and the Rutherfotd scattering on gold, for the Demokritos experiment.*

Solid angles	$\Omega_f/\Omega_b(L150)$	$\Omega_f/\Omega_b(L170)$	$\Omega_f/\Omega_b(R150)$	$\Omega_f/\Omega_b(L170)$
Geometry method	0.9345	0.987	0.8035	0.857
Rutherford meth.	0.9126	1.0518	0.774	0.827

Table 3.4: *Ratio of solid angles calculated taking into account the setup geometry and the Rutherfotd scattering on lead, for the Catania experiment.*

Solid angles	$\Omega_f/\Omega_b(L160)$	$\Omega_f/\Omega_b(L170)$	$\Omega_f/\Omega_b(R160)$	$\Omega_f/\Omega_b(L170)$
Geometry method	0.023	0.0137	0.0226	0.0142
Rutherford meth.	0.02	0.0132	0.0221	0.0139

3.4 Determination of cross-section

The cross section gives the probability for a reaction to take place. The cross section, as shown in section 1.1.5, is given by the following formula:

$$\sigma = \frac{0.267 \cdot 10^{-6} \cdot A \cdot charge\ state \cdot N}{Q \cdot \tau \cdot efficiency \cdot \Omega}\ (mb) \tag{3.6}$$

where A is the mass number of the target, N the number of counts, Q the charge in μCb, τ the target thickness in mg/cm^2 and Ω the solid angle. For the forward angles we have Rutherford scattering so:

$$Q \cdot \tau = \frac{0.267 \cdot 10^{-6} \cdot A \cdot charge\ state \cdot N_f}{\sigma_{fRuth} \cdot efficiency \cdot \Omega_f} \tag{3.7}$$

where the σ Rutherford is known. Replacing that in equation (3.6) it yields:

$$\sigma_{backward} = \frac{N_b}{N_f}\frac{\Omega_f}{\Omega_b}\sigma_{fRuth} \tag{3.8}$$

The above formula is not depended on the flux of the beam or the thickness of the target. Dividing with σ Rutherford at backward angles it yields:

$$\frac{\sigma_{backward}}{\sigma_{BRuth}} = \frac{N_b}{N_f}\frac{\Omega_f}{\Omega_b}\frac{\sigma_{fRuth}}{\sigma_{BRuth}} \tag{3.9}$$

The determination of the ratio Ω_f/Ω_b was given in the previous section.

The quantities $N_f, N_b, \Omega_f/\Omega_b$ have the uncertainties $\delta N_f, \delta N_b, \delta(\Omega_f/\Omega_b)$, so the error in (3.8) is:

$$\Delta\sigma_b = \sqrt{\Big(\frac{\partial\sigma_q}{\partial N_b}\delta N_b\Big)^2 + \Big(\frac{\partial\sigma_q}{\partial N_f}\delta N_f\Big)^2 + \Big(\frac{\partial\sigma_q}{\partial(\Omega_f/\Omega_b)}\delta(\frac{\Omega_f}{\Omega_b})\Big)^2} \tag{3.10}$$

$$\begin{aligned}\Delta\sigma_b = &\Big[\Big(\frac{\sigma_{fRuth}}{N_f}\frac{\Omega_f}{\Omega_b}\delta N_b\Big)^2 + \Big(-\frac{\sigma_{fRuth}N_b}{N_f^2}\frac{\Omega_f}{\Omega_b}\delta N_f\Big)^2 + \sigma_{fRuth}\frac{N_b}{N_f}\Big(\frac{1}{N_{Gb}}\frac{\sigma_{GRuth(b)}}{\sigma_{GRuth(f)}}\delta N_f\Big)^2 \\ &+ \sigma_{fRuth}\frac{N_b}{N_f}\Big(-\frac{N_{Gf}}{N_{Gb}^2}\frac{\sigma_{GRuth(b)}}{\sigma_{GRuth(f)}}\delta N_b\Big)^2\Big]^{1/2}\end{aligned} \tag{3.11}$$

The quantity $\frac{\sigma_{backward}}{\sigma_{BRuth}}$ was calculated for each backward detector. For the final cross section the weighted mean of $\frac{\sigma_{backward}}{\sigma_{BRuth}}$ was estimated, which is given by the following formula:

$$f_{mean} = \frac{\sum_i f_i/\sigma_i^2}{\sum_i 1/\sigma_i^2} \tag{3.12}$$

The error is:

$$\sigma_{mean} = \frac{1}{\sum_i 1/\sigma_i^2} \tag{3.13}$$

3.5 Experimental excitation functions of $d\sigma/d\sigma_R$

Excitation functions of measured elastic backscattering cross sections versus Rutherford are presented in the following figures for all systems. The results are error-weighted means of the cross sections obtained at 150 and 170 degrees for the $^{6,7}Li + {}^{28}Si$ and at 160 and 170 degrees for the $^{6,7}Li + {}^{58}Ni$, ^{120}Sn, ^{208}Pb. This was done to increase the statistics and it was possible, since the energy centrifugal correction was negligible for these angles. For comparison purposes the energy is given as a ratio to the Coulomb barrier. Coulomb barriers were calculated according to Broglia [77].

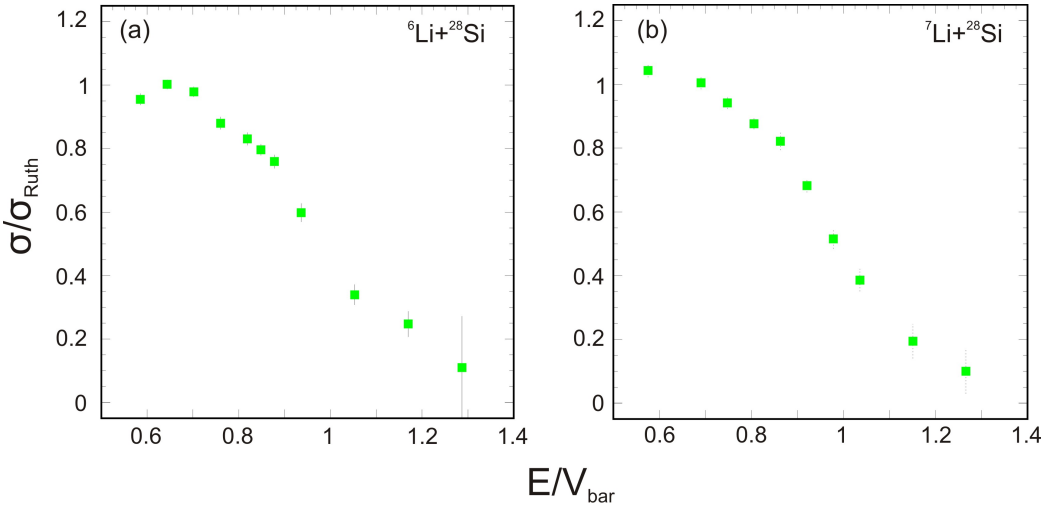

Figure 3.7: *a) Excitation function for the system $^{6}Li + {}^{28}Si$. The Coulomb barrier is $V_{bar}^{lab} = 8.54\ MeV$. b) Excitation function for the system $^{7}Li + {}^{28}Si$. The Coulomb barrier is $V_{bar}^{lab} = 8.69\ MeV$.*

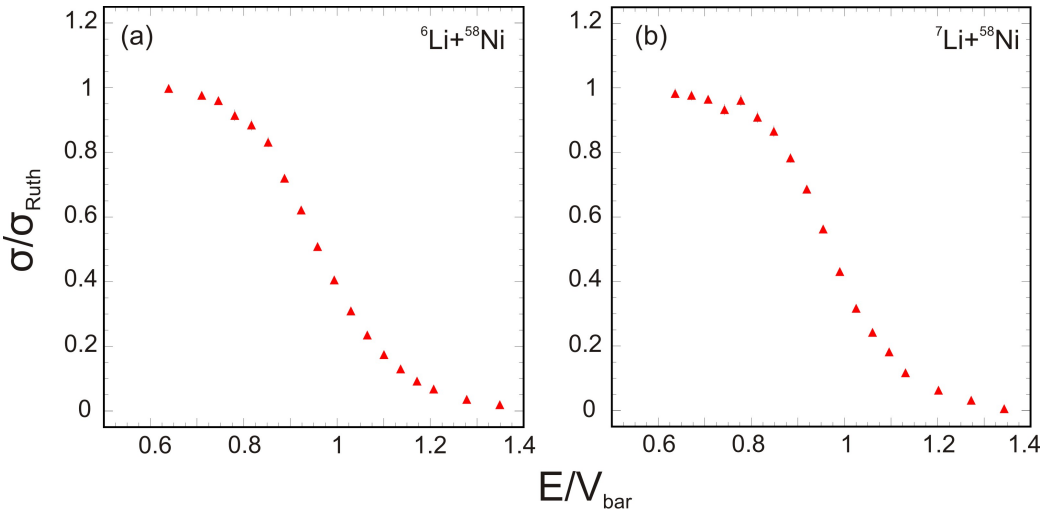

Figure 3.8: *a) Excitation function for the system* $^{6}Li+\ ^{58}Ni$*. The Coulomb barrier is* $V_{bar}^{lab} = 14.07\ MeV$*. b) Excitation function for the system* $^{7}Li+\ ^{58}Ni$*. The Coulomb barrier is* $V_{bar}^{lab} = 14.14\ MeV$*.*

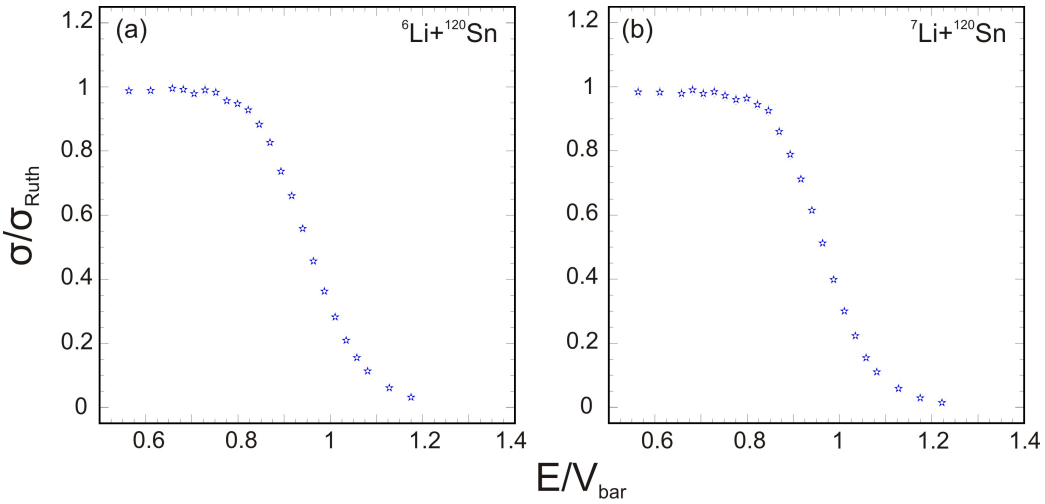

Figure 3.9: *a) Excitation function for the system* $^{6}Li+\ ^{120}Sn$ *The Coulomb barrier is* $V_{bar}^{lab} = 21.37\ MeV$*. b) Excitation function for the system* $^{7}Li+\ ^{120}Sn$*. The Coulomb barrier is* $V_{bar}^{lab} = 21.33\ MeV$*.*

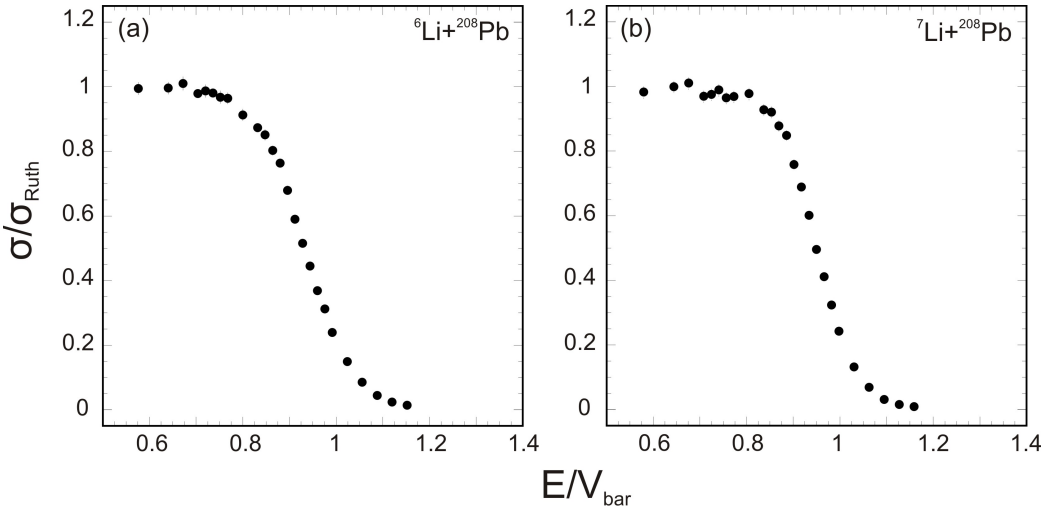

Figure 3.10: *a) Excitation function for the system* $^{6}Li + {}^{208}Pb$ *The Coulomb barrier is* $V_{bar}^{lab} = 31.22\ MeV$. *b) Excitation function for the system* $^{7}Li + {}^{208}Pb$. *The Coulomb barrier is* $V_{bar}^{lab} = 31.1\ MeV$.

3.6 Experimental barrier distribution

As it is shown in Chapter 1, the representation of barrier distribution can be obtained from quasi-elastic and elastic backscattering excitation functions through the first derivative:

$$D_{qel}(E) = -\frac{d}{dE}\Big[\frac{d\sigma_{qel}}{d\sigma_{ruth}}(E)\Big] \tag{3.14}$$

$$D_{el}(E) \equiv -\frac{d}{dE}\Big[\frac{d\sigma_{el}}{d\sigma_{ruth}}(E)\Big]^{1/2} \tag{3.15}$$

In ^{6}Li the scattering was elastic and in the ^{7}Li quasi-elastic. But for reasons of comparison and because the inelastic scattering in ^{7}Li was small, the representation of barriers from elastic scattering was used for both projectiles by using relation (3.14).

The relevant derivative was determined by adopting a point-difference formula [78]. Denoting $d\sigma/d\sigma_{Ruth}$ by $-f(E)$ for two energy values E_1 and E_2 we have,

$$D_{el}(E') = \frac{f(E_2) - f(E_1)}{E_2 - E_1} \tag{3.16}$$

where $E' = 1/2(E_2 + E_1)$ and an associated error:

$$\delta D_{el}(E') = \frac{(\delta f_2^2 - \delta f_1^2)^{1/2}}{E_2 - E_1} \tag{3.17}$$

In figures 3.11 - 3.14 the calculated barrier distributions $D(E)$ are depicted, for all the systems. Finally, in figure 3.15 the barrier distributions for the two different isotopes of Sn are shown. These results indicate that there is no difference between the two isotopes at least in the context of the barrier distribution method and no further consideration of ^{116}Sn was pursued.

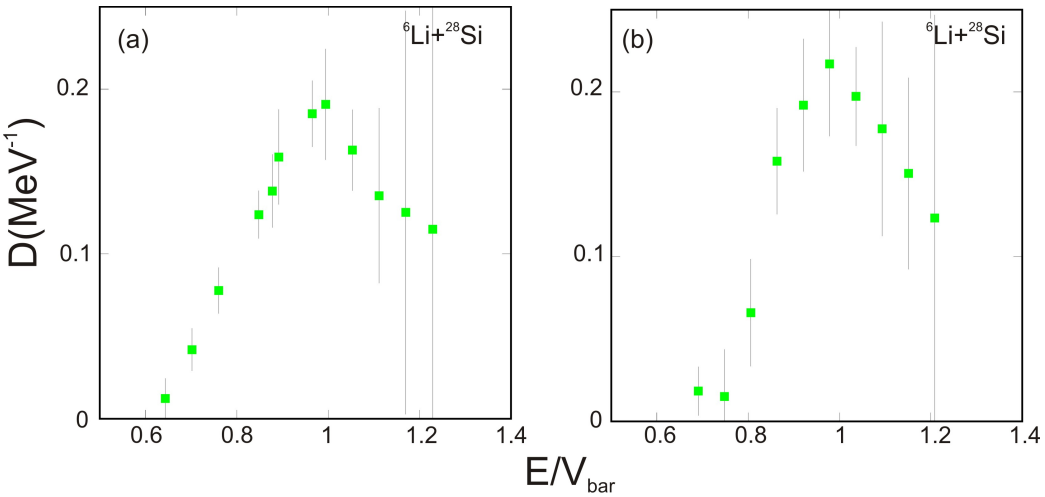

Figure 3.11: *a) Barrier distribution for the system $^{6}Li + {}^{28}Si$. b) Barrier distribution for the system $^{7}Li + {}^{28}Si$.*

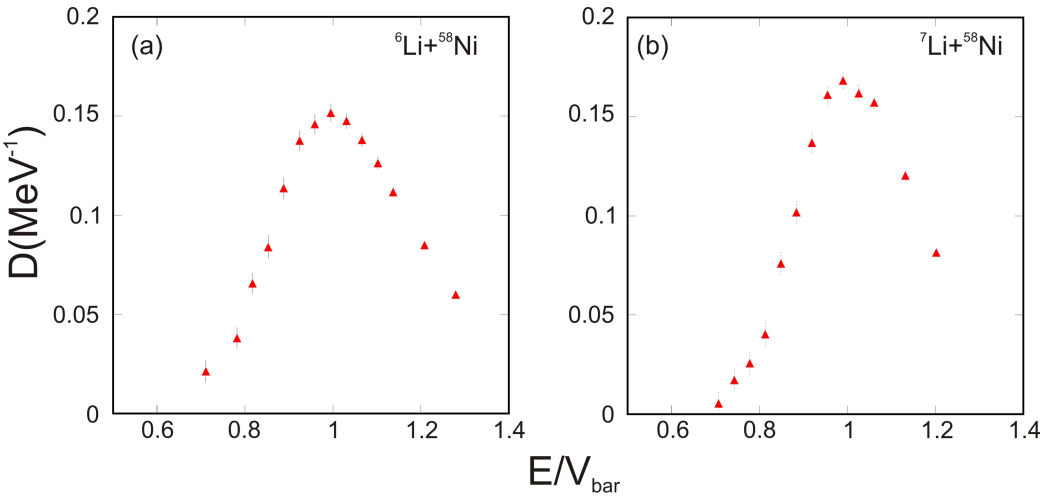

Figure 3.12: *a) Barrier distribution for the system $^{6}Li + {}^{58}Ni$. b) Barrier distribution for the system $^{7}Li + {}^{58}Ni$.*

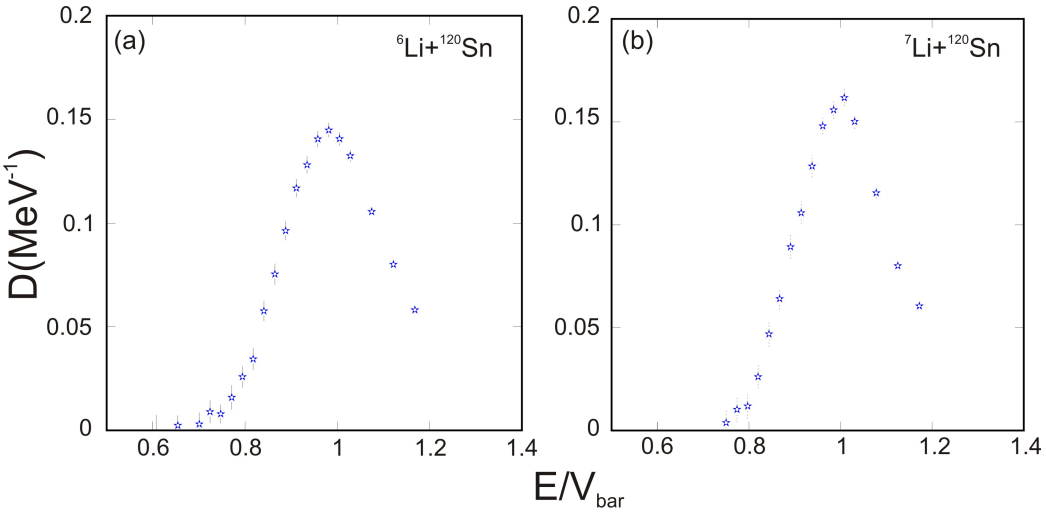

Figure 3.13: *a) Barrier distribution for the system* $^{6}Li + {}^{120}Sn$*. b) Barrier distribution for the system* $^{7}Li + {}^{120}Sn$*.*

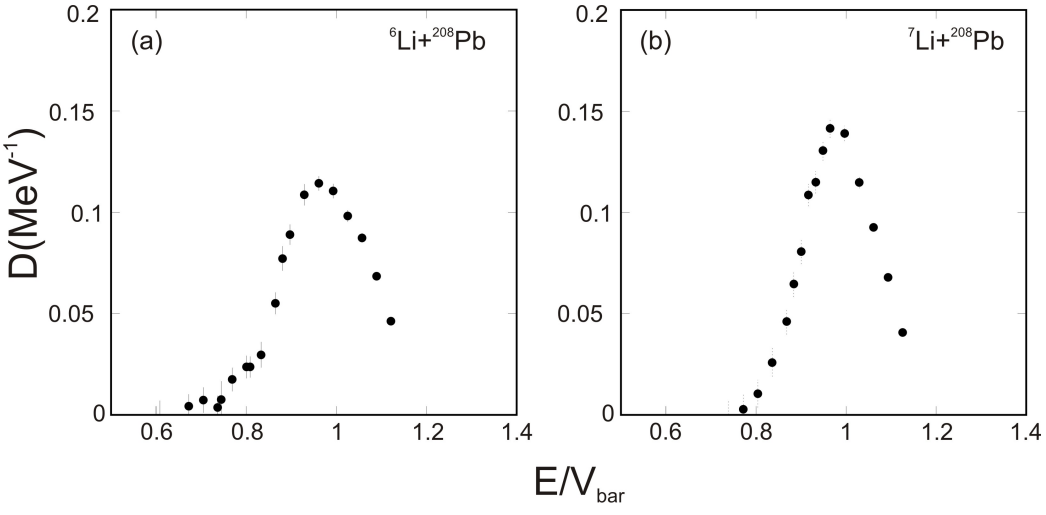

Figure 3.14: *a) Barrier distribution for the system* $^{6}Li + {}^{208}Pb$*. b) Barrier distribution for the system* $^{7}Li + {}^{208}Pb$*.*

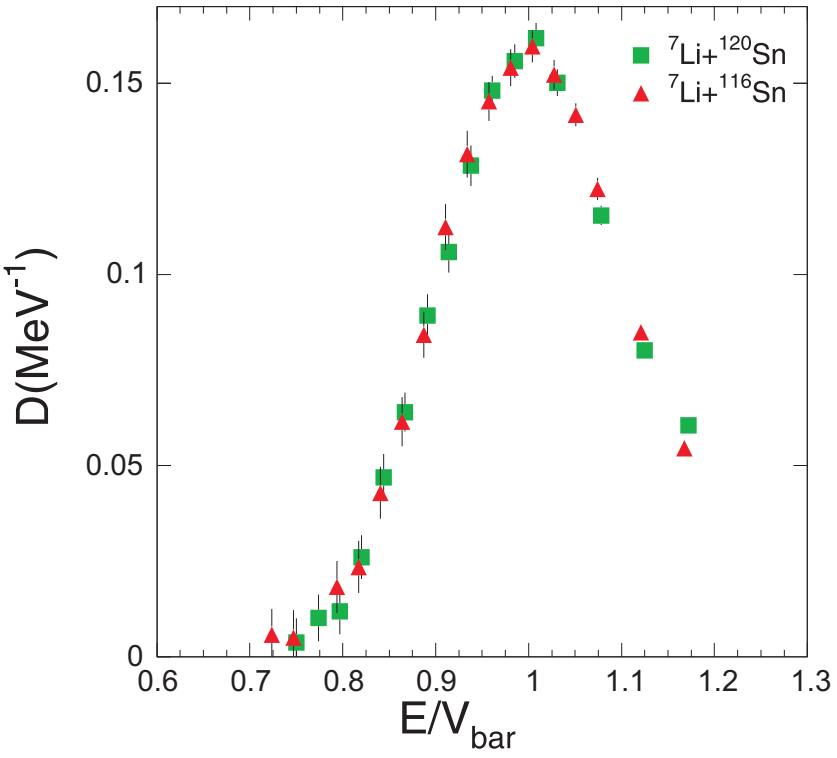

Figure 3.15: *Comparison of barrier distributions for* $^{7}Li + ^{116}$ *Sn and* $^{7}Li + ^{120}$ *Sn, denoted with solid triangles and boxes, respectively.*

Chapter 4

Theoretical Analysis

In the present chapter the theoretical analysis of the experimental excitation functions and barrier distributions is described and discussed. The optical-model analysis for probing the optical potential as a function of energy, was accomplished by using for the real and imaginary part a BDM3Y1 interaction [79]. It was assumed that the interaction has the same radial dependence for the two parts of the optical potential, the real and the imaginary, but with different normalization factors. For the folding procedure, density distributions for the target nuclei were taken from electron scattering data in a conventional two- or three-parameter Fermi model [80]. A phenomenological model according to Bray et al. [81] and Hartree Fock calculations obtained by Trache et al. [82] were adopted for the densities of the projectiles ^{6}Li and ^{7}Li, respectively. The code ECIS [83] was used for calculating, with the above potentials, the differential cross sections at backward angles. It was also used for reanalyzing elastic scattering differential cross-sections of previous measurements. The code FRESCO [84] was used for predicting transfer cross sections and the code ECIS for predicting one barrier penetration fusion cross sections. Finally, Continuum Discretized Coupled Channel (CDCC) calculations are performed by Krzystof Rusek and are presented for a more global view of the reaction mechanisms involved in the present systems under consideration. In this case, the differential cross-sections were obtained by using the code FRESCO for probing couplings to continuum.

4.1 Optical-model Analysis

The starting point in the optical model theoretical analysis is the imaginary potential. As analyzed in chapter 1, the simplest way to reproduce this is by using the linear segment model as proposed by G.R. Satchler [6]. This has the advantage of giving a simple analytic form for the dispersion relation, while it gives results close to more physical, smooth functions for $W(E)$. The real potential is calculated via dispersion relations. Putting the

values of the the real and imaginary potential in ECIS code, it is possible to calculate the ratio of elastic excitation function over Rutherford for that energy. In the case of the ^{7}Li projectile, trials were also performed with an imaginary potential following the linear segment model and a flat real potential not obeying the dispersion relations. In order to systematically probe the optical potential, the analysis of all data was carried out following the same standard procedure which can be described by the following main steps as depicted in figure 4.1:

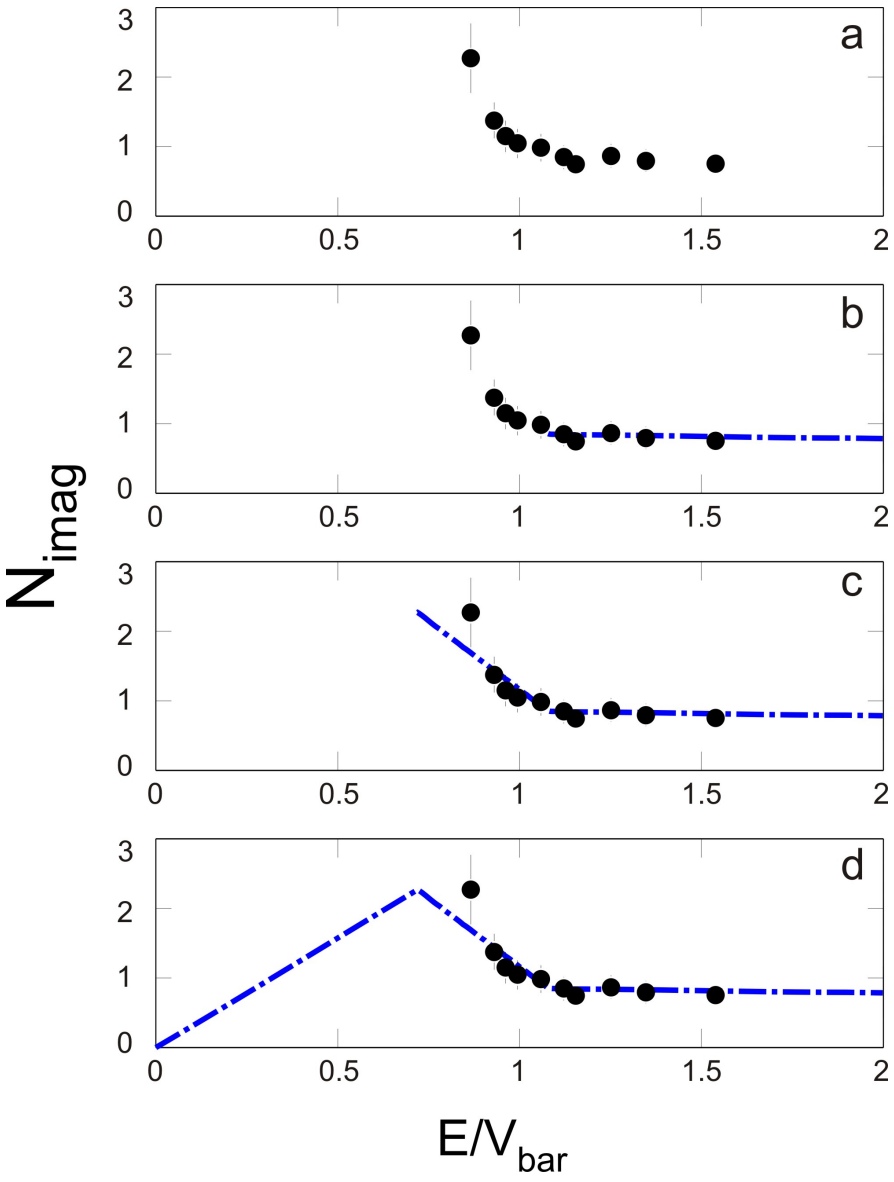

Figure 4.1: *The main steps followed as to energy map the potential.*

1. Draw a straight line, from higher to lower energies, in order to define the imaginary potential above the Coulomb barrier (Appendix F1,

F2). This line should be consistent with previous experimental data extracted via an optical-potential analysis (Fig 4.1 a,b) [87].

2. Define the energy point where a second line should be drawn with positive or negative slope. This second line is drawn with a certain slope and its start point is changed from higher to lower energies (Fig 4.1 b).

3. Define the slope of the second line which is drawn down to very low energies close to zero, changing it from negative slopes (conventional threshold anomaly) to more positive ones (Fig 4.1 c).

4. Iterate between points 2 and 3 till the best reduced χ^2 is obtained between the calculated and experimentally determined barrier distributions.

5. Define the last energy point, where the imaginary potential drops to zero, changing it from higher to lower energies up to a point beyond which the fit is not any more sensitive to potential changes (Fig 4.1 d).

6. (If the final fit is not satisfactory.) Iterate between 1 to 5 changing the height of the first flat line describing the imaginary potential at energies above the Coulomb barrier.

The optical model theoretical analysis is described in detail for the system $^{6,7}Li + ^{58}Ni$, which is used as the main example for demonstrating the sensitivity and usefulness of the technique for probing the potential. All the other systems are treated in the same way with emphasis on a final comparison between the potentials.

4.1.1 Optical model of the system ^{6}Li $+^{58}$ Ni

Elastic scattering angular distribution measurements for the ^{6}Li system have been presented before by Pfeiffer, Speth, Bethge [85] for near-barrier energies (experimental data A, denoted with black boxes in figure 4.2 a,b). Similar measurements have been presented by E.F. Aguilera et al. [25] for sub-barrier energies (experimental data B, denoted with blue boxes in figure 4.2 a,b). The data A were reanalyzed recently by Biswas et al. [22] in a double-folding BDM3Y1 framework as well as with a Woods Saxon potential. The energy dependence obtained for the imaginary part of the optical potential shows a steep increasing trend with decreasing energy at the barrier region. This corresponds to a bump in the real part appearing at $E = 0.8V_{bar}$, obeying a dispersion relation. The data A+B were reanalyzed recently by A. Gomez Camacho et al. [29], with the double-folding Sao Paolo Potential (SPP) interaction. In this case a rather flat energy dependence of the imaginary potential is predicted, which continues well below sub-barrier

energies and finally drops to zero at $E \sim 0.65 V_{bar}$. The rather large errors of the fitting procedure, as expected in this energy region, may also allow a description of the imaginary potential consistent with a small increasing trend as the energy is decreasing. The data A+B were also reanalyzed in the present study in the standard BDM3Y1 framework [79]. The uncertainty in all data points was considered to be 10%. The results for the potential are presented in figure 4.2 (a, b) for the imaginary and real part of the optical potential, respectively, and are denoted with boxes. These results are compatible with those obtained by Gomez Camacho et al. [29], presenting a rather flat behavior and not the trend proposed in [22].

It will be demonstrated now how the backscattering technique will reduce the ambiguity of the energy dependence of the potential as presented above, and further on, how it can provide the means for an accurate determination of the potential to very low sub-barrier energies. The analysis starts with various trial imaginary potentials, shown in fig. 4.2 a, by using as a guide the elastic scattering data existing at the higher energies. The procedure is

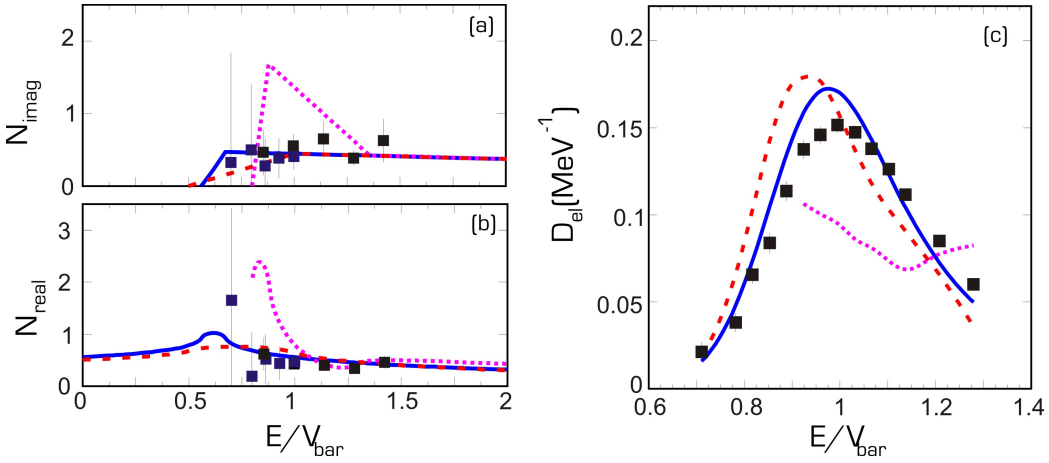

Figure 4.2: *Study of the system $^{6}Li + ^{58}Ni$: a) Trial imaginary potentials. The red dashed line corresponds to potential with a traditional threshold anomaly, the blue solid line with the suggested potential by Camacho et al. and the purple dotted line with the potential suggested by Biswas et al. b) The respective real potentials obtained via dispersive relations. In panels a and b, with boxes are denoted the potentials obtained in the present study from fits to previous angular distribution measurements [85, 25]. c) Barrier distributions corresponding to these potentials.*

commenced by drawing a flat line from the higher-to-lower energies, and a second line describing the drop of the potential to zero at an energy close to the Coulomb barrier (dashed red line). This is the conventional imaginary potential which appears in the threshold anomaly of well-bound nuclei. The analysis is then continued with a similar trial potential, suggested by Gomez Camacho et al. [29] or suggested by the present reanalysis of the previous elastic scattering data (solid blue line), it is described also by a flat line but

which continues to very low sub-barrier energies, dropping to zero at $E = 0.65V_{bar}$. Finally, a third trial potential is shown as suggested by the analysis of Biswas et al. [22], denoted by a dotted purple line (a flat part accompanied by a line of positive slope and then a line with negative slope, dropping to zero at the barrier). The corresponding real parts in all three cases are calculated via dispersion relations [5]. Subsequently adopting such optical potentials, elastic scattering cross-sections are calculated for the backward angles $\theta_{lab} = 160°$ and $170°$, an average cross-section is extracted and used for calculating barrier distributions. The results are presented in fig. 4.2c with the same notation as the potential of fig. 4.2.

It is obvious that the above optical potentials, suggested by the elastic scattering, cannot reproduce the backscattering results of the barrier distribution. Therefore many trials were performed in order to obtain the best energy point at which the imaginary potential starts rising as the energy is decreasing and also for the energy point where it starts dropping to zero. Some trials were also devoted to the height of the flat part of the line describing the imaginary potential at the higher energies. Some of these trials are shown in figures 4.3, 4.4 and 4.5. After several other trials, a best optical potential is adopted as the one for which the predicted barrier distribution shows the best consistency with the measured one. It is described by the solid black line in all figures.

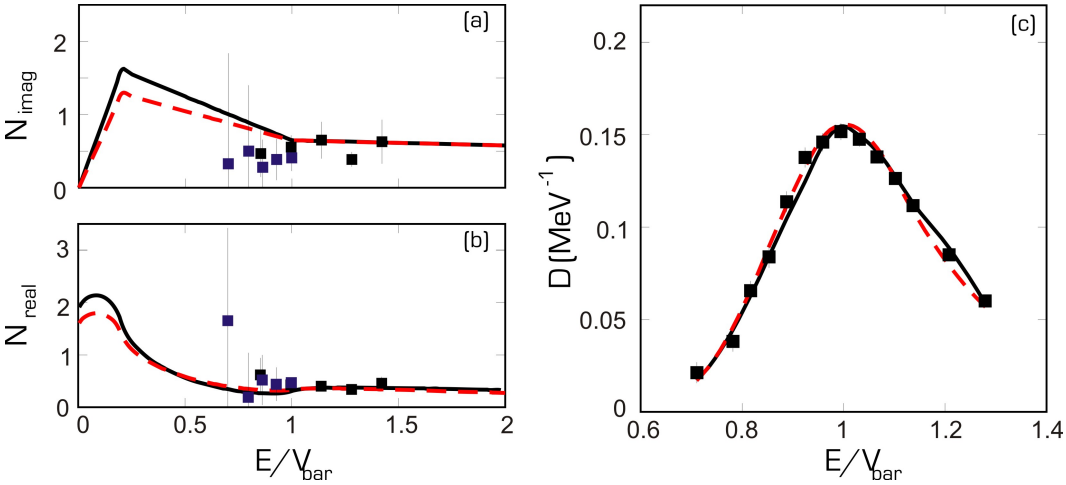

Figure 4.3: *a, b) Same as figure 4.2 but with trial potentials whose imaginary parts have different slopes. The black line corresponds to the best potential. c) Barrier distributions corresponding to these potentials.*

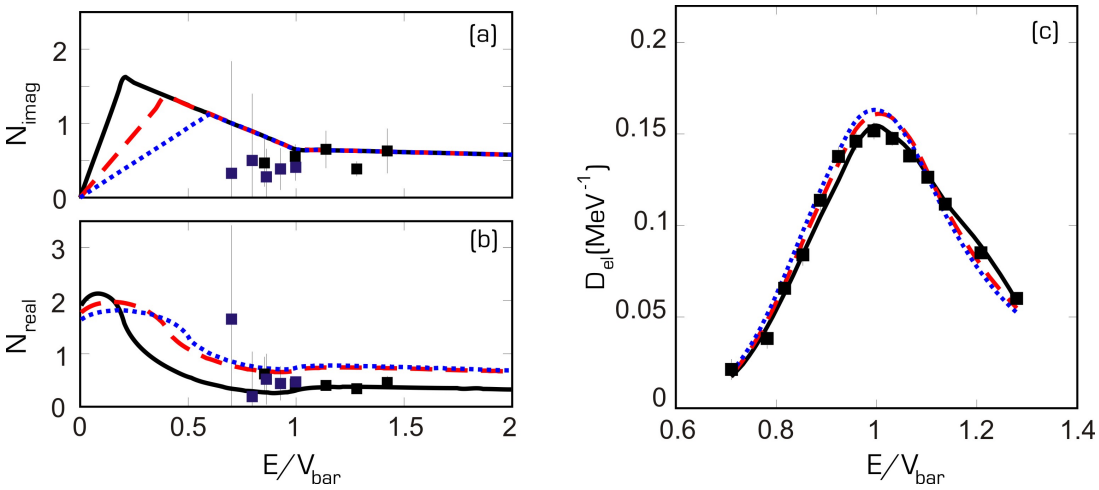

Figure 4.4: *a, b) Same as figure 4.2 but with trial potentials whose imaginary parts have different falling point. The black line corresponds to the best potential. c) Barrier distributions corresponding to these potentials.*

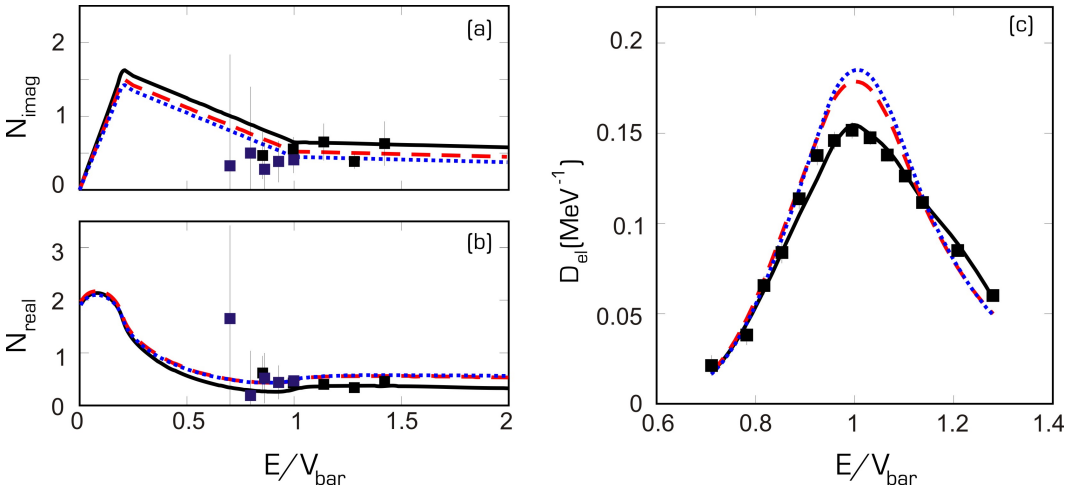

Figure 4.5: *a, b) Same as figure 4.2 but with trial potentials whose imaginary parts have different height in the straight line. The black line corresponds to the best potential. c) Barrier distributions corresponding to these potentials.*

Finally, in fig. 4.6a previous experimental data (data B) are presented of elastic scattering angular distributions at some near barrier energies together with the best fits, obtained in the present reanalysis of these data in our usual BDM3Y1 framework. In the same figure, predicted cross-sections are presented according to the proposed potentials, obtained via the backscattering barrier distribution technique and the agreement is very good.

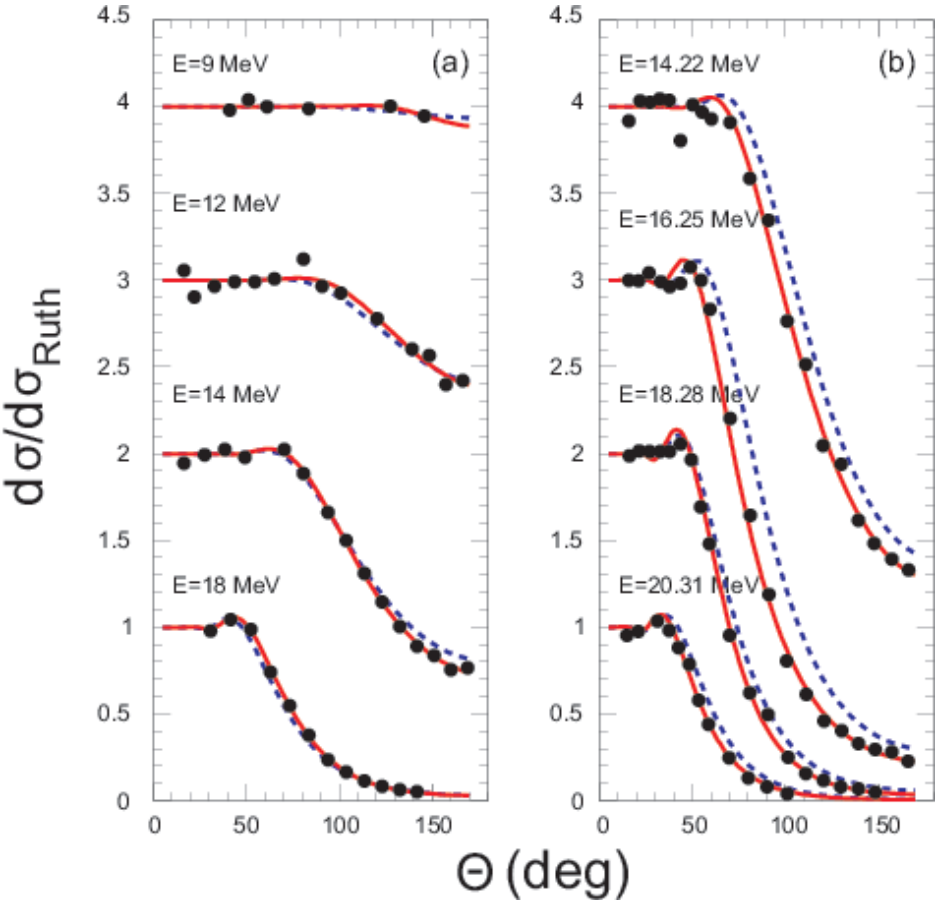

Figure 4.6: *Previous elastic scattering data [25] are compared with best fits into a BDM3Y1 optical-model analysis (solid line, red line) and predictions obtained via optical potentials determined via the backscattering technique (dashed line, blue line) for the systems (a) $^{6}Li +^{58} Ni$ and (b) $^{7}Li +^{58} Ni$.*

4.1.2 Optical model of the system ^{7}Li $+^{58}$ Ni

A similar procedure was carried for the system $^{7}Li +^{58} Ni$. For ease of comparison the same notation of lines was used in these figures. In more detail, it had considered an optical potential with the real part in one case described by a line deduced from the imaginary potential via a dispersion relation and in the second case described simply by a flat line not obeying the dispersion theory. The analysis was started with a few trial imaginary potential which fited few data extracted from the reanalysis of elastic scattering results [85] via our standard BDM3Y1+ECIS procedure, as shown in figure 4.7. The barrier distributions, obtained either with a potential obeying the dispersion relation or with one that does not, were not compatible with the backscattering data.

Subsequently, more trials were performed, reducing substantially the flat part of the line describing the higher energy imaginary potential, while changing gradually the slope of the decreasing low-energy part, as shown in fig-

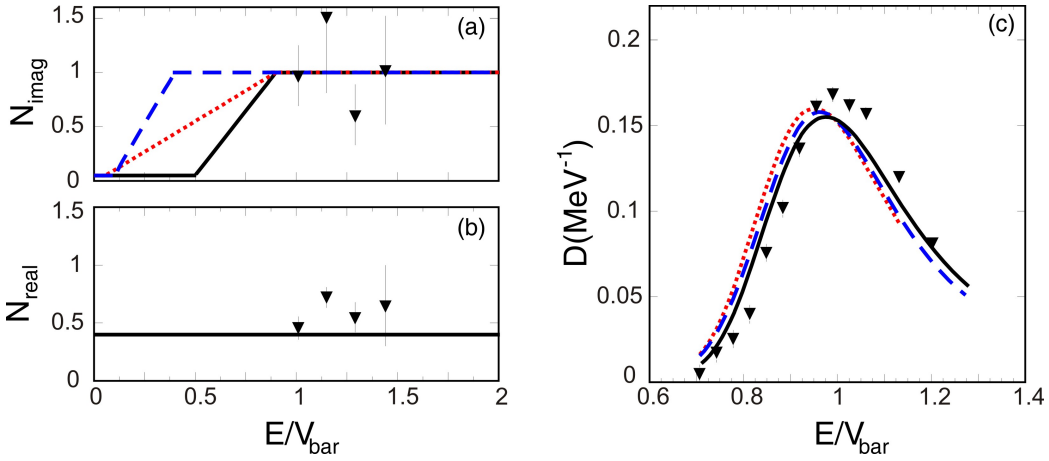

Figure 4.7: *Study of the system $^{7}Li + ^{58}Ni$: a) Trial imaginary potentials which follow the experimental data. b) A flat line was used as the real part of the potential, which does not obey a dispersive relation. In panels a and b, with triangles are denoted the potentials obtained in the present study from fits to previous angular distribution measurements [85]. c) Barrier distributions corresponding to these potentials.*

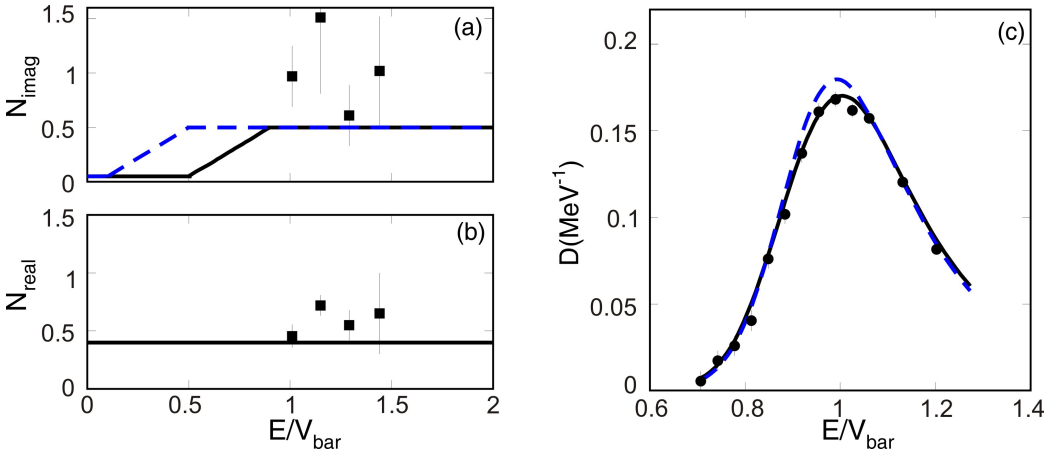

Figure 4.8: *a,b) Same as figure 4.7 but with different trial potentials. Again a flat line was used as the real part of the potential, which does not obey a dispersive relation. The thick solid black line corresponds to the best potential. c) Barrier distributions corresponding to these potentials.*

ure 4.8 and 4.9. The best optical potential obtained gives almost equally good predictions for the barrier distribution data, with and without dispersion, with slightly different reduced χ^2's (with dispersion $\chi^2 = 2.7$, without dispersion$\chi^2 = 1.2$). Note the step in the imaginary potential in all trials, is necessary to absorb flux from the elastic channel.

Finally, in fig. 4.6 b previous experimental data (data B) are presented of elastic scattering angular distributions at some near-barrier energies together with the best fits, obtained in the present reanalysis of these data in our usual

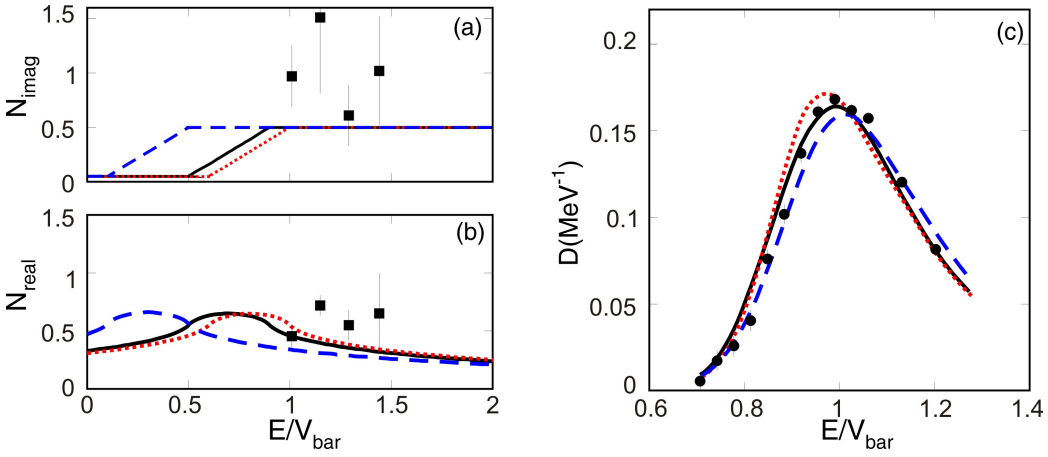

Figure 4.9: *a,b) Same as figure 4.8 but with real part of the potential obeying a dispersive relation. The solid black line corresponds to the best potential. c) Barrier distributions corresponding to these potentials.*

BDM3Y1 framework. In the same figure predicted cross-sections are presented, according to the proposed potentials obtained via the backscattering barrier distribution technique. In this case the agreement at lower energies, between predictions of backscattering and angular distribution data, is adequately good only at the extremes of a 10% error. Despite several trial attempts it was impossible to find a potential describing both sets of data indicating that new angular distribution measurements may be necessary. In principle this disagreement does not exclude problems in the present barrier distribution data. Taking into account that the present data were determined with small errors and that data on other targets do not present similar large inconsistencies, with some caution we give more confidence to the present data.

4.1.3 Optical model of the systems ^{6}Li $+^{116,120}$ Sn

A similar analysis, as in the previous subsections, was applied for the system $^{6}Li + ^{120}Sn$. In figure 4.10 a trial potential is shown, which follows the experimental data. It is obvious that the barrier distribution which was obtained does not follow the backscattering data. For an imaginary potential which reached the higher point of the data, the barrier distribution was even worse.

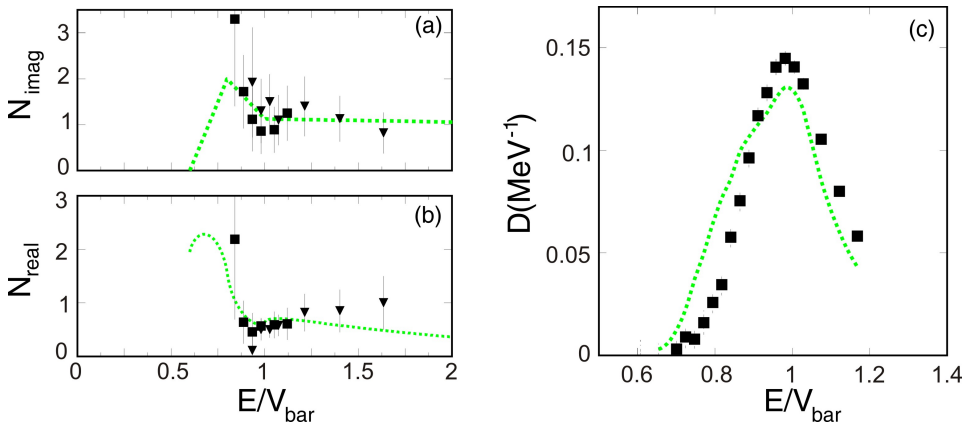

Figure 4.10: *Study of the system $^{6}Li + ^{120}Sn$: a) Trial imaginary potential which follows the experimental data. b) The respectively real potential obtained via dispersive relations. In panels a and b with the solid boxes are denoted the potentials obtained from fits to previous angular distribution measurements for the system $^{6}Li + ^{118}Sn$ [85] and with triangles the potentials for the system $^{6}Li + ^{116}Sn$ [86] c) Barrier distribution corresponding to this potential.*

So more trials were made with different imaginary potentials. In figures 4.11 and 4.12 various other trials are given, for obtaining the optical potentials taking as a reference point the barrier distribution. The best potential is the one with the solid black line.

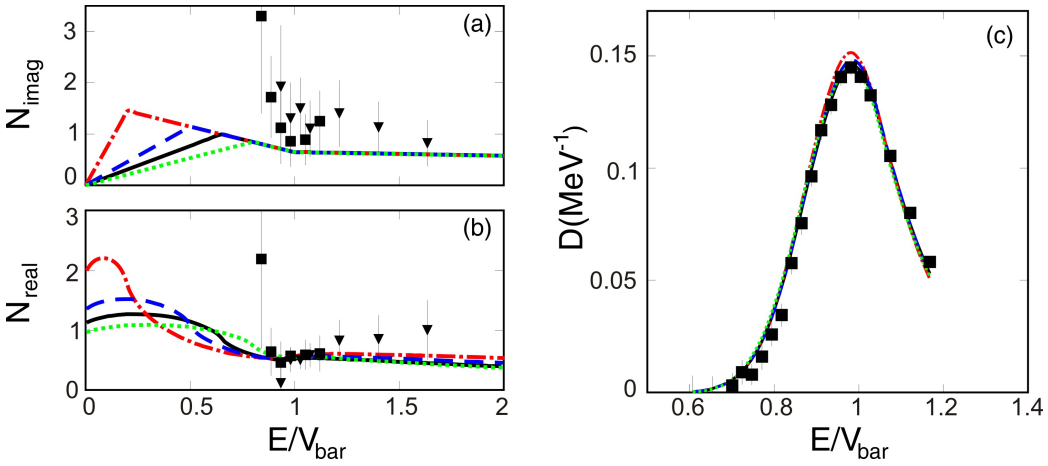

Figure 4.11: *a, b)Same as figure 4.10 but with trial potentials whose imaginary parts have different falling point. The solid black line corresponds to the best potential. c) Barrier distributions for these potentials.*

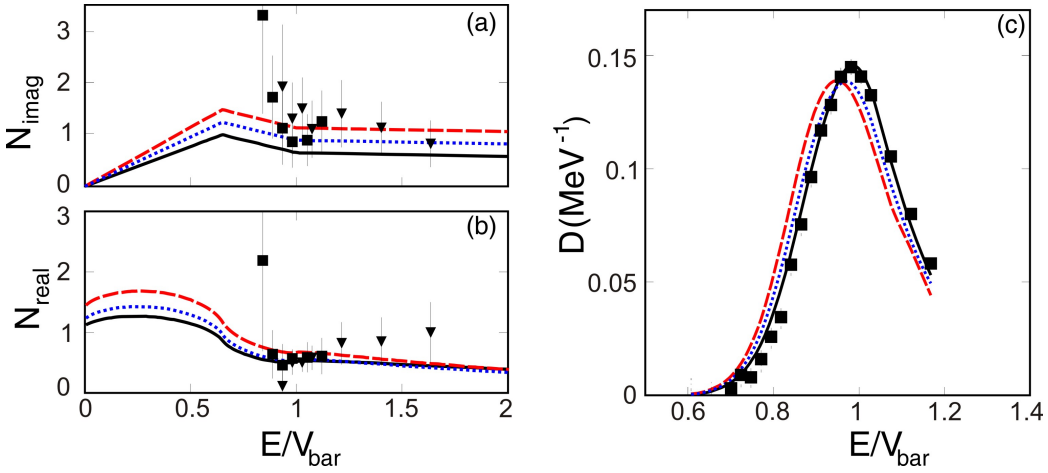

Figure 4.12: *a, b) Same as figure 4.10 but with trial potentials whose imaginary parts have different heights in the flat line. The solid black line corresponds to the best potential. c) Barrier distributions for these potentials.*

4.1.4 Optical model of the systems ^{7}Li $+^{116,120}$ Sn

The various trials for obtaining the optical potentials for the system $^{7}Li + ^{120}Sn$, taking as a reference point the barrier distribution, are given in figs. 4.13 and 4.14 assuming a dispersion relation or a flat line respectively.

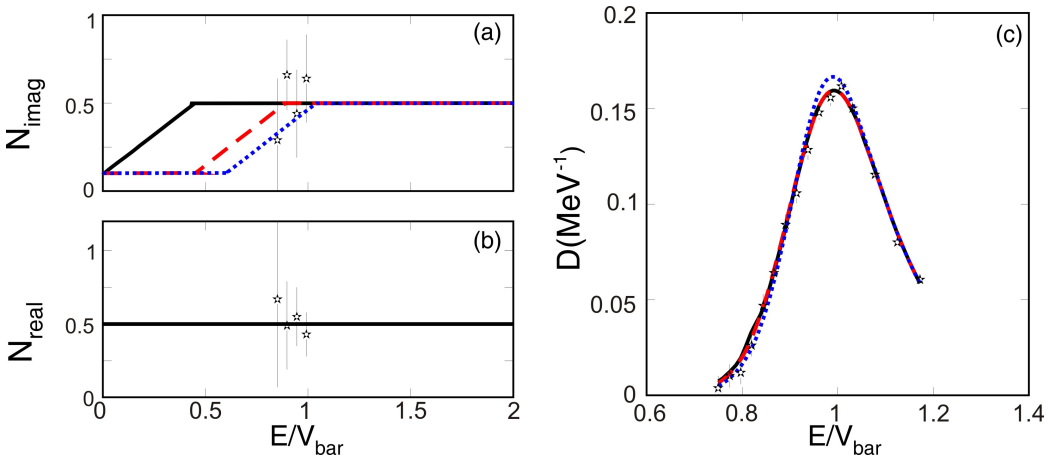

Figure 4.13: *Study of the system $^{7}Li + ^{120}Sn$: a) Trial imaginary potentials b) A flat line was used as the real part of the potential, which does not obey the dispersive relation. In panels a and b, with stars are denoted the potentials obtained in the present study from fits to previous angular distribution measurements [85]. The solid black line corresponds to the best potential. c) Barrier distributions corresponding to these potentials.*

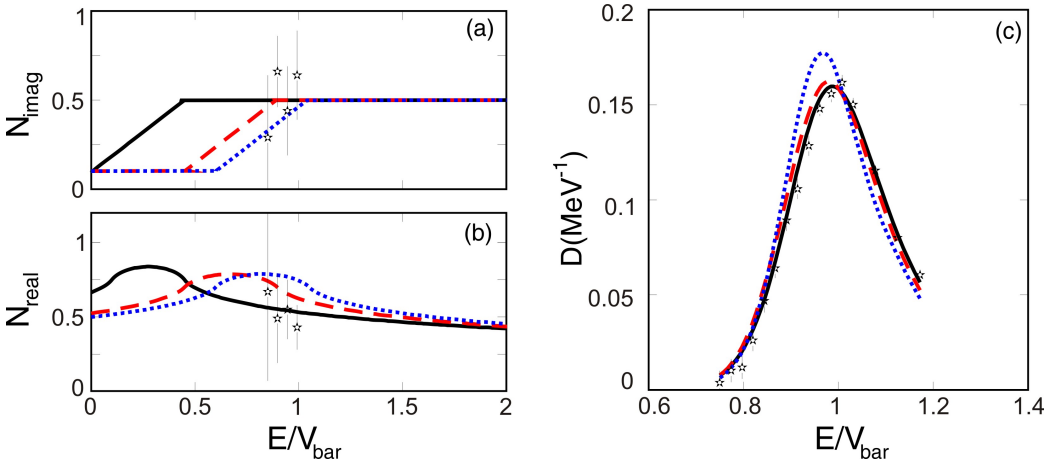

Figure 4.14: *a) Some as figure 4.13, but with real part of the potential obeying the dispersion relation. c) Barrier distributions corresponding to these potentials.*

4.1.5 Optical model of the systems ^{6}Li $+^{208}$ Pb

A similar analysis, as in the previous subsections, was applied for the system $^{6}Li + ^{208}Pb$. The first trial was made with an imaginary potential which passed exactly through the data, and especially from the higher point, but this attempt was not satisfactory since it gave very bad fit to the barrier distribution. So more trials were made with imaginary potentials which had different slope, different starting and falling point and different height at the straight part. The various trials for obtaining the optical potentials taking as a reference point the barrier distribution, are given in figs. 4.15 - 4.18.

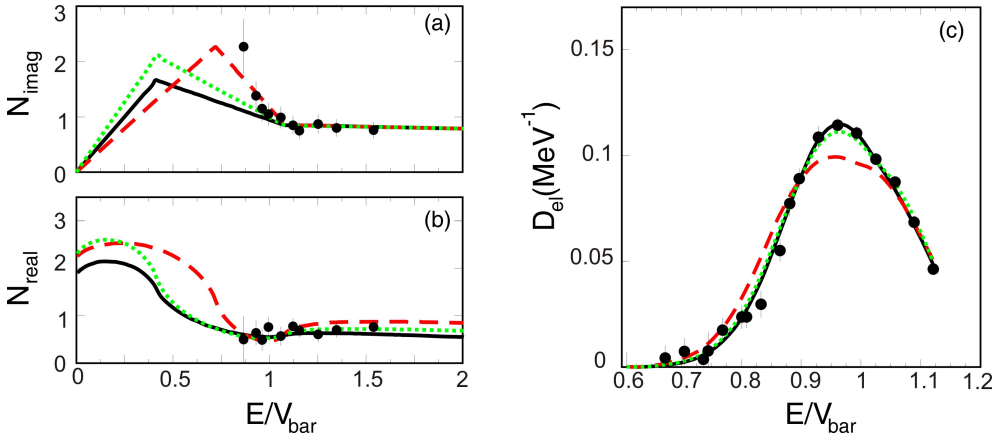

Figure 4.15: *Study of the system $^{6}Li + ^{208}Pb$: a) Trial imaginary potentials with different slopes. b) The real potentials is calculated via dispersive relations. The solid black line corresponds to the best potential. In panels b and c, with circles are denoted the potentials obtained in the present study from fits to previous angular distribution measurements [87] .c) Barrier distributions for these potentials.*

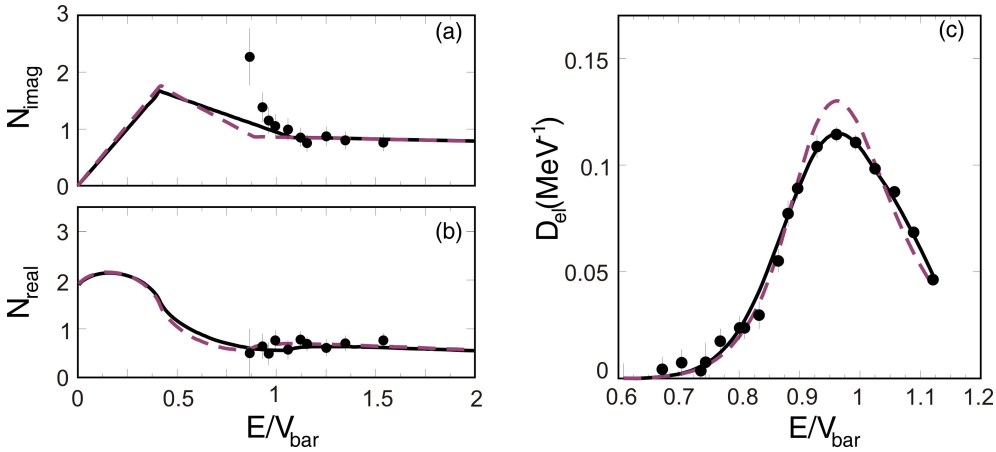

Figure 4.16: *a,b) Same as figure 4.15 but with trial potentials whose imaginary parts have different starting point. The solid black line corresponds to the best potential. c) Barrier distributions for these potentials.*

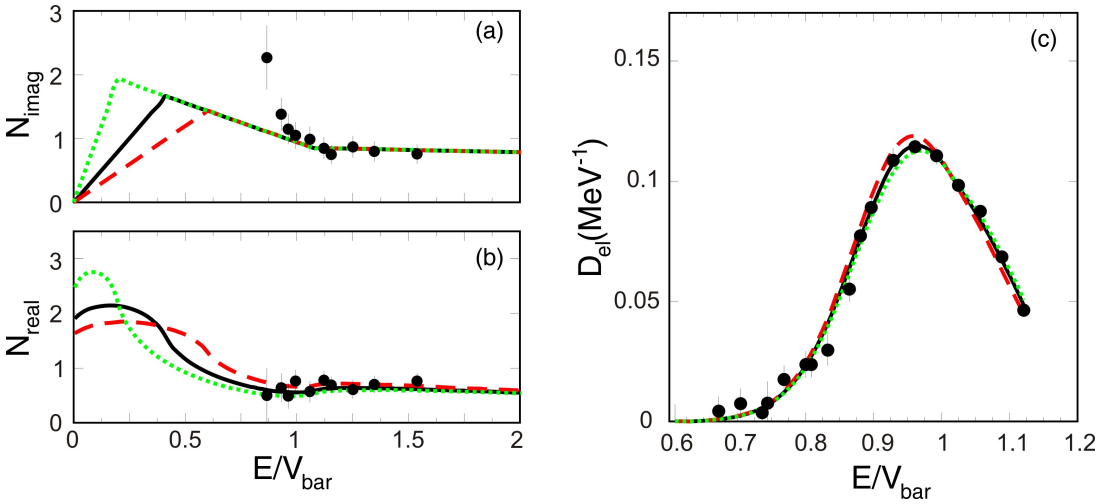

Figure 4.17: *a,b) Same as figure 4.15 but with trial potentials whose imaginary parts have different falling point. The solid black line corresponds to the best potential. c) Barrier distributions for these potentials.*

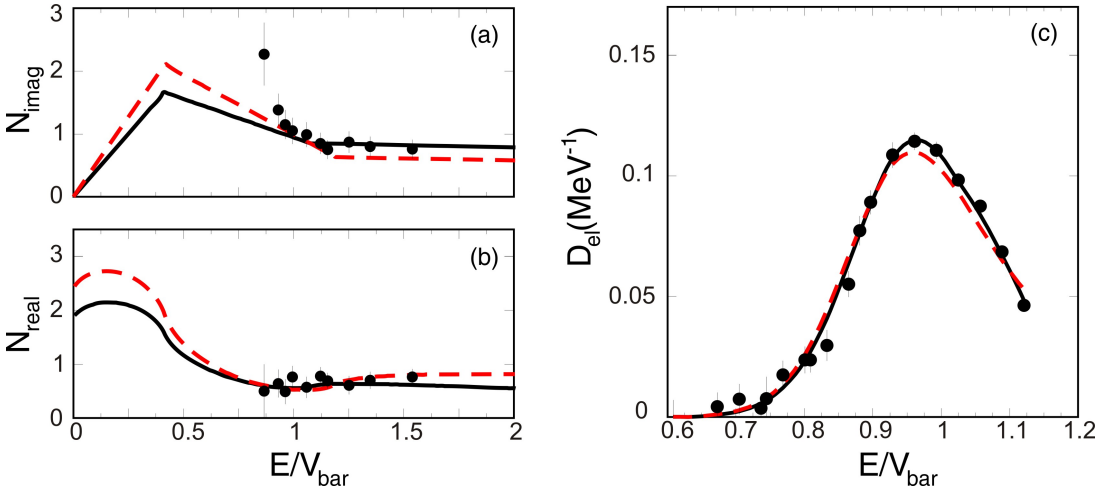

Figure 4.18: *a,b) Same as figure 4.15 but with trial potentials whose imaginary parts have different height of the flat line. The solid black line corresponds to the best potential. c) Barrier distributions for these potentials.*

4.1.6 Optical model of the systems ^{7}Li $+^{208}$ Pb

The various trials for obtaining the optical potentials taking as a reference point the barrier distribution, are given in figs. 4.19 - 4.24.

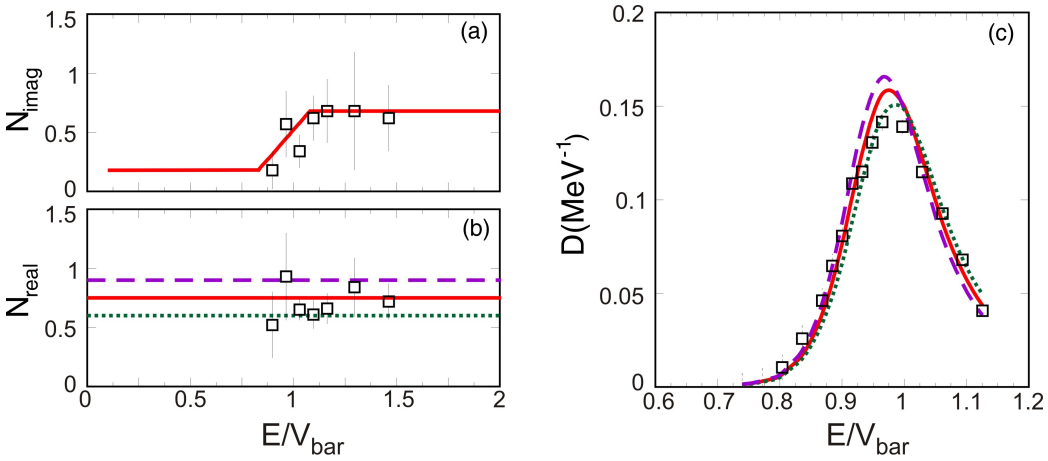

Figure 4.19: *Study of the system $^{7}Li+^{208}Pb$: a) Trial imaginary potentials which follow the experimental data. b) Flat lines were used as the real part of the potential, which do not obey the dispersion relation. In panels b and c, with boxes are denoted the potentials obtained in the present study from fits to previous angular distribution measurements [87]. c) Barrier distributions for these potentials.*

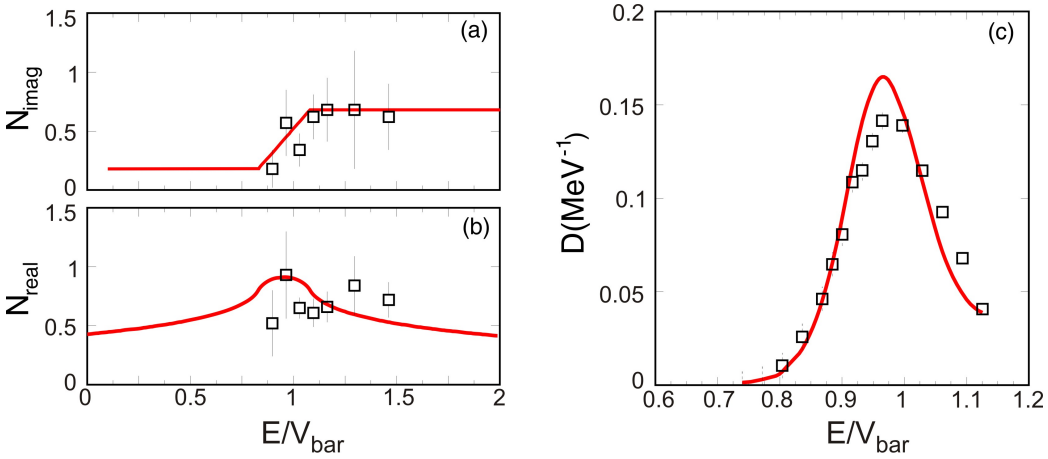

Figure 4.20: *a,b) Same as figure 4.19 but with real part of the potential obeying the dispersion relation. c) Barrier distributions for these potentials.*

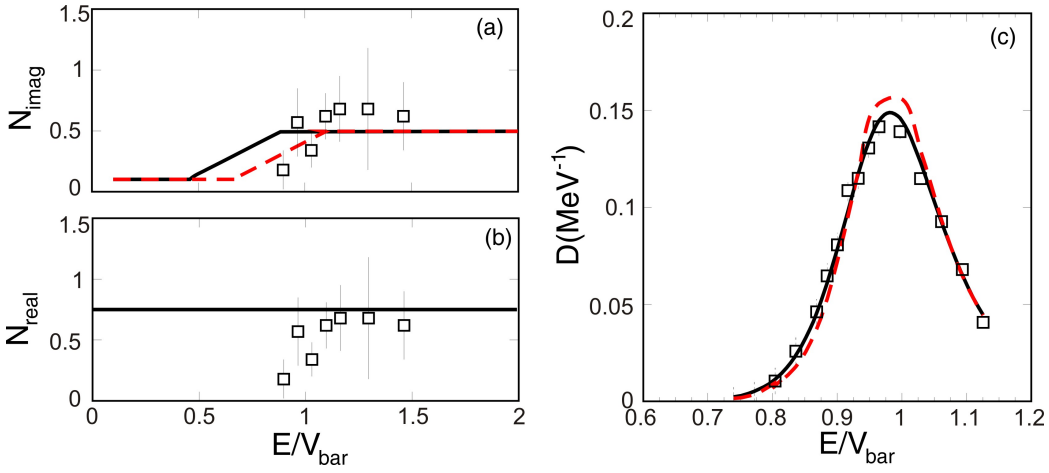

Figure 4.21: *a,b) Same as figure 4.19 but with further trial potential whose imaginary parts have different falling point and their real part does not obey the dispersion relation. The solid black line corresponds to the best potential. c) Barrier distributions for these potentials.*

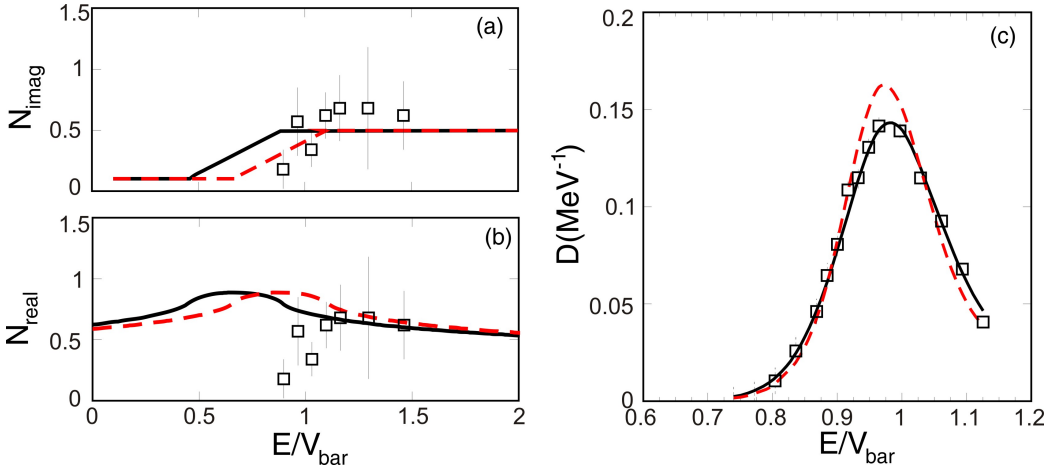

Figure 4.22: *a,b) Same as figure 4.19 but with further trial potential whose imaginary parts have different falling point and their real obeying the dispersion relation. The solid black line corresponds to the best potential. c) Barrier distributions for these potentials.*

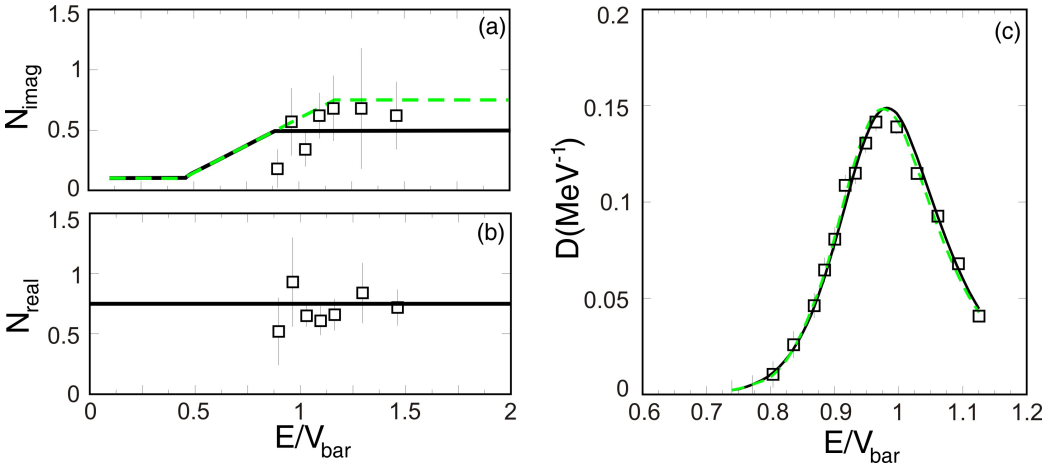

Figure 4.23: *a,b) Same as figure 4.19 but with further trial potential whose imaginary parts have different height of the flat line and their real part does not obey the dispersion relation. The solid black line corresponds to the best potential. c) Barrier distributions for these potentials.*

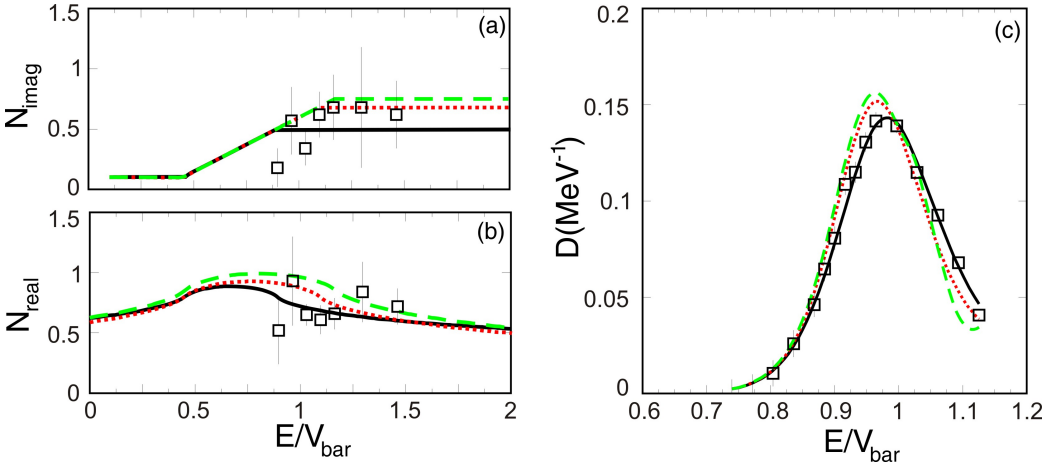

Figure 4.24: *a,b) Same as figure 4.19 but with further trial potential whose imaginary parts have different height of the flat line and their real obeying the dispersion relation. The solid black line corresponds to the best potential. c) Barrier distributions for these potentials.*

4.1.7 Optical model of the system ^{6}Li $+^{28}$ Si

The various trials for obtaining the optical potentials taking as a reference point the barrier distribution, are given in figs. 4.25 and 4.26.

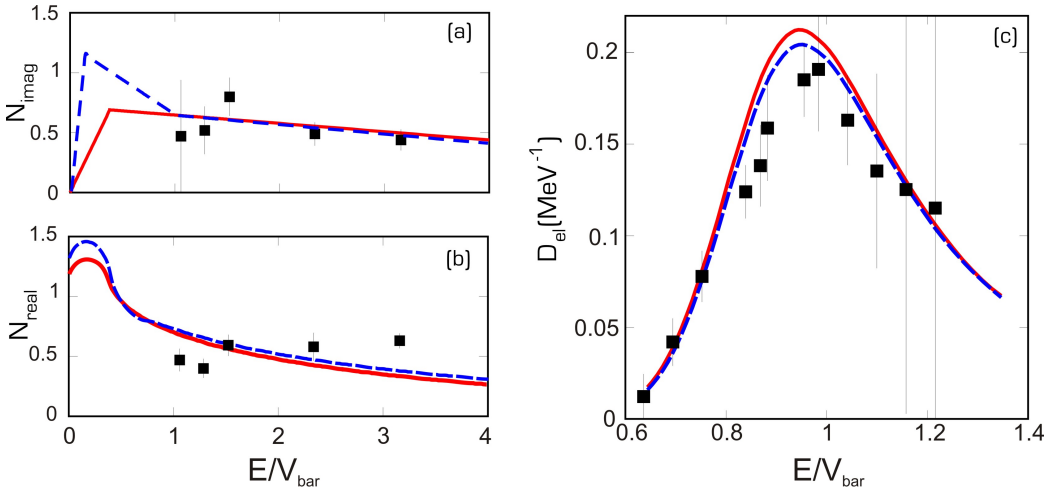

Figure 4.25: *Study of the system $^{6}Li +^{28} Si$: a) Trial imaginary potentials with a small peak at very low energies. b) The real potential is calculated via dispersive relations. c) Barrier distributions for these potentials.*

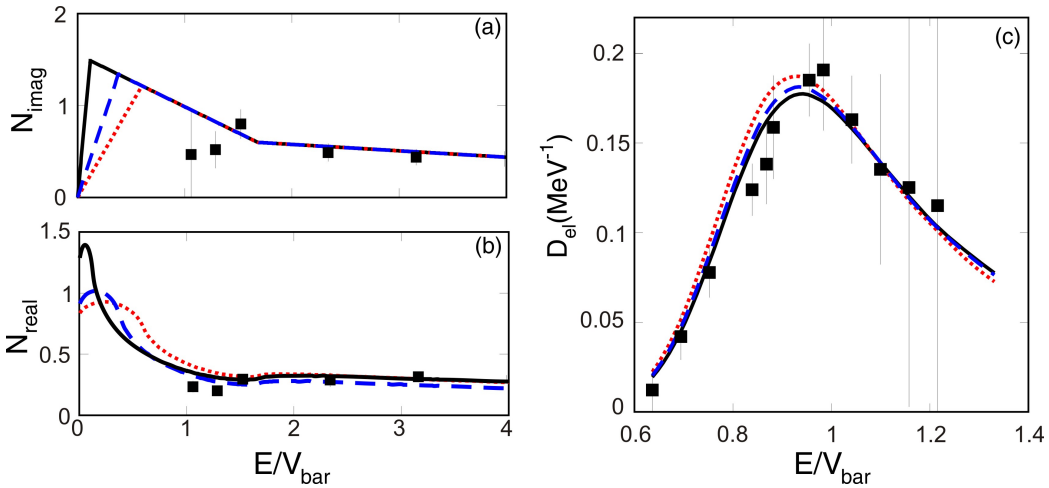

Figure 4.26: *a,b) Same as figure 4.25 but with further trial potential whose imaginary parts have different final point. The solid black line corresponds to the best potential. c) Barrier distributions for these potentials.*

4.1.8 Optical model of the systems ^{7}Li $+^{28}$ Si

The various trials for obtaining the optical potentials taking as a reference point the barrier distribution, are given in figs. 4.27, 4.28 and 4.29.

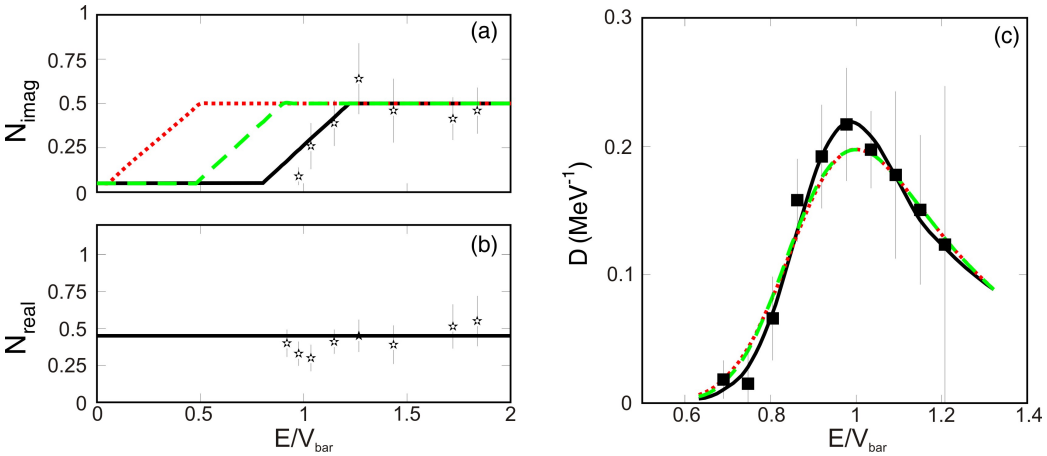

Figure 4.27: *Study of the system $^{7}Li +^{28} Si$: a) Trial imaginary potentials with different dropping point. b) A flat line was used as the real part of the potential, which does not obey the dispersion relation. The black line corresponds to the best potential. c) Barrier distributions for these potentials.*

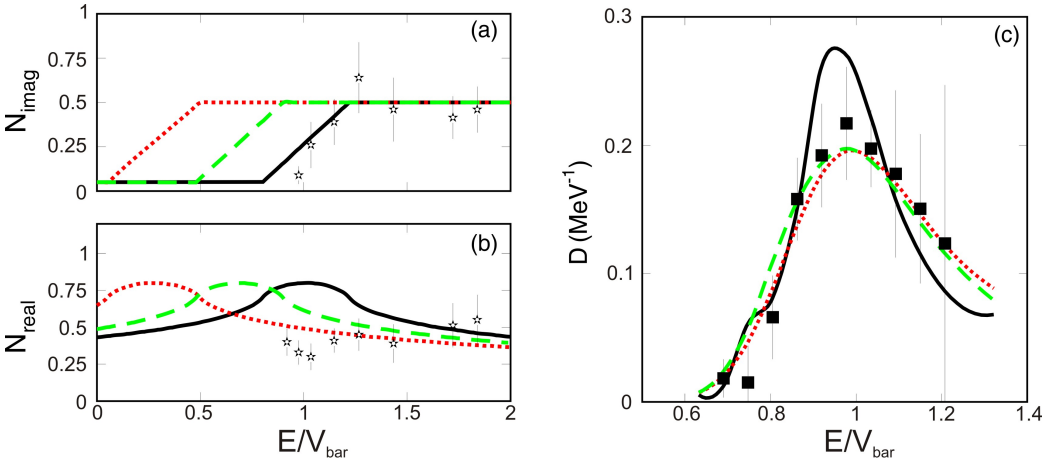

Figure 4.28: *a,b) Same as figure 4.27 but with real part of the potential obeying the dispersive relation. c) Barrier distributions for these potentials.*

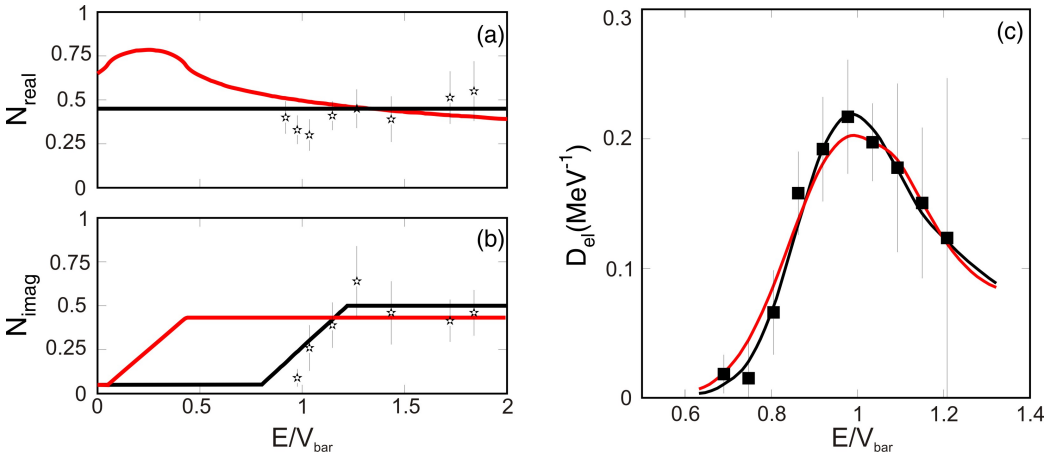

Figure 4.29: *a,b)Same as figure 4.27 but the black line represents the best potential which does not obey dispersive relation while the red line the best potential which obeys the dispersive relation. c) Barrier distributions for these potentials.*

As it can be seen from the analysis we made, this new method is particularly sensitive to the identification of the optical potential. The reason is that the barrier distribution is calculated by the derivative of differential elastic scattering cross sections, so even a small change in the potential has a substantial effect on the barrier distribution.

4.2 Fusion barriers

Fusion barriers extracted from the barrier distributions are shown in tables 4.1 and 4.2, and are compared with theoretical values extracted from phenomenological parameterizations [77]. Other details of the barrier distributions such as the widths and heights are also included in the same tables.

Table 4.1: *Details of barrier distributions for ^{6}Li on various targets. The obtained fusion barriers, $V_{bar}^{meas.}$, are compared with calculated values $V_{bar}^{calc.}$, according to Broglia [77].*

Target	$V_{bar}^{meas.}(MeV)$	$V_{bar}^{calc.}(MeV)$	Width (MeV)	Height (MeV)
^{28}Si	8.5	8.5	3.8	0.20
^{58}Ni	14.0	14.1	5.5	0.15
^{120}Sn	20.9	21.4	6.0	0.15
^{208}Pb	30.0	31.2	7.5	0.11

From the systematics of the barrier distributions we can draw the following conclusions:
The measured barriers agree very well with values calculated via the Broglia parameterizations [77]. For the lighter targets the agreement is excellent.

Table 4.2: *Details of barrier distributions for ^{7}Li on various targets. The obtained fusion barriers, $V_{bar}^{meas.}$, are compared with calculated values $V_{bar}^{calc.}$, according to Broglia [77].*

Target	$V_{bar}^{meas.}(MeV)$	$V_{bar}^{calc.}(MeV)$	Width (MeV)	Height (MeV)
^{28}Si	8.5	8.7	3.3	0.22
^{58}Ni	14.0	14.1	4.8	0.17
^{120}Sn	21.5	21.3	5.3	0.16
^{208}Pb	30.3	31.1	5.6	0.14

The widths of the barrier distributions are larger for the heavier targets, indicating stronger quantal effects, generated by couplings to various reaction channels. For ^{6}Li this is reflected in the increasing trend of the imaginary part of the optical potential (line with a positive slope). The heavier the target the larger the slope. On the other hand the energy point where the imaginary potential drops to zero is located at much lower energies for the lighter targets than for the heavier ones. Comparing the barrier widths of ^{6}Li and ^{7}Li we see that the widths are larger for the first projectile. This fact is also reflected in the imaginary potential which rises at sub-barrier energies for ^{6}Li but is flat for ^{7}Li. In both cases the widths are much larger than those observed for well-bound projectiles, in accordance with the proposed potentials for weakly bound ones, where the imaginary part persists to very low energies below the barrier. The heights of the barrier distributions are systematically larger for the lower mass targets, possibly indicating a stronger surface penetrability for the heavier ones.

4.3 Comparison of potentials

After completing the study of all the systems, four with ^{6}Li and four with ^{7}Li, in figs. 4.30 and 4.31 the optical potentials obtained via the backscattering technique are compared.

The following conclusions can be drawn:

- For ^{6}Li, the imaginary potential presents an increasing trend from higher to lower energies. This rising part has the largest slope for the heavier targets and the smallest slope for the lighter ones. Qualitatively, this may be interpreted to be connected with the breakup channel which is expected to be larger for the heavier targets (larger Z) and smaller for the lighter ones (smaller Z) without excluding transfer contributions. Another interesting point is that the energy where the imaginary potential drops to zero is not located at the barrier but at

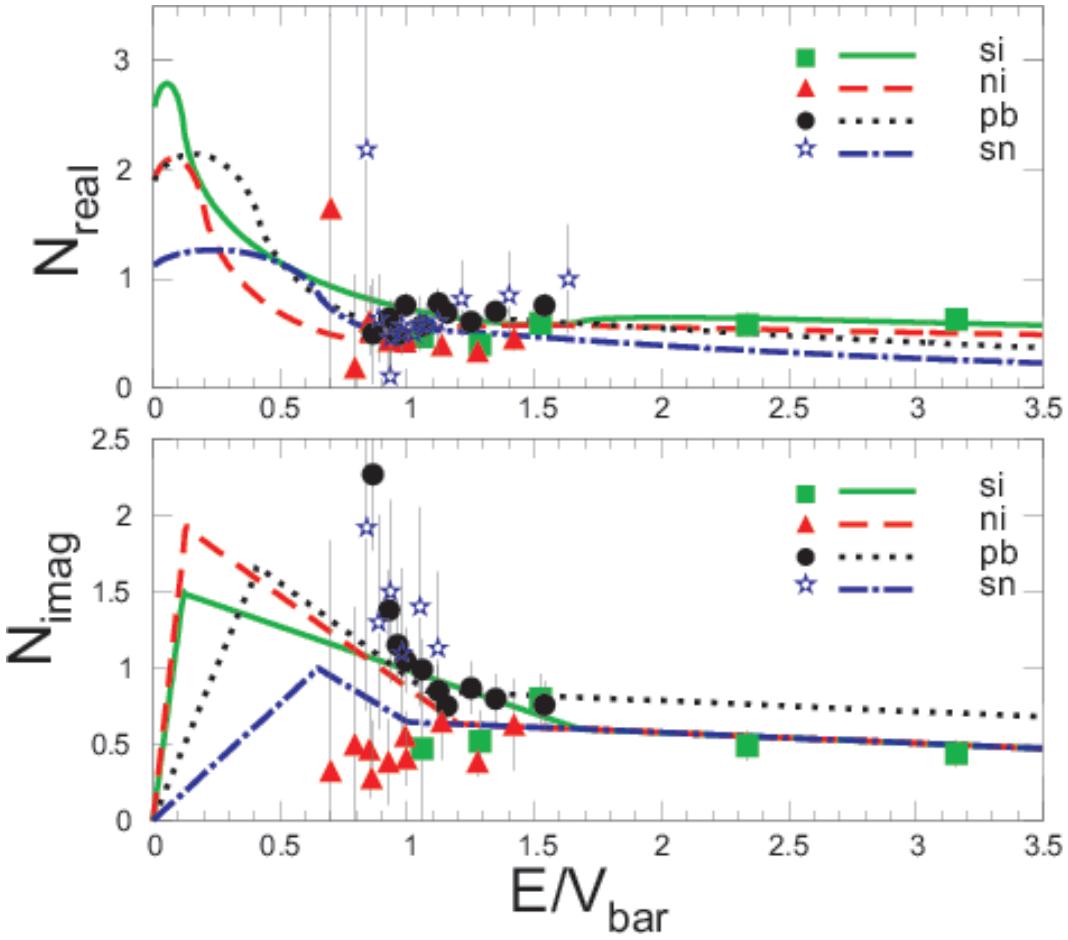

Figure 4.30: *Energy dependence of the optical potentials extracted from the present barrier distribution analysis of ^6Li on silicon, nickel, tin and lead targets. Results obtained from a conventional reanalysis of elastic scattering distributions on various energies previously measured are compared with them. It should be mentioned that symbols and lines of the same color refer to the same colliding system.*

sub-barrier energies, in contrast with the behavior of well-bound nuclei. It should be underlined however that the low energy where the imaginary potential drops to zero for the nickel and silicon targets near $E/V_{bar} \sim 0.2$ raises some questions about the validity of the dispersion relation. It is hardly credible that at this energy such an enormous real dynamical polarization potential almost two times the bare one can be generated. Also it is difficult to think of a physical process which generates such large amounts of absorption.

- For the ^7Li case, a possible break down of the dispersion relation was even more intensified. The problem which has arisen was that the backscattering barrier distributions were well predicted by a potential (polarization potential) obeying the dispersion relation but also by one that does not, with similar χ^2 for the two solutions, although the small-

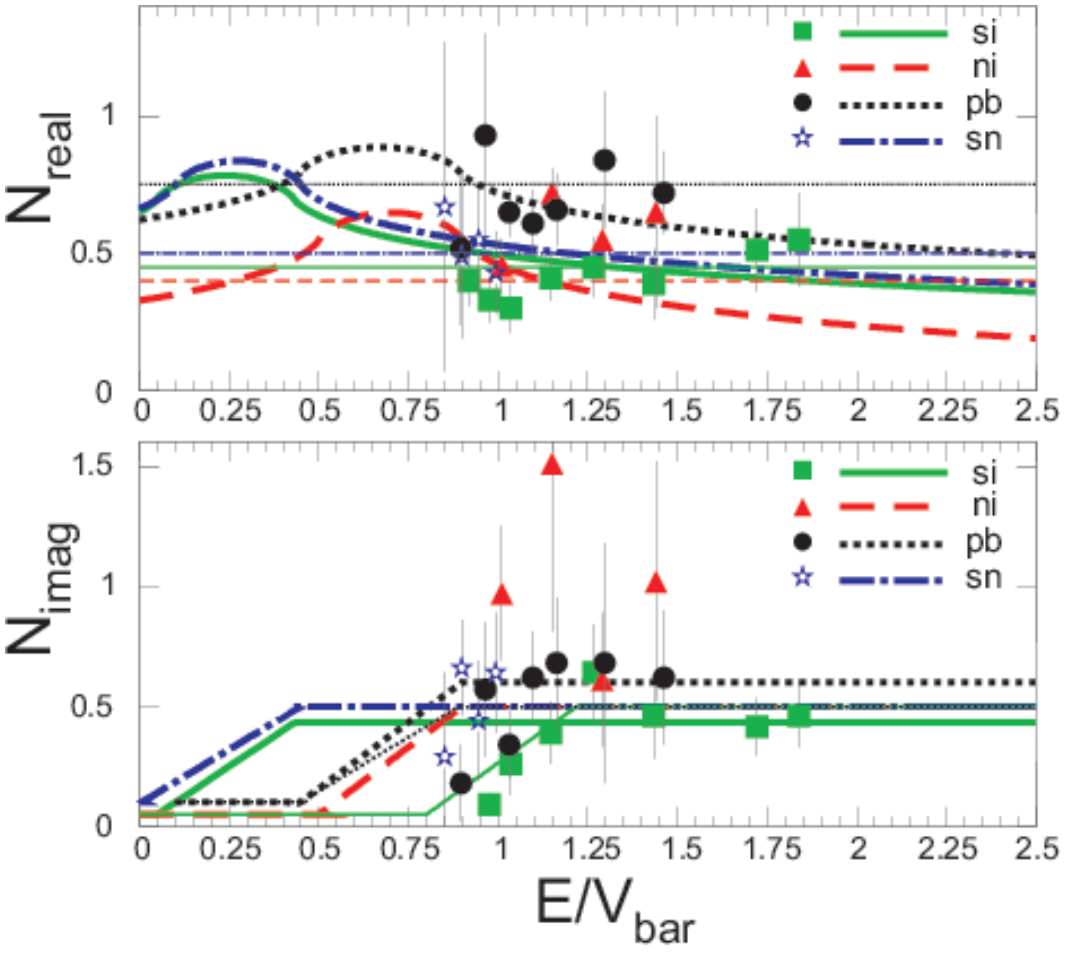

Figure 4.31: *Energy dependence of the optical potentials extracted from the present barrier distribution analysis of ^7Li on silicon, nickel, tin and lead targets. Thin lines represent best potentials where the dispersion relation does not hold. Results obtained from a conventional reanalysis of elastic scattering distributions on various energies previously measured are compared with them. It should be mentioned that symbols and lines of the same color refer to the same colliding system.*

est χ^2 distribution always occurs for the second scenario. If we take into account the case where a dispersion relation holds, then the imaginary potential can be described by a flat line which progresses to very low energies, with a drop to zero between $E/V_{bar} \sim 0.5$ to 0.9.

- If we finally assume that the dispersion relation does not hold then the potential starts dropping to zero between $E/V_{bar} \sim 0.8$ to 1.2 and then continues with a flat step to very low sub-barrier energies. Transfer measurements may be necessary to indicate the correct energy point where the imaginary potential drops to zero and therefore to decide between the two scenarios. In either case the optical potential behavior obtained for the ^7Li projectile contrasts with the trend for ^6Li, where

we observe a rising behavior towards the lower energies. On the other hand, for both weakly bound projectiles the common point is a loss of flux from the elastic channel persisting to very low energies. This is reflected in the imaginary potential which continues to very low sub-barrier energies either with an increasing trend towards lower energies in the case of ^6Li, or with a flat line or/and a small step potential in the case of ^7Li. As was also noticed in the ^6Li case, the proposed potentials do not follow any systematics due to the different reaction mechanisms involved and are unique for each target. This finding is in accordance with the results on polarization potentials studied by Lubian et al. [6]. The authors claim that the net result of polarization potentials describing transfer and breakup may vary from system to system depending on the charge of the target and consequently on the relative strength of the Coulomb and nuclear potentials. Unfortunately this fact prohibits a systematic description of the potential as a function of mass and energy for weakly bound nuclei.

4.4 Prediction of reaction channels

In this section, some examples of one neutron transfer Distorted-Wave Born Approximation (DWBA) calculations are presented, performed with the code FRESCO. Also, fusion calculations are presented, performed with the code ECIS by adopting the potentials determined in the previous section. The examples concern the system $^6Li + ^{28}Si$ for transfer and $^{6,7}Li + \ ^{28}Si$ for fusion.

4.4.1 Transfer

For the system $^6Li + ^{28}Si$ the calculations are performed for two energies, $9MeV$ and $15MeV$ and for two different potentials, the best potential (which was found from the optical model analysis) and a conventional one, which describes well bound systems. The experimental angular distributions were taken from [88]. The results of the calculations for the two incident energies are presented in Figure 4.32.

As it is expected, variations of calculations with the best and the conventional potential are observed at the lower energies and larger angles. As to deduce concrete conclusions, data at lower energies and in a wide angular region are requested.

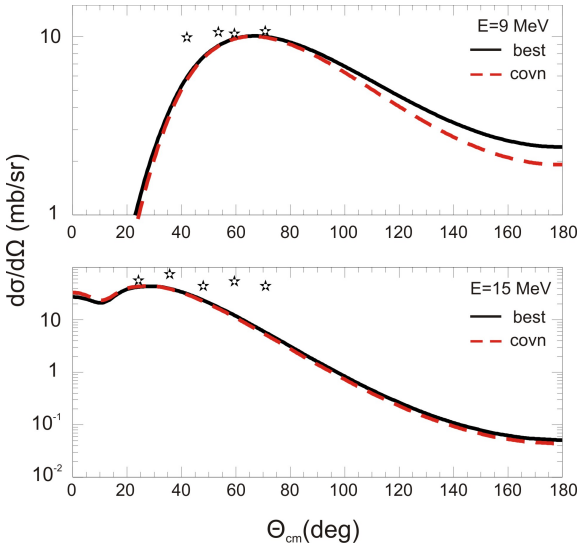

Figure 4.32: *1-n transfer DWBA calculations are compared with experimental results for the system* $^{6}Li + {}^{28}Si$*. For both energies the DWBA calculations were multiplied by a factor of 4.*

4.4.2 Fusion

To complete the analysis, previously measured excitation functions of fusion cross sections are presented in Figure 4.33 for the system $^{6,7}Li + {}^{28}Si$ and are compared with our one barrier penetration model calculations. The above calculations include the best potential (black lines) and a potential having a different trend. They were performed with the code ECIS by using as real part the entrance potential taken from the backscattering study while as imaginary part a very deep potential to absorb all the flux.

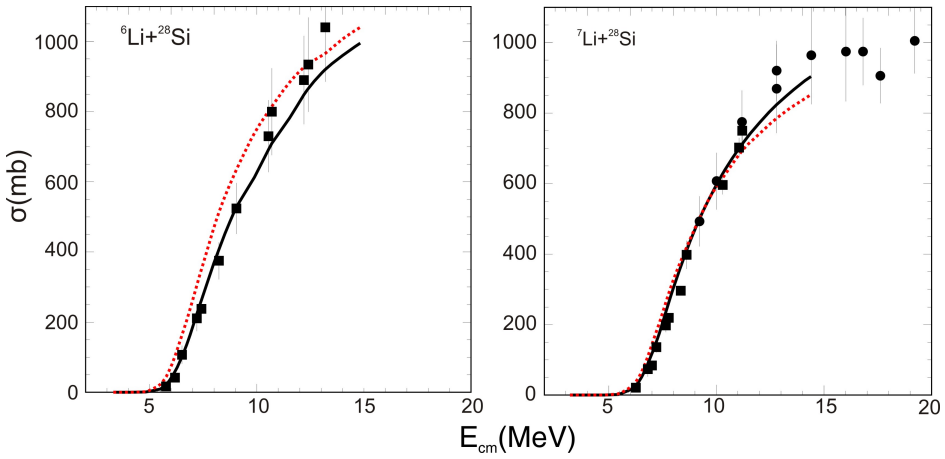

Figure 4.33: *Fusion cross section as a function of energy for the systems (a)* $^{6}Li + {}^{28}Si$ *and (b)* $^{7}Li + {}^{28}Si$*. The black solid line corresponds to the calculation adopting the "best" potential while the red line with corresponds to the calculation with a conventional potential.*

For ^6Li, it is obvious that the calculation with the best potential follows better the experimental data but in large energies is not possible to have safe conclusions because the data are between the calculations. For ^7Li, at the lower energies there is no particular distinction as both calculations follow the data. However, at large energies it is obvious that our calculations describe adequately well the data. The main conclusion is that adopting an exact optical potential as a function of energy we can predict fusion cross sections without the need of CC (Coupled Channels) calculations.

4.5 The reaction mechanism - CDCC calculations

For the completeness of this work, Continuum Discretized Coupled Channels calculations (CDCC calculations) are presented in this section for all the systems. The calculations were performed by Professor K. Rusek. It was assumed that the nucleus ^6Li (^7Li) has a two-body $\alpha + d$ ($\alpha + t$) cluster structure. Couplings between resonant and non-resonant cluster states corresponding to $\alpha - d$ ($\alpha - t$) relative orbital angular momentum $L = 0, 1, 2$ ($L = 0, 1, 3$) were included. For ^7Li excitation of the first-excited-state and ground-state reorientation were taken into account. The continuum above the $^6Li \rightarrow \alpha + d$ ($^7Li \rightarrow \alpha + t$) breakup threshold was discretized into momentum bins. The width of most of the bins was set to $k = 0.26fm^{-1}$ for ^6Li and to $k = 0.25fm^{-1}$ for ^7Li. In the presence of resonant states the binning schemes were suitably modified in order to avoid double counting. All the diagonal and coupling potentials were generated from empirical α+target, d+target and t+target optical model potentials derived from elastic scattering experiments. Since in the backscattering measurements of ^7Li on the silicon, nickel and tin targets, the inelastic part was not resolved from the elastic part, the calculations for ^7Li represent the quasi-elastic scattering (elastic + excitation of ^7Li to its first excited state). The backscattering results are presented in figures 4.34-4.37 and are compared with the CDCC calculations. It is seen that for all cases coupling to the continuum improves the description of the barrier distributions. The effect for the ^6Li cases is very strong, shifting the barrier to higher energies and reducing the barrier distribution height. For the ^7Li cases the effect is much smaller. With no obvious reason a disagreement between the calculation and the data is noted only for $^7Li + ^{120}Sn$. A full CRC calculation taking into account the effect of transfer is beyond the scope of the present work but it may give a solution to the problem. However the main conclusion of this study is that breakup is a dominant contributor to the coupling mechanism at near and sub-barrier energies.

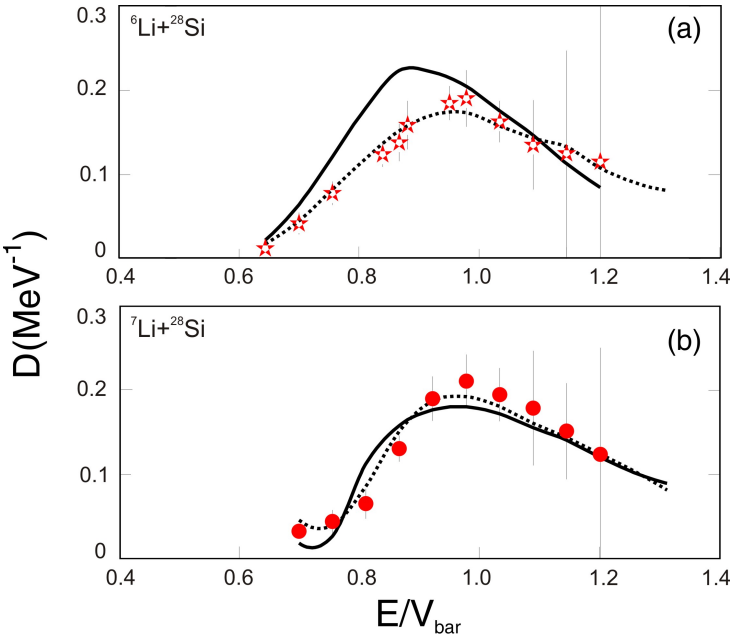

Figure 4.34: *Experimental data of barrier distributions for (a) $^{6}Li + ^{28}Si$ and (b) $^{7}Li + ^{28}Si$, are compared with fresco CDCC calculations. Solid lines refer to uncoupled calculation while the dashed lines represent coupled channel calculations to continuum.*

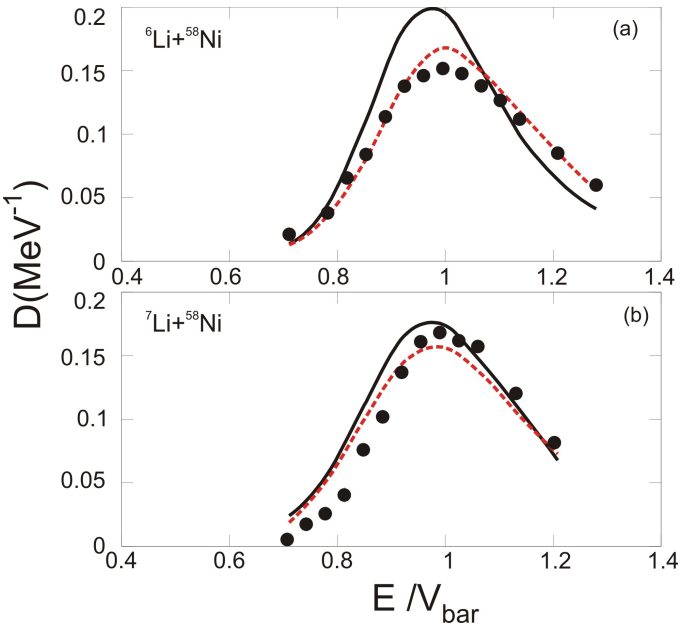

Figure 4.35: *Experimental data of barrier distributions for (a) $^{6}Li + ^{58}Ni$ and (b) $^{7}Li + ^{58}Ni$, are compared with fresco CDCC calculations. Solid lines refer to uncoupled calculation while the dashed lines represent coupled channel calculations to continuum.*

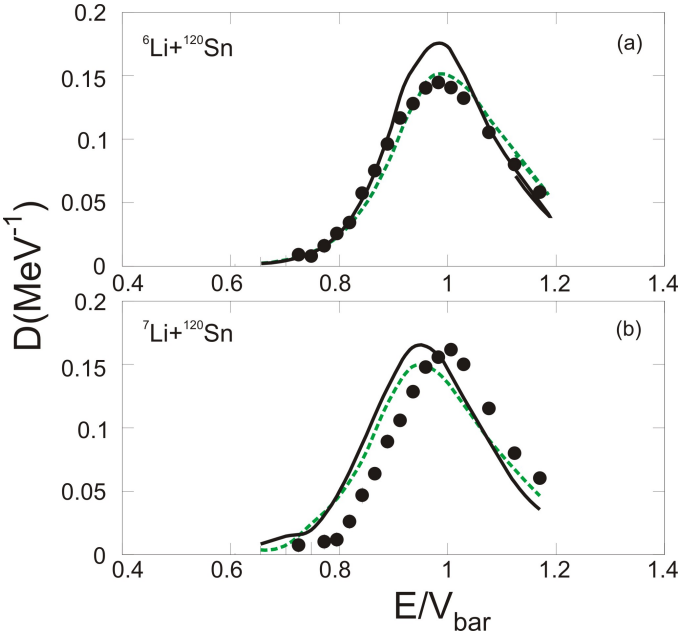

Figure 4.36: *Experimental data of barrier distributions for (a) $^{6}Li + ^{120}Sn$ and (b) $^{7}Li + ^{120}Sn$, are compared with fresco CDCC calculations. Solid lines refer to uncoupled calculation while the dashed lines represent coupled channel calculations to continuum.*

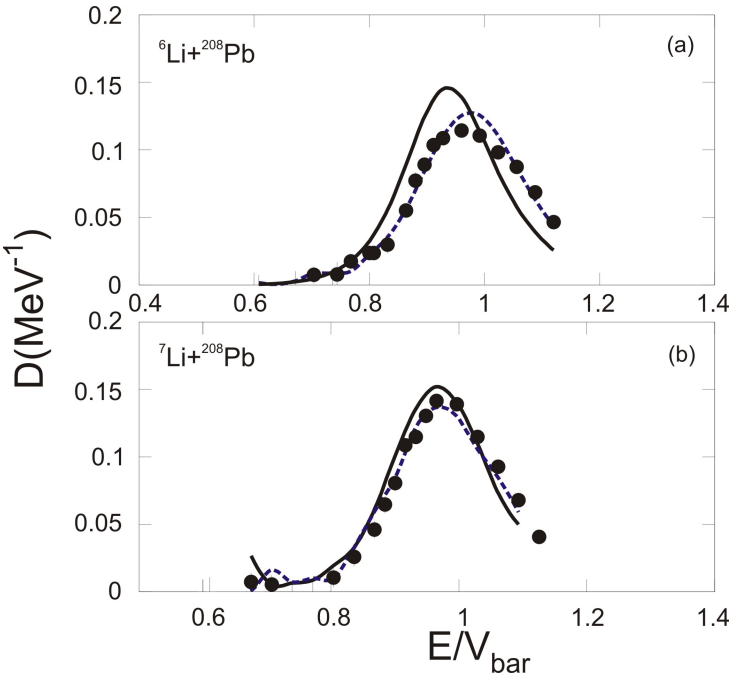

Figure 4.37: *Experimental data of barrier distributions for (a) $^{6}Li + ^{208}Pb$ and (b) $^{7}Li + ^{208}Pb$, are compared with fresco CDCC calculations. Solid lines refer to uncoupled calculation while the dashed lines represent coupled channel calculations to continuum.*

Chapter 5

Discussion and Conclusions

Elastic backscattering excitation functions and the corresponding barrier distributions were measured for $^{6,7}Li$ projectiles incident on ^{28}Si, ^{58}Ni, $^{116,120}Sn$ and ^{208}Pb targets. For these systems, the optical potential based on dispersion relations was probed in a systematic way at energies close to and well below the barrier at deep sub-barrier energies. Although a lack of systematic behavior prohibits the deduction of a global optical potential for weakly bound projectiles at sub-barrier energies, considerable conclusions can be drawn and may be summarized as follows:

1. The backscattering barrier distribution technique is a new method and can be used as a very valuable tool for predicting in a complementary way, the optical potential at low energies. It is at the moment the only tool for predicting the potential to some extend at energies below the barrier, where the conventional angular distribution technique is not sensitive to the nuclear potential, since the nuclear part of the potential is very weak in comparison to the Coulomb part. Our new technique is very sensitive since the barrier distribution depends on the derivative of differential elastic scattering cross sections, so even a small change in the potential has a substantial effect on the barrier distribution. But in order to provide detailed information on this issue, extensive and precise experimental data of various kinds are required. Unfortunately at these low energies the measurement of reaction cross-sections of any type is a very difficult task.

2. For weakly bound nuclei the imaginary potential persists either with an increasing trend (^6Li) or a flat behavior (^7Li) to sub-barrier energies near $E/V_{bar} = 0.5$, in contrast with well-bound nuclei where the loss of flux from the elastic channel stops around the Coulomb barrier. For some targets the potential fall occurs at very low energies, $E/V_{bar} = 0.2$, associated with a very large real part, unexpected under physical conditions. This fact puts on stake the validity of the dispersion relation.

3. For ^{6}Li the rising part has the largest slope for the heavier targets and the smallest slope for the lighter ones, possibly indicating in a qualitative interpretation that the competition between breakup and transfer or some compound procedure at energies at the barrier is in favor of breakup. However, as we proceed to lower sub-barrier energies, the competition of the various channels is not clear but only under a complete set of reaction cross-section measurements.

4. For ^{7}Li, while the backscattering technique also proves to be a valuable tool for predicting the potential at very low sub-barrier energies, it is not sensitive enough to distinguish between a potential obeying the dispersion relation and one which does not, although the trend is in favor of the second scenario. Studies including other targets are necessary to pin down this problem.

In principle, it can be shown that the optical potential that comes out of Feshbach theory must formally satisfy a dispersion relation. However, this is a theoretical construct and therefore not the same as the empirical optical potential that was obtained from fits to elastic scattering data. Therefore, the empirical optical potential does not necessarily have to satisfy a dispersion relation. In the present case, with caution it can be said that this is observed as an absence of an energy dependence of the potential, an observation which can generate an important theoretical work. A possible explanation, although under theoretical investigation for the moment, is that this is due to the interference of the repulsive polarization potential due to the break-up process, with the attractive polarization potential generated by transfer reactions involving the bound excited state of ^{7}Li. The strength of these two components of the polarization potential could be equal and of opposite sign one repulsive the other attractive and the net effect may be a non-energy dependent optical potential. The presence or a possible absence of the so-called break-up threshold anomaly in the optical potential of the scattering of weakly bound nuclei is a question of paramount importance. It may challenge our current theoretical understanding of low energy reaction dynamics involving weakly bound nuclei and modify our current understanding of the genesis and production rate of some nuclei produced in stellar explosions.

This work, which has been presented in the publications [89, 90, 91], is the first to experimentally demonstrate that the break-up threshold anomaly although present in the case of elastic scattering including ^{6}Li projectiles was absent in the case of ^{7}Li nuclei. This experimental finding for a silicon target [90] raised an important criticism and a consequent experimental and theoretical work. Since our first publications, the absence of the threshold anomaly in the case of ^{7}Li, that is the absence of energy dependence of the real and imaginary part of the optical potential, has been reported in a number of experimental papers by other groups and for other mass regions as well and now reported in a more systematic way in this work. This result should

initiate more studies including other targets and various techniques from the point of view of the potential and the reaction mechanism itself. Moreover in this study the validity of dispersion relation has also been questioned in the case of ^{6}Li projectiles.

From the point of view of the reaction mechanisms, via the CDCC calculations it became clear once more that couplings to the continuum are strong and important. This fact was also verified in similar work on samarium, thorium and lead in [53, 54, 55, 56]. However, to obtain a full insight into the reaction mechanism and how it is related to the predicted optical potential more work from the experimental and theoretical points of view is necessary. This should include backscattering measurements from several targets, transfer and breakup measurements for the same targets the latter as tracers of the predicted potentials as well as full CRC calculations where transfer will be included simultaneously with breakup. The case of $^{7}Li +^{120} Sn$ remains open to a new CDCC calculation since at the moment our calculation fails to describe our data [91].

In Summary

We have determined barrier distributions, and through these the energy dependence of the optical potential, via elastic backscattering for $^{6,7}Li$ on ^{58}Ni, $^{116,120}Sn$ and ^{208}Pb. Optical potentials based on the dispersion relation were probed at near- and sub-barrier energies indicating a loss of flux till very low energies, even below $0.5V_{Coulomb}$ for both weakly bound projectiles, although the energy dependence varies between them. Further on, it was found that the energy dependence between different targets but the same projectile is unique, possibly due to the involvement of different reaction mechanisms, therefore different polarization potentials. The validity of the dispersion relation is questioned but not clearly concluded for both projectiles. The new systematic results indicate that the backscattering technique, by forming barrier distributions, is valuable tool for probing the potential at very low sub-barrier energies, acting complementary to conventional angular distribution and reaction cross-section measurements. Such results can also indicate the importance of coupling to the continuum without, however, giving clear insight into the reaction mechanism.

Bibliography

[1] P. E. Hodgson, *The nucleon Optical Model*, World Scientific, ISBN 981-02-1722-6

[2] M. E. Brandan, G. R. Satchler, Phys. Reports 285 (1997) 143-243

[3] N. Alamanos, P. Roussel-Chomaz, Ann. Phys. Fr. 21 (1996) 601-668.

[4] C. Mahaux, H. Ngo and G. R. Satchler, Nucl. Phys. A 449 (1986) 354-394

[5] M. A. Nagarajan, C. C. Mahaux and G. R. Satchler, Phys. Rev. Lett. 54 (1985) 1136.

[6] G. R. Satchler, Physics Reports 199 No.3 (1991) 147-190.

[7] J. M. Figueira et al, Phys. Rev. C 73 054603 (2006)

[8] J. Lubian et al, Nucl. Phys. A 791 24 (2007)

[9] J. Lubian et al, Phys. Rev. C 78, 064615 (2008)

[10] G. R. Satchler and W. Love, Phys. Rep. 55 183 (1979)

[11] N. Keeley et al. Nucl. Phys. A571 (1994) 326

[12] A. Pakou et al. Phys. Lett. B 556, 21 (2003)

[13] A. Pakou et al. Phys. Rev. C 69, 054602 (2004)

[14] A. Pakou and K. Rusek PRC 69 057602 (2004)

[15] A. Pakou et al Phys. Lett. B633, 691 (2006)

[16] A. Pakou Phys. Rev. C 78 067601 (2008)

[17] A.M.M. Maciel et al. Phys. Rev. C 59, 2103 (1999)

[18] J. M. Figueira et al., Phys. Rev. C 73, 054603 (2006)

[19] J. M. Figueira et al., Phys Rev. C75, 017602 (2007)

[20] J. Fernandez et al., Nucl. Phys. A 787, 484 (2007)

[21] F. A. Souza et al., Phys. Rev. C 75, 044601 (2007)

[22] M. Biswas et al., Nucl. Phys. A 802, 67 (2008)

[23] H. Kumawat et al., Phys. Rev C78, 044617 (2008)

[24] M. Zadro et al., Phys. Rev. C80, 064610 (2009)

[25] E.F. Aguilera et al., Phys. Rev. C 79, 021601(R) (2009)

[26] J. M. Figueira et al., Phys. Rev. C81, 024613 (2010)

[27] A. Camacho et al., Nucl. Phys. A 833, 156 (2010)

[28] A. Gomez Camacho, P. R. S. Gomes, and J. Lubian, Phys. Rev. C 82, 067601 (2010)

[29] A. Gomez Camacho et al., Nucl. Phys. A 833, 156 (2010).

[30] A. Gomez Camacho et al., J. of Phys: Conference Series 239 (2010) 012015

[31] A. E. Woodard et al. Nucl. Phys. A 873 17-27 (2012)

[32] A. Gomez Camacho et al. Phys. Rev. C 84, 034615 (2011)

[33] L. Fimiani et al., PRC 86, 044607 (2012)

[34] N. Rowley, G.R. Satchler, P.H. Stelson, Phys. Lett. B 254, 25 (1991)

[35] M. A. Candido Ribeiro, L. C. Chamon, D. Pereira, M. S. Hussein and D. Galetti, Phys. Rev. Lett. 78, 3270 (1997)

[36] M. Dasgupta, D. Hinde, N. Rowley, A. Stefanini, Annu. Rev. Nucl. Part. Sci. 48, 401 (1998)

[37] L.F. Canto, P.R.S. Gomes, R. Donangelo, M.S. Hussein, Phys. Rep. 424, 1 (2006)

[38] N. Keeley, R. Raabe, N. Alamanos, J.L. Sida, Prog. Part. Nucl. Phys. 59, 579 (2007)

[39] M. S. Hussein, P. R. S. Gomes, J. Lubian, and L. C. Chamon, Phys. Rev. C 76, 019902(E) (2007)

[40] N. Keeley, N. Alamanos, K.W. Kemper, K. Rusek, Prog. Part. Nucl. Phys. 63, 396 (2009)

[41] M. A. Nagarajan and G.R. Satchler, Phys Lett B 173, 29 (1986)

[42] Y. Sakuragi, et al., Prog. Theor. Phys. 68 (1982) 322

[43] Y. Sakuragi, et al., Prog. Theor. Phys. 70 (1983) 525

[44] N. Rowley, H. Timmers, et all, Phys. Let. B 373 (1996) 23-29

[45] I.I. Gontchar, D.J. Hinde, M. Dasgupta, J.O. Newton, Nucl. Phys. A 722, 479c (2003)

[46] K. Hagino, T. Takehi, A.B. Balantekin, N. Takigawa, Phys. Rev. C 71, 044612 (2005)

[47] K. Washiyama, K. Hagino, M. Dasgupta, Phys. Rev. C 73, 034607 (2006)

[48] L.R. Gasques et al., Phys. Rev. C 76, 024612 (2007)

[49] O.A. Capurro et al., Phys. Rev. C 75, 047601 (2007)

[50] M. Evers et al., Phys. Rev. C 78, 034614 (2008)

[51] J.F.P. Huiza et al., Phys. Rev. C 82, 054603 (2010).

[52] E. Crema et al., Phys. Rev. C 84, 024601 (2011)

[53] C.J. Lin et al., Nucl. Phys. A 787, 281c (2007)

[54] D.S. Monteiro et al., Phys. Rev. C 79, 014601 (2009)

[55] D.R. Otomar et al., Phys. Rev. C 80, 034614 (2009)

[56] S. Mukherjee et al., Phys. Rev. C 80, 014607 (2009)

[57] Kenneth S. Krane, *Introductory Nuclear Physics*, ISBN 0471 85914 1

[58] G. R. Satchler, *Introduction to Nuclear Reactions, second edition*, ISBN 0333 52379 2

[59] Sammuel S. M. Wong, *Introductory Nuclear Physics, second edition*, ISBN 0471 23973 9

[60] R. R. Roy, B. P. Nigan, *Nuclear Physics: Theory and experiment*, ISBN 0471 74383 6

[61] G. R. Satchler, *Direct Nuclear Reactions*, ISBN 019-851269-4

[62] J. S. Lilley, B. R. Fulton, M. A. Nagarajan, I. S. Thompson and D. w. Banes, Phys. Lett. B 151 (1985) 181.

[63] A. Baeza, B. Bilwes, R. Bilwes, J. Diaz and J. L. Ferrero, Nucl. Phys. A 419 (1984) 181.

[64] J. M. Cornwall and M. A. Ruderman, Phys. Rev. 128 (1962) 1474.

[65] H. Timmers et all., Nucl. Phys. A 584, 190 (1995)

[66] R. F. Simoes et al., Phys. Lett. B527, 187 (2002).

[67] J. M. B. Shorto et al., Phys. Rev. C 78, 064610 (2008).

[68] K.Hagino, N. Rowley, Phys. Rev. C 69, 054610 (2004).

[69] http://www.slcj.uw.edu.pl/en/57.html

[70] H. Timmers et al., J. Phys. G 23, 1175 (1997)

[71] H. Timmers et al., Nucl. Phys. A633, 421 (1998)

[72] H.Timmers Brazilian J. of Phys. 33 no 2 (2003)

[73] H.Timmers Ph.D. thesis, Expressions of Inner Freedom, An Experimental Study of the Scattering and Fusion of Nuclei at Energies Spanning the Coulomb Barrier, http://thesis.anu.edu.au/public/adt-ANU20020328.152158, Australian National University, Canberra, Australia (1996).

[74] tandem.inp.demokritos.gr

[75] http://www.lns.infn.it/index.php?option=com_contentview=articleid=75 Itemid=108

[76] Camac data acquisition system, H. Steltzer, private communication, E-mail: h.steltzer@gsi.de.

[77] R.A. Broglia, A. Winther, Heavy Ion Reactions, Vol. I: Elastic and Inelastic Reactions, BenjaminCummings, Redwood City, CA, 1981.

[78] E. Piasecki et al., Phys. Rev. C 65, 054611 (2002)

[79] D.T. Khoa et al., Phys. Lett. B 342, 6 (1995).

[80] H.D. Vries, C.W. Jager, C. De Vries, At. Data Nucl. Data Tables 14, 479 (1974)

[81] K.H. Bray et al., Nucl. Phys. 189, 35 (1972)

[82] L. Trache et al., Phys. Rev. C 61, 024612 (2000) and private communication.

[83] J. Raynal, Phys. Rev. C 23, 2571 (1981)

[84] I.J. Thompson, Comput. Phys. Rep. 7, 167 (1988)

[85] K.O. Pfeiffer, E. Speth, K. Berthge, Nucl. Phys. A 206, 545 (1973).

[86] N.N. Deshmukh et al., Phys. Rev. C 83, 024607 (2011).

[87] N. Keeley et al., Nucl. Phys. A 571, 326 (1994).

[88] A. Pakou et al. Phys Rev. C76, 054601 (2007)

[89] K. Zerva et al., Phys. Rev. C 80, 017601 (2009)

[90] K. Zerva et al., Phys. Rev. C 82, 044607 (2010)

[91] K. Zerva et al., Eur. Phys. J. A 48 (2012)

[92] W. R. Leo, *Techniques for Nuclear and Particle Physics Experiments, second edition*, ISBN 0387 572805

Appendix A

Mathematical Preliminaries

A.1 The angular momentum operator

The angular momentum of a particle is given by:

$$\vec{L} = \vec{r} \times \vec{r} \tag{A.1}$$

where $\vec{r}$ is the position vector of the particle relative to the origin and $\vec{p}$ is the linear momentum of the particle. The components of the angular momentum operator are:

$$\begin{aligned} L_x &= yp_z - zp_y = -i\hbar\Big(y\frac{\partial}{\partial z} - z\frac{\partial}{\partial y}\Big) \\ &= i\hbar\Big(\sin\phi\frac{\partial}{\partial\theta} + \cot\theta\cos\phi\frac{\partial}{\partial\phi}\Big) \end{aligned} \tag{A.2}$$

$$\begin{aligned} L_y &= zp_x - xp_z = -i\hbar\Big(z\frac{\partial}{\partial x} - x\frac{\partial}{\partial z}\Big) \\ &= i\hbar\Big(-\cos\phi\frac{\partial}{\partial\theta} + \cot\theta\sin\phi\frac{\partial}{\partial\phi}\Big) \end{aligned} \tag{A.3}$$

$$\begin{aligned} L_z &= xp_y - yp_z = -i\hbar\Big(x\frac{\partial}{\partial y} - y\frac{\partial}{\partial x}\Big) \\ &= -i\hbar\frac{\partial}{\partial\phi} \end{aligned} \tag{A.4}$$

and

$$\mathbf{L}^2 = L_x^2 + L_y^2 + L_z^2 = -\hbar^2\Big[\frac{1}{\sin\theta}\frac{\partial}{\partial\theta}\Big(\sin\theta\frac{\partial}{\partial\theta}\Big) + \frac{1}{\sin^2\theta}\frac{\partial^2}{\partial\phi^2}\Big] \tag{A.5}$$

A.2 Spherical Harmonics

The eigenfunctions of the operators $\mathbf{L}^2$ and L_z are the spherical harmonics $Y_{lm}(\theta, \phi)$.

$$\mathbf{L}^2 Y_{lm}(\theta, \phi) = l(l+1)\hbar^2 Y_{lm}(\theta, \phi) \tag{A.6}$$

$$L_z^2 Y_{lm}(\theta, \phi) = m\hbar Y_{lm}(\theta, \phi) \tag{A.7}$$

The spherical harmonics $Y_{lm}(\theta, \phi)$ are defined in terms of the associated Legendre polynomials as:

$$Y_{lm}(\theta, \phi) = \sqrt{\frac{2l+1}{4\pi}\frac{(l-m)!}{(l+m)!}}(-1)^m e^{im\phi} P_{lm}(\cos\theta) \tag{A.8}$$

where

$$P_{lm}(\cos\theta) = \frac{(-1)^{l+m}}{2^l l!}\frac{(l+m)!}{(l-m)!}\sin^{-m}\theta\frac{d^{l-m}}{d(\cos\theta)^{l-m}}\sin^{2l}\theta \tag{A.9}$$

with $-l \leq m \leq l$.

The complex conjugate spherical harmonic $Y_{lm}^*(\theta, \phi)$ is given in terms of the negative m by the relation

$$Y_{lm}^*(\theta, \phi) = (-1)^m Y_{l,-m}(\cos\theta) \tag{A.10}$$

The spherical harmonics form an orthonormal set

$$\int_0^{2\pi}\int_0^{\pi} Y_{lm}^*(\theta, \phi) Y_{l'm'}(\theta, \phi) d\Omega = \delta_{ll'}\delta_{mm'} \tag{A.11}$$

where the solid angle $d\Omega = d\hat{r} = \sin\theta d\theta d\phi$

Under space reversal $\mathbf{r} \to -\mathbf{r}$, $\theta \to \pi - \theta$ and $\phi \to \pi + \phi$ so that $e^{im\phi} \to (-1)^m e^{im\phi}$, $P_{lm}(\cos\theta) \to (-1)^{l+m} P_{lm}(\cos\theta)$, and therefore

$$Y_{lm}(\theta, \phi) \to (-1)^l Y_{lm}(\theta, \phi) \quad \text{under} \quad \mathbf{r} \to -\mathbf{r} \tag{A.12}$$

Some useful spherical harmonics are:

$$Y_{l0}(\theta, \phi) = \sqrt{\frac{2l+1}{4\pi}} P_l(\cos\theta) \tag{A.13}$$

$$Y_{lm}(0, \phi) = \sqrt{\frac{2l+1}{4\pi}}\delta_{m0} \tag{A.14}$$

A.3 Pauli matrices

The Pauli matrices are a set of three 2 2 complex matrices which are Hermitian and unitary.
Spin:

$$\vec{S} = \frac{\hbar}{2}\vec{\sigma} \tag{A.15}$$

Isospin:

$$\vec{t} = \frac{1}{2}\vec{\tau} \tag{A.16}$$

$$\begin{gathered} \sigma_1 = \tau_1 = \begin{pmatrix} 0 & 1 \\ 1 & 0 \end{pmatrix} \qquad \sigma_2 = \tau_2 = \begin{pmatrix} 0 & -i \\ i & 0 \end{pmatrix} \\ \sigma_3 = \tau_3 = \begin{pmatrix} 1 & 0 \\ 0 & -1 \end{pmatrix} \end{gathered} \tag{A.17}$$

A.4 Yukawa potential

A Yukawa potential is a potential of the form:

$$V(r) = -g^2 \frac{e^{-\mu r}}{r} \tag{A.18}$$

where g is a constant, $\mu = \frac{mc}{\hbar}$ and r is the radial distance to the particle. The potential is monotone increasing, implying that the force is always attractive.

Appendix B

Surface barrier silicon detectors

The detectors used in this experiment were Silicon Surface Barrier Detectors (SSB) which belong in the category of Semiconductor Detectors. Semiconductor detectors are based on crystalline semiconductor materials. The passage of ionizing radiation creates electron-hole pairs which are collected by an electric field. For charged particle detection, silicon is the most widely used semiconductor material as it has the advantage of room temperature operation.

The most widely used silicon detectors for charged particle measurements are the surface barrier detectors (SSB). These detectors rely on the junction formed between a semiconductor and certain metals, usually n-type silicon with gold or p-type silicon with aluminum. Because of the different Fermi levels in these materials, a contact *emf* arises when the two are put together. This causes a lowering of the band levels in the semiconductor as illustrated in figure 2.4. Such junctions are also known as Schottky barriers. An electric

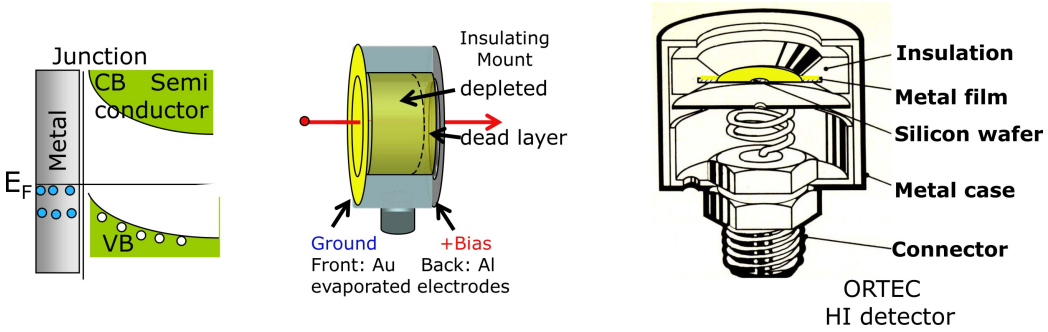

Figure B.1: *Formation of a Schottky barrier junction, and the schematic diagram of a surface barrier detector (from Ortec)*

field is created across the junction and as a consequence there is a potential difference. This is known as contact potential and in case of silicon is on the order of $1V$. The region of changing potential is the depletion zone and its

width can be calculated using the following formula:

$$d = x_n = \sqrt{\frac{2\epsilon V_0}{eN_D}}$$

where ϵ is the dielectric constant, e is the charge of the electron, N_d is the donor impurity and V_0 is the contact potential. Surface barrier detectors can be made with varying thickness and depletion zone regions [92].

Appendix C

Error Theory

C.1 Propagation of errors

The *mean* $\bar{x}$ or *expectation value* $< x >$ of experimental data containing N elements, or measurements, is given by the sum of all elements of the measured quantity x divided by the number of the elements.

$$\bar{x} \equiv \frac{1}{N} \sum_{i=1}^{N} x_i \tag{C.1}$$

The data $x_1, x_2, \ldots, x_n$ are dispersed around the mean. A measurement of this dispersion is called *standard deviation* and is given by:

$$\Delta x \equiv \sqrt{\frac{1}{N} \sum_{i=1}^{N} (x_i - \bar{x})^2} \tag{C.2}$$

In an experiment, the quantities measured are not the quantities of final interest. Since all measurements have uncertainties associated with them, any calculated quantity will have an uncertainty that is related to the uncertainties of the direct measurements. Consider the general case first. Suppose the variables $A, B, C, \ldots$ which represent independent measurable quantities that will be used to obtain a value of some calculated quantity U. Since U is a function of $A, B, C, \ldots$ it can be written as $U = f(A, B, C, \ldots)$. The quantities $A, B, C, \ldots$ have the expectation values $\bar{A}, \bar{B}, \bar{C}, \ldots$ and the associated uncertainties $\Delta A, \Delta B, \Delta C, \ldots$ In order to find the expectation value for the quantity U, the expectation value of each measured variable is substituted into the equation for U:

$$\bar{U} = f(\bar{A}, \bar{B}, \bar{C}, \ldots) \tag{C.3}$$

If the errors for $A, B, C, \ldots$ are independent, random and sufficiently small, the uncertainty for U is given by:

$$\Delta U = \sqrt{\left(\frac{\partial U}{\partial A} \Delta A\right)^2 + \left(\frac{\partial U}{\partial B} \Delta B\right)^2 + \left(\frac{\partial U}{\partial C} \Delta C\right)^2 + \ldots} \tag{C.4}$$

where the partial derivatives are evaluated using the expectation values $\bar{A}, \bar{B}, \bar{C}, \ldots$ The final estimate for the calculated quantity U is given by: $U = \bar{U} + \Delta U$.

C.2 Weighted mean

The weighted mean is similar to an arithmetic mean, where instead of each of the data points contributing equally to the final average, some data points contribute more than others. The weighted mean of a set of data $x_1, x_2, \ldots x_n$ with non-negative weights $w_1, w_2, \ldots w_n$ is the quantity:

$$\bar{x} = \frac{\sum_{i=1}^{n} w_i x_i}{\sum_{i=1}^{n} w_i} \tag{C.5}$$

Therefore data elements with a high weight contribute more to the weighted mean than do elements with a low weight. The weights cannot be negative. Some may be zero, but not all of them (since division by zero is not allowed). If all the weights are equal, then the weighted mean is the same as the arithmetic mean.

C.3 Energy centrifugal correction

When the energy depends on the angle of the scattered ions the centrifugal correction is necessary.

$$E_{eff} = E_{cms}\Big[1 - \frac{\mathrm{cosec}(\frac{\theta_{cms}}{2}) - 1}{\mathrm{cosec}(\frac{\theta_{cms}}{2}) + 1}\Big] \tag{C.6}$$

Appendix D

Experimental excitation functions and barrier distributions

D.1 Data for the system $^{6}Li +^{28} Si$

Table D.1: Excitation function

$\mathbf{E_{lab}}$ (MeV)	$\mathbf{E_{lab}/V_{bar}}$	$\sigma/\sigma_{\mathbf{Ruth}}$	error
5	0.585	0.9554	0.0181
5.5	0.644	1.0023	0.0156
6	0.703	0.9786	0.0164
6.5	0.761	0.8800	0.0200
7	0.820	0.8307	0.0205
7.25	0.849	0.7963	0.0178
7.5	0.878	0.7591	0.0218
8	0.937	0.5979	0.0297
9	1.054	0.3394	0.0322
10	1.171	0.2473	0.0405
11	1.288	0.1103	0.16158

Table D.2: Barrier Distribution

$\mathbf{E_{lab}}$ (MeV)	$\mathbf{E_{lab}/V_{bar}}$	D ($\mathbf{MeV^{-1}}$)	error
5.5	0.644	0.0123	0.0123
6	0.703	0.0420	0.0130
6.5	0.761	0.0778	0.0140
7.25	0.849	0.1239	0.0146
7.5	0.878	0.1382	0.0223

7.625	0.893	0.1588	0.0289
8.25	0.966	0.1851	0.0202
8.5	0.995	0.1907	0.0337
9	1.054	0.1630	0.0246
9.5	1.112	0.1354	0.0531
10	1.171	0.1252	0.1224
10.5	1.230	0.1150	0.2474

D.2 Data for the system $^{7}Li +^{28} Si$

Table D.3: Excitation function

$\mathbf{E_{lab}}$ **(MeV)**	$\mathbf{E_{lab}/V_{bar}}$	$\sigma/\sigma_{\mathbf{Ruth}}$	**error**
5	0.575	1.0436	0.0218
6	0.69	1.0054	0.0210
6.5	0.748	0.9423	0.0189
7	0.806	0.8768	0.0173
7.5	0.863	0.8213	0.0272
8	0.921	0.6823	0.0213
8.5	0.978	0.5155	0.0317
9	1.036	0.3858	0.0355
10	1.151	0.1944	0.0539
11	1.266	0.1	0.07

Table D.4: Barrier Distribution

$\mathbf{E_{lab}}$ **(MeV)**	$\mathbf{E_{lab}/V_{bar}}$	**D** $(\mathbf{MeV^{-1}})$	**error**
6	0.690	0.0184	0.0149
6.5	0.748	0.0152	0.0287
7	0.806	0.0660	0.0326
7.5	0.863	0.1580	0.0322
8	0.921	0.1920	0.0403
8.5	0.978	0.2170	0.0440
9	1.036	0.1973	0.0300
9.5	1.093	0.1776	0.0652
10	1.151	0.1506	0.0582
10.5	1.208	0.1235	0.1233

D.3 Data for the system $^{6}Li +^{58} Ni$

Table D.5: Excitation function

$\mathbf{E_{lab}}$ (MeV)	$\mathbf{E_{lab}/V_{bar}}$	$\sigma/\sigma_{\mathbf{Ruth}}$	error
9	0.640	0.9977	0.0135
10	0.711	0.9765	0.0127
10.5	0.746	0.9601	0.0126
11	0.782	0.9145	0.0176
11.5	0.817	0.8845	0.0169
12	0.853	0.8318	0.0160
12.5	0.888	0.7200	0.0137
13	0.924	0.6217	0.0121
13.5	0.959	0.5085	0.0097
14	0.995	0.4054	0.0079
14.5	1.031	0.3099	0.0061
15	1.066	0.2354	0.0046
15.5	1.102	0.1748	0.0035
16	1.137	0.1302	0.0026
16.5	1.173	0.0924	0.0019
17	1.208	0.0686	0.0013
18	1.279	0.0365	0.0007
19	1.350	0.0201	0.0005

Table D.6: Barrier Distribution

$\mathbf{E_{lab}}$ (MeV)	$\mathbf{E_{lab}/V_{bar}}$	D ($\mathbf{MeV^{-1}}$)	error
10	0.711	0.0213	0.0057
11	0.782	0.0381	0.0054
11.5	0.817	0.0657	0.0052
12	0.853	0.0839	0.0060
12.5	0.888	0.1137	0.0056
13	0.924	0.1376	0.0054
13.5	0.959	0.1459	0.0049
14	0.995	0.1516	0.0045
14.5	1.031	0.1475	0.0040
15	1.066	0.1380	0.0036
15.5	1.102	0.1263	0.0032
16	1.137	0.1116	0.0027
17	1.208	0.0849	0.0020
18	1.279	0.0600	0.0015

D.4 Data for the system $^{7}Li + ^{58}Ni$

Table D.7: Excitation function

$\mathbf{E_{lab}}$ (MeV)	$\mathbf{E_{lab}/V_{bar}}$	$\sigma/\sigma_{\mathbf{Ruth}}$	error
9	0.636	0.9833	0.0155
9.5	0.672	0.9768	0.0151
10	0.707	0.9648	0.0140
10.5	0.743	0.9328	0.0174
11	0.778	0.9617	0.0165
11.5	0.813	0.9094	0.0167
12	0.849	0.8660	0.0168
12.5	0.884	0.7832	0.0147
13	0.919	0.6867	0.0122
13.5	0.955	0.5625	0.0105
14	0.990	0.4313	0.0080
14.5	1.025	0.3169	0.0060
15	1.061	0.2424	0.0044
15.5	1.096	0.1818	0.0033
16	1.132	0.1172	0.0023
17	1.202	0.0633	0.0016
18	1.273	0.0322	0.0008
19	1.344	0.0056	0.0002

Table D.8: Barrier Distribution

$\mathbf{E_{lab}}$ (MeV)	$\mathbf{E_{lab}/V_{bar}}$	D ($\mathbf{MeV^{-1}}$)	error
10	0.7072	0.0055	0.0057
10.5	0.7426	0.0173	0.0058
11	0.7779	0.0258	0.0058
11.5	0.8133	0.0404	0.0061
12	0.8487	0.0760	0.0056
12.5	0.8840	0.1018	0.0056
13	0.9194	0.1369	0.0054
13.5	0.9547	0.1610	0.0049
14	0.9901	0.1682	0.0043
14.5	1.0254	0.1618	0.0040
15	1.0608	0.1572	0.0035
16	1.1315	0.1204	0.0027
17	1.2023	0.0815	0.0020

D.5 Data for the system $^{6}Li +^{120} Sn$

Table D.9: Excitation function

$\mathbf{E_{lab}}$ (MeV)	$\mathbf{E_{lab}/V_{bar}}$	$\sigma/\sigma_{\mathbf{Ruth}}$	error
12	0.562	0.9882	0.0164
13	0.608	0.9884	0.0151
14	0.655	0.9955	0.0156
14.5	0.679	0.9922	0.0153
15	0.702	0.9787	0.0113
15.5	0.725	0.9904	0.0175
16	0.749	0.9831	0.0153
16.5	0.772	0.9565	0.0151
17	0.796	0.9474	0.0140
17.5	0.819	0.9279	0.0151
18	0.842	0.8833	0.0131
18.5	0.866	0.8264	0.0129
19	0.889	0.7363	0.0115
19.5	0.912	0.6601	0.0104
20	0.936	0.5583	0.0088
20.5	0.959	0.4562	0.0073
21	0.983	0.3623	0.0059
21.5	1.006	0.2823	0.0047
22	1.029	0.2093	0.0033
22.5	1.053	0.1554	0.0026
23	1.076	0.1136	0.0020
24	1.123	0.0608	0.0011
25	1.170	0.0314	0.0006

Table D.10: Barrier Distribution

$\mathbf{E_{lab}}$ (MeV)	$\mathbf{E_{lab}/V_{bar}}$	D ($\mathbf{MeV^{-1}}$)	error
13	0.6075	0.0018	0.0057
14	0.6542	0.0025	0.0048
15	0.7009	0.0031	0.0055
15.5	0.7243	0.0090	0.0054
16	0.7477	0.0080	0.0046
16.5	0.7710	0.0159	0.0059
17	0.7944	0.0258	0.0052
17.5	0.8178	0.0345	0.0052
18	0.8411	0.0576	0.0049
18.5	0.8645	0.0754	0.0051
19	0.8878	0.0963	0.0045

19.5	0.9112	0.1168	0.0044
20	0.9346	0.1281	0.0041
20.5	0.9579	0.1405	0.0039
21	0.9813	0.1448	0.0034
21.5	1.0047	0.1406	0.0032
22	1.0280	0.1324	0.0028
23	1.0748	0.1054	0.0021
24	1.1215	0.0800	0.0017
25	1.1682	0.0582	0.0012

D.6 Data for the system $^{7}Li +^{120} Sn$

Table D.11: Excitation function

$\mathbf{E_{lab}}$ **(MeV)**	$\mathbf{E_{lab}/V_{bar}}$	$\sigma/\sigma_{\mathbf{Ruth}}$	**error**
12	0.563	0.9837	0.0182
13	0.609	0.9826	0.0173
14	0.656	0.9785	0.0169
14.5	0.680	0.9905	0.0173
15	0.703	0.9790	0.0174
15.5	0.727	0.9847	0.0175
16	0.750	0.9721	0.0170
16.5	0.774	0.9598	0.0162
17	0.797	0.9641	0.0179
17.5	0.820	0.9444	0.0164
18	0.844	0.9258	0.0159
18.5	0.867	0.8601	0.0147
19	0.891	0.7888	0.0152
19.5	0.914	0.7122	0.0098
20	0.938	0.6145	0.0119
20.5	0.961	0.5123	0.0102
21	0.985	0.3985	0.0078
21.5	1.008	0.3002	0.0056
22	1.031	0.2233	0.0042
22.5	1.055	0.1540	0.0029
23	1.078	0.1097	0.0021
24	1.125	0.0584	0.0011
25	1.172	0.0292	0.0006
26	1.220	0.0146	0.0003

Table D.12: Barrier Distribution

$\mathbf{E_{lab}}$ (MeV)	$\mathbf{E_{lab}/V_{bar}}$	D ($\mathbf{MeV^{-1}}$)	error
16	0.750	0.0038	0.0063
16.5	0.774	0.0102	0.0061
17	0.797	0.0119	0.0060
17.5	0.820	0.0261	0.0057
18	0.844	0.0469	0.0062
18.5	0.867	0.0640	0.0051
19	0.891	0.0892	0.0056
19.5	0.914	0.1058	0.0053
20	0.938	0.1284	0.0053
20.5	0.961	0.1480	0.0039
21	0.985	0.1557	0.0044
21.5	1.008	0.1617	0.0040
22	1.031	0.1501	0.0035
23	1.078	0.1154	0.0025
24	1.125	0.0801	0.0018
25	1.172	0.0605	0.0013

D.7 Data for the system $^{6}Li +^{208} Pb$

Table D.13: Excitation function

$\mathbf{E_{lab}}$ (MeV)	$\mathbf{E_{lab}/V_{bar}}$	$\sigma/\sigma_{\mathbf{Ruth}}$	error
20	0.641	0.9956	0.0189
21	0.673	1.0101	0.0214
22	0.705	0.9785	0.0139
22.5	0.721	0.9866	0.0202
23	0.737	0.9806	0.0137
23.5	0.753	0.9676	0.0201
24	0.769	0.9641	0.0179
25	0.801	0.9126	0.0184
26	0.833	0.8733	0.0121
26.5	0.849	0.8512	0.0171
27	0.865	0.8025	0.0153
27.5	0.881	0.7638	0.0108
28	0.897	0.6794	0.0143
28.5	0.913	0.5901	0.0122
29	0.929	0.5153	0.0075
29.5	0.945	0.4448	0.0093
30	0.961	0.3684	0.0073

30.5	0.977	0.3119	0.0062
31	0.993	0.2393	0.0049
32	1.025	0.1490	0.0031
33	1.057	0.0857	0.0018
34	1.089	0.0446	0.0010
35	1.121	0.0242	0.0006
36	1.153	0.0140	0.0003

Table D.14: Barrier Distribution

$\mathbf{E_{lab}}$ **(MeV)**	$\mathbf{E_{lab}/V_{bar}}$	**D** $(\mathbf{MeV^{-1}})$	**error**
19	0.6086	0.0003	0.0068
21	0.6726	0.0043	0.0059
22	0.7047	0.0074	0.0063
23	0.7367	0.0037	0.0058
23.5	0.7447	0.0076	0.0091
24	0.7687	0.0175	0.0059
25	0.8008	0.0237	0.0056
25.5	0.8088	0.0237	0.0052
26	0.8328	0.0297	0.0064
27	0.8648	0.0551	0.0054
27.5	0.8808	0.0772	0.0061
28	0.8969	0.0890	0.0050
29	0.9289	0.1086	0.0053
30	0.9609	0.1143	0.0036
31	0.9930	0.1105	0.0036
32	1.0250	0.0982	0.0029
33	1.0570	0.0874	0.0023
34	1.0890	0.0685	0.0018
35	1.1211	0.0463	0.0014

D.8 Data for the system $^{7}Li + ^{208}Pb$

Table D.15: Excitation function

$\mathbf{E_{lab}}$ (MeV)	$\mathbf{E_{lab}/V_{bar}}$	$\sigma/\sigma_{\mathbf{Ruth}}$	error
20	0.643	0.9994	0.0180
21	0.675	1.0106	0.0206
22	0.707	0.9700	0.0199
22.5	0.723	0.9756	0.0196
23	0.740	0.9891	0.0198
23.5	0.756	0.9648	0.0194
24	0.772	0.9692	0.0195
25	0.804	0.9778	0.0203
26	0.836	0.9284	0.0182
26.5	0.852	0.9203	0.0183
27	0.868	0.8782	0.0177
27.5	0.884	0.8482	0.0157
28	0.900	0.7589	0.0154
28.5	0.916	0.6889	0.0140
29	0.932	0.6017	0.0124
29.5	0.949	0.4954	0.0100
30	0.965	0.4113	0.0084
30.5	0.981	0.3236	0.0065
31	0.997	0.2427	0.0049
32	1.029	0.1320	0.0026
33	1.061	0.0693	0.0015
34	1.093	0.0316	0.0007
35	1.125	0.0162	0.0004
36	1.158	0.0093	0.0003

Table D.16: Barrier Distribution

$\mathbf{E_{lab}}$ (MeV)	$\mathbf{E_{lab}/V_{bar}}$	D ($\mathbf{MeV^{-1}}$)	error
23	0.7395	0.0002	0.0071
24	0.7717	0.0028	0.0072
25	0.8039	0.0105	0.0068
26	0.8360	0.0259	0.0070
27	0.8682	0.0462	0.0065
27.5	0.8842	0.0647	0.0064
28	0.9003	0.0807	0.0062
28.5	0.9164	0.1086	0.0055
29	0.9325	0.1149	0.0055
29.5	0.9486	0.1306	0.0051

30	0.9646	0.1415	0.0047
31	0.9968	0.1390	0.0038
32	1.0289	0.1148	0.0029
33	1.0611	0.0927	0.0021
34	1.0932	0.0679	0.0016
35	1.1254	0.0407	0.0013

Appendix E

Calculated optical potentials

E.1 Potential for the system $^{6}Li +^{28} Si$

Table E.1: Normalization factors of the real and imaginary potential

E	$\mathbf{E/V_{bar}}$	$\mathbf{N_{real}}$	$\mathbf{N_{imag}}$
5	0.585	1.048	1.223
5.5	0.644	0.985	1.189
6	0.703	0.929	1.155
6.5	0.761	0.883	1.124
7	0.820	0.838	1.087
7.5	0.878	0.797	1.055
8	0.937	0.764	1.024
8.5	0.995	0.730	0.99
9	1.054	0.701	0.956
9.5	1.112	0.677	0.924
10	1.171	0.654	0.89
10.5	1.230	0.634	0.856
11	1.288	0.617	0.822

Table E.2: BDM3Y interaction at $E = 9\ MeV$

R (**fm**)	**interaction**(MeV)	**R** (**fm**)	**interaction**(MeV)	**R** (**fm**)	**interaction**(MeV)
0.100	-283.8458862305	0.200	-283.3797912598	0.300	-282.6036987305
0.400	-281.5188903809	0.500	-280.1271057129	0.600	-278.4302978516
0.700	-276.4313964844	0.800	-274.1333923340	0.900	-271.5401000977
1.000	-268.6556091309	1.100	-265.4847106934	1.200	-262.0327148438
1.300	-258.3053894043	1.400	-254.3092041016	1.500	-250.0513000488
1.600	-245.5395050049	1.700	-240.7821960449	1.800	-235.7886047363
1.900	-230.5688934326	2.000	-225.1338958740	2.100	-219.4954071045

2.200	-213.6658935547	2.300	-207.6589965820	2.400	-201.4891052246
2.500	-195.1714935303	2.600	-188.7225952148	2.700	-182.1593933105
2.800	-175.5000000000	2.900	-168.7633056641	3.000	-161.9689941406
3.100	-155.1372985840	3.200	-148.2890930176	3.300	-141.4454956055
3.400	-134.6282043457	3.500	-127.8584976196	3.600	-121.1580963135
3.700	-114.5481033325	3.800	-108.0488967896	3.900	-101.6802978516
4.000	-95.4612808228	4.100	-89.4092788696	4.200	-83.5404663086
4.300	-77.8694076538	4.400	-72.4088821411	4.500	-67.1697769165
4.600	-62.1609916687	4.700	-57.3893890381	4.800	-52.8597488403
4.900	-48.5748481750	5.000	-44.5354385376	5.100	-40.7404212952
5.200	-37.1869201660	5.300	-33.8704414368	5.400	-30.7850799561
5.500	-27.9236602783	5.600	-25.2779693604	5.700	-22.8388996124
5.800	-20.5967006683	5.900	-18.5411205292	6.000	-16.6616096497
6.100	-14.9474496841	6.200	-13.3879098892	6.300	-11.9723701477
6.400	-10.6904201508	6.500	-9.5319490433	6.600	-8.4872303009
6.700	-7.5469479561	6.800	-6.7022590637	6.900	-5.9448118210
7.000	-5.2667670250	7.100	-4.6607971191	7.200	-4.1200919151
7.300	-3.6383440495	7.400	-3.2097380161	7.500	-2.8289310932
7.600	-2.4910299778	7.700	-2.1915740967	7.800	-1.9264990091
7.900	-1.6921210289	8.000	-1.4851069450	8.100	-1.3024480343
8.200	-1.1414350271	8.300	-0.9996321201	8.400	-0.8748583198
8.500	-0.7651603222	8.600	-0.6687934995	8.700	-0.5842028260
8.800	-0.5100033879	8.900	-0.4449645877	9.000	-0.3879939914
9.100	-0.3381234109	9.200	-0.2944956124	9.300	-0.2563525140
9.400	-0.2230246067	9.500	-0.1939212978	9.600	-0.1685214937
9.700	-0.1463668048	9.800	-0.1270533949	9.900	-0.1102263033
10.000	-0.0955737680	10.100	-0.0828218386	10.200	-0.0717302263
10.300	-0.0620882213	10.400	-0.0537111014	10.500	-0.0464371108
10.600	-0.0401246399	10.700	-0.0346497782	10.800	-0.0299041905
10.900	-0.0257931799	11.000	-0.0222340208	11.100	-0.0191545207
11.200	-0.0164916497	11.300	-0.0141904699	11.400	-0.0122030796
11.500	-0.0104877697	11.600	-0.0090082195	11.700	-0.0077328212
11.800	-0.0066340999	11.900	-0.0056881751	12.000	-0.0048743100
12.100	-0.0041745072	12.200	-0.0035731569	12.300	-0.0030567280
12.400	-0.0026135030	12.500	-0.0022333350	12.600	-0.0019074520
12.700	-0.0016282680	12.800	-0.0013892330	12.900	-0.0011846920
13.000	-0.0010097680	13.100	-0.0008602570	13.200	-0.0007325377
13.300	-0.0006234927	13.400	-0.0005304408	13.500	-0.0004510776
13.600	-0.0003834238	13.700	-0.0003257808	13.800	-0.0002766912
13.900	-0.0002349057	14.000	-0.0001993538	14.100	-0.0001691189
14.200	-0.0001434168	14.300	-0.0001215770	14.400	-0.0001030269
14.500	-0.0000872775	14.600	-0.0000739113	14.700	-0.0000625721
14.800	-0.0000529559	14.900	-0.0000448035	15.000	-0.0000378943
15.100	-0.0000320407	15.200	-0.0000270830	15.300	-0.0000228857
15.400	-0.0000193335	15.500	-0.0000163281	15.600	-0.0000137860

15.700	-0.0000116362	15.800	-0.0000098186	15.900	-0.0000082821
16.000	-0.0000069837	16.100	-0.0000058872	16.200	-0.0000049614
16.300	-0.0000041800	16.400	-0.0000035206	16.500	-0.0000029641
16.600	-0.0000024944	16.700	-0.0000020980	16.800	-0.0000017638
16.900	-0.0000014822	17.000	-0.0000012452	17.100	-0.0000010458
17.200	-0.0000008778	17.300	-0.0000007363	17.400	-0.0000006170
17.500	-0.0000005165	17.600	-0.0000004319	17.700	-0.0000003610
17.800	-0.0000003016	17.900	-0.0000002519	18.000	-0.0000002102
18.100	-0.0000001750	18.200	-0.0000001454	18.300	-0.0000001204
18.400	-0.0000000994	18.500	-0.0000000820	18.600	-0.0000000677
18.700	-0.0000000559	18.800	-0.0000000460	18.900	-0.0000000377
19.000	-0.0000000305	19.100	-0.0000000244	19.200	-0.0000000194
19.300	-0.0000000154	19.400	-0.0000000123	19.500	-0.0000000098
19.600	-0.0000000078	19.700	-0.0000000059	19.800	-0.0000000043
19.900	-0.0000000028	20.000	-0.0000000017	20.100	-0.0000000009
20.200	-0.0000000004	20.300	-0.0000000002	20.400	0.0000000001
20.500	0.0000000004	20.600	0.0000000008	20.700	0.0000000012
20.800	0.0000000014	20.900	0.0000000015	21.000	0.0000000013
21.100	0.0000000011	21.200	0.0000000010	21.300	0.0000000011
21.400	0.0000000012	21.500	0.0000000014	21.600	0.0000000015
21.700	0.0000000014	21.800	0.0000000011	21.900	0.0000000009
22.000	0.0000000007				

E.2 Potential for the system $^{7}Li +^{28} Si$

Table E.3: Normalization factors of the real and imaginary potential

E	**E/V$_{bar}$**	**N$_{real}$**	**N$_{imag}$**	**N$_{real}$**	**N$_{imag}$**
5	0.575	0.45	0.05	0.601	0.443
5.5	0.633	0.45	0.05	0.578	0.443
6	0.69	0.45	0.05	0.561	0.443
6.5	0.748	0.45	0.05	0.545	0.443
7	0.806	0.45	0.055	0.532	0.443
7.5	0.863	0.45	0.120	0.519	0.443
8	0.921	0.45	0.179	0.509	0.443
8.5	0.978	0.45	0.243	0.498	0.443
9	1.036	0.45	0.302	0.489	0.443
9.5	1.093	0.45	0.366	0.480	0.443
10	1.151	0.45	0.425	0.472	0.443
10.5	1.208	0.45	0.489	0.464	0.443
11	1.266	0.45	0.50	0.458	0.443

Table E.4: BDM3Y interaction at at $E = 9\ MeV$

R (fm)	**interaction**(MeV)	**R (fm)**	**interaction**(MeV)	**R (fm)**	**interaction**(MeV)
0.100	-283.8458862305	0.200	-283.3797912598	0.300	-282.6036987305
0.400	-281.5188903809	0.500	-280.1271057129	0.600	-278.4302978516
0.700	-276.4313964844	0.800	-274.1333923340	0.900	-271.5401000977
1.000	-268.6556091309	1.100	-265.4847106934	1.200	-262.0327148438
1.300	-258.3053894043	1.400	-254.3092041016	1.500	-250.0513000488
1.600	-245.5395050049	1.700	-240.7821960449	1.800	-235.7886047363
1.900	-230.5688934326	2.000	-225.1338958740	2.100	-219.4954071045
2.200	-213.6658935547	2.300	-207.6589965820	2.400	-201.4891052246
2.500	-195.1714935303	2.600	-188.7225952148	2.700	-182.1593933105
2.800	-175.5000000000	2.900	-168.7633056641	3.000	-161.9689941406
3.100	-155.1372985840	3.200	-148.2890930176	3.300	-141.4454956055
3.400	-134.6282043457	3.500	-127.8584976196	3.600	-121.1580963135
3.700	-114.5481033325	3.800	-108.0488967896	3.900	-101.6802978516
4.000	-95.4612808228	4.100	-89.4092788696	4.200	-83.5404663086
4.300	-77.8694076538	4.400	-72.4088821411	4.500	-67.1697769165
4.600	-62.1609916687	4.700	-57.3893890381	4.800	-52.8597488403
4.900	-48.5748481750	5.000	-44.5354385376	5.100	-40.7404212952
5.200	-37.1869201660	5.300	-33.8704414368	5.400	-30.7850799561
5.500	-27.9236602783	5.600	-25.2779693604	5.700	-22.8388996124
5.800	-20.5967006683	5.900	-18.5411205292	6.000	-16.6616096497
6.100	-14.9474496841	6.200	-13.3879098892	6.300	-11.9723701477

6.400	-10.6904201508	6.500	-9.5319490433	6.600	-8.4872303009
6.700	-7.5469479561	6.800	-6.7022590637	6.900	-5.9448118210
7.000	-5.2667670250	7.100	-4.6607971191	7.200	-4.1200919151
7.300	-3.6383440495	7.400	-3.2097380161	7.500	-2.8289310932
7.600	-2.4910299778	7.700	-2.1915740967	7.800	-1.9264990091
7.900	-1.6921210289	8.000	-1.4851069450	8.100	-1.3024480343
8.200	-1.1414350271	8.300	-0.9996321201	8.400	-0.8748583198
8.500	-0.7651603222	8.600	-0.6687934995	8.700	-0.5842028260
8.800	-0.5100033879	8.900	-0.4449645877	9.000	-0.3879939914
9.100	-0.3381234109	9.200	-0.2944956124	9.300	-0.2563525140
9.400	-0.2230246067	9.500	-0.1939212978	9.600	-0.1685214937
9.700	-0.1463668048	9.800	-0.1270533949	9.900	-0.1102263033
10.000	-0.0955737680	10.100	-0.0828218386	10.200	-0.0717302263
10.300	-0.0620882213	10.400	-0.0537111014	10.500	-0.0464371108
10.600	-0.0401246399	10.700	-0.0346497782	10.800	-0.0299041905
10.900	-0.0257931799	11.000	-0.0222340208	11.100	-0.0191545207
11.200	-0.0164916497	11.300	-0.0141904699	11.400	-0.0122030796
11.500	-0.0104877697	11.600	-0.0090082195	11.700	-0.0077328212
11.800	-0.0066340999	11.900	-0.0056881751	12.000	-0.0048743100
12.100	-0.0041745072	12.200	-0.0035731569	12.300	-0.0030567280
12.400	-0.0026135030	12.500	-0.0022333350	12.600	-0.0019074520
12.700	-0.0016282680	12.800	-0.0013892330	12.900	-0.0011846920
13.000	-0.0010097680	13.100	-0.0008602570	13.200	-0.0007325377
13.300	-0.0006234927	13.400	-0.0005304408	13.500	-0.0004510776
13.600	-0.0003834238	13.700	-0.0003257808	13.800	-0.0002766912
13.900	-0.0002349057	14.000	-0.0001993538	14.100	-0.0001691189
14.200	-0.0001434168	14.300	-0.0001215770	14.400	-0.0001030269
14.500	-0.0000872775	14.600	-0.0000739113	14.700	-0.0000625721
14.800	-0.0000529559	14.900	-0.0000448035	15.000	-0.0000378943
15.100	-0.0000320407	15.200	-0.0000270830	15.300	-0.0000228857
15.400	-0.0000193335	15.500	-0.0000163281	15.600	-0.0000137860
15.700	-0.0000116362	15.800	-0.0000098186	15.900	-0.0000082821
16.000	-0.0000069837	16.100	-0.0000058872	16.200	-0.0000049614
16.300	-0.0000041800	16.400	-0.0000035206	16.500	-0.0000029641
16.600	-0.0000024944	16.700	-0.0000020980	16.800	-0.0000017638
16.900	-0.0000014822	17.000	-0.0000012452	17.100	-0.0000010458
17.200	-0.0000008778	17.300	-0.0000007363	17.400	-0.0000006170
17.500	-0.0000005165	17.600	-0.0000004319	17.700	-0.0000003610
17.800	-0.0000003016	17.900	-0.0000002519	18.000	-0.0000002102
18.100	-0.0000001750	18.200	-0.0000001454	18.300	-0.0000001204
18.400	-0.0000000994	18.500	-0.0000000820	18.600	-0.0000000677
18.700	-0.0000000559	18.800	-0.0000000460	18.900	-0.0000000377
19.000	-0.0000000305	19.100	-0.0000000244	19.200	-0.0000000194
19.300	-0.0000000154	19.400	-0.0000000123	19.500	-0.0000000098
19.600	-0.0000000078	19.700	-0.0000000059	19.800	-0.0000000043

19.900	-0.0000000028	20.000	-0.0000000017	20.100	-0.0000000009
20.200	-0.0000000004	20.300	-0.0000000002	20.400	0.0000000001
20.500	0.0000000004	20.600	0.0000000008	20.700	0.0000000012
20.800	0.0000000014	20.900	0.0000000015	21.000	0.0000000013
21.100	0.0000000011	21.200	0.0000000010	21.300	0.0000000011
21.400	0.0000000012	21.500	0.0000000014	21.600	0.0000000015
21.700	0.0000000014	21.800	0.0000000011	21.900	0.0000000009
22.000	0.0000000007				

E.3 Potential for the system $^{6}Li +^{58} Ni$

Table E.5: Normalization factors of the real and imaginary potential

E	**E/V$_{bar}$**	**N$_{real}$**	**N$_{imag}$**
9	0.640	0.393	1.079
9.5	0.675	0.362	1.037
10	0.711	0.335	0.995
10.5	0.746	0.313	0.953
11	0.782	0.294	0.911
11.5	0.817	0.280	0.869
12	0.853	0.269	0.821
12.5	0.888	0.264	0.779
13	0.924	0.266	0.737
13.5	0.959	0.275	0.695
14	0.995	0.299	0.653
14.5	1.031	0.334	0.645
15	1.066	0.350	0.643
15.5	1.102	0.360	0.640
16	1.137	0.366	0.638
16.5	1.173	0.371	0.635
17	1.208	0.374	0.633
17.5	1.244	0.375	0.631
18	1.279	0.376	0.629
18.5	1.315	0.375	0.626
19	1.350	0.375	0.623

Table E.6: BDM3Y interaction at $E = 15\ MeV$

R (fm)	**interaction**(MeV)	**R (fm)**	**interaction**(MeV)	**R (fm)**	**interaction**(MeV)
0.100	-268.4209899902	0.200	-268.2319946289	0.300	-267.9164123535
0.400	-267.4735107422	0.500	-266.9023132324	0.600	-266.2013854980
0.700	-265.3692016602	0.800	-264.4039001465	0.900	-263.3034973145
1.000	-262.0657043457	1.100	-260.6882019043	1.200	-259.1683959961
1.300	-257.5038146973	1.400	-255.6918029785	1.500	-253.7295989990
1.600	-251.6148986816	1.700	-249.3450012207	1.800	-246.9176940918
1.900	-244.3307952881	2.000	-241.5823974609	2.100	-238.6710968018
2.200	-235.5955963135	2.300	-232.3551940918	2.400	-228.9494934082
2.500	-225.3787994385	2.600	-221.6439056396	2.700	-217.7463073730
2.800	-213.6880035400	2.900	-209.4720001221	3.000	-205.1018066406
3.100	-200.5816955566	3.200	-195.9169006348	3.300	-191.1134948730
3.400	-186.1784057617	3.500	-181.1190948486	3.600	-175.9443969727
3.700	-170.6634979248	3.800	-165.2866973877	3.900	-159.8251037598

4.000	-154.2902984619	4.100	-148.6949005127	4.200	-143.0520019531
4.300	-137.3755035400	4.400	-131.6797943115	4.500	-125.9794998169
4.600	-120.2900009155	4.700	-114.6268005371	4.800	-109.0054016113
4.900	-103.4417037964	5.000	-97.9510726929	5.100	-92.5489501953
5.200	-87.2502212524	5.300	-82.0692062378	5.400	-77.0195007324
5.500	-72.1137771606	5.600	-67.3636779785	5.700	-62.7796211243
5.800	-58.3707313538	5.900	-54.1446990967	6.000	-50.1077308655
6.100	-46.2645111084	6.200	-42.6181411743	6.300	-39.1702003479
6.400	-35.9207687378	6.500	-32.8684883118	6.600	-30.0107002258
6.700	-27.3435096741	6.800	-24.8619194031	6.900	-22.5600204468
7.000	-20.4311008453	7.100	-18.4678001404	7.200	-16.6622390747
7.300	-15.0062198639	7.400	-13.4912900925	7.500	-12.1088800430
7.600	-10.8504495621	7.700	-9.7075309753	7.800	-8.6718349457
7.900	-7.7353129387	8.000	-6.8902120590	8.100	-6.1291131973
8.200	-5.4449667931	8.300	-4.8311100006	8.400	-4.2812800407
8.500	-3.7896211147	8.600	-3.3506801128	8.700	-2.9594039917
8.800	-2.6111268997	8.900	-2.3015580177	9.000	-2.0267629623
9.100	-1.7831449509	9.200	-1.5674320459	9.300	-1.3766490221
9.400	-1.2081010342	9.500	-1.0593550205	9.600	-0.9282174110
9.700	-0.8127142191	9.800	-0.7110751867	9.900	-0.6217147112
10.000	-0.5432153940	10.100	-0.4743128121	10.200	-0.4138802886
10.300	-0.3609161079	10.400	-0.3145307899	10.500	-0.2739354074
10.600	-0.2384312004	10.700	-0.2074002028	10.800	-0.1802964956
10.900	-0.1566379070	11.000	-0.1359996945	11.100	-0.1180075034
11.200	-0.1023316011	11.300	-0.0886824280	11.400	-0.0768052712
11.500	-0.0664764866	11.600	-0.0574998595	11.700	-0.0497032888
11.800	-0.0429359488	11.900	-0.0370657705	12.000	-0.0319770910
12.100	-0.0275687892	12.200	-0.0237524193	12.300	-0.0204507094
12.400	-0.0175962001	12.500	-0.0151300002	12.600	-0.0130007602
12.700	-0.0111637004	12.800	-0.0095798401	12.900	-0.0082152402
13.000	-0.0070403721	13.100	-0.0060295672	13.200	-0.0051605278
13.300	-0.0044138958	13.400	-0.0037728790	13.500	-0.0032229209
13.600	-0.0027514140	13.700	-0.0023474470	13.800	-0.0020015810
13.900	-0.0017056600	14.000	-0.0014526410	14.100	-0.0012364470
14.200	-0.0010518359	14.300	-0.0008942973	14.400	-0.0007599442
14.500	-0.0006454358	14.600	-0.0005479004	14.700	-0.0004648713
14.800	-0.0003942319	14.900	-0.0003341670	15.000	-0.0002831216
15.100	-0.0002397646	15.200	-0.0002029576	15.300	-0.0001717273
15.400	-0.0001452422	15.500	-0.0001227923	15.600	-0.0001037714
15.700	-0.0000876629	15.800	-0.0000740265	15.900	-0.0000624878
16.000	-0.0000527285	16.100	-0.0000444777	16.200	-0.0000375053
16.300	-0.0000316153	16.400	-0.0000266414	16.500	-0.0000224423
16.600	-0.0000188984	16.700	-0.0000159084	16.800	-0.0000133869
16.900	-0.0000112614	17.000	-0.0000094704	17.100	-0.0000079618
17.200	-0.0000066912	17.300	-0.0000056212	17.400	-0.0000047201

17.500	-0.0000039616	17.600	-0.0000033236	17.700	-0.0000027872
17.800	-0.0000023367	17.900	-0.0000019582	18.000	-0.0000016403
18.100	-0.0000013730	18.200	-0.0000011482	18.300	-0.0000009594
18.400	-0.0000008010	18.500	-0.0000006684	18.600	-0.0000005576
18.700	-0.0000004649	18.800	-0.0000003872	18.900	-0.0000003219
19.000	-0.0000002670	19.100	-0.0000002209	19.200	-0.0000001825
19.300	-0.0000001507	19.400	-0.0000001244	19.500	-0.0000001026
19.600	-0.0000000844	19.700	-0.0000000690	19.800	-0.0000000559
19.900	-0.0000000450	20.000	-0.0000000360	20.100	-0.0000000288
20.200	-0.0000000231	20.300	-0.0000000185	20.400	-0.0000000146
20.500	-0.0000000112	20.600	-0.0000000082	20.700	-0.0000000057
20.800	-0.0000000038	20.900	-0.0000000024	21.000	-0.0000000015
21.100	-0.0000000009	21.200	-0.0000000003	21.300	0.0000000003
21.400	0.0000000010	21.500	0.0000000016	21.600	0.0000000020
21.700	0.0000000020	21.800	0.0000000019	21.900	0.0000000017
22.000	0.0000000016				

E.4 Potential for the system $^{7}Li +^{58} Ni$

Table E.7: Normalization factors of the real and imaginary potential

E	**E/V$_{bar}$**	**N$_{real}$**	**N$_{imag}$**
9	0.636	0.4	0.201
9.5	0.672	0.4	0.241
10	0.707	0.4	0.280
10.5	0.743	0.4	0.325
11	0.778	0.4	0.365
11.5	0.813	0.4	0.404
12	0.849	0.4	0.443
12.5	0.884	0.4	0.483
13	0.919	0.4	0.5
13.5	0.955	0.4	0.5
14	0.990	0.4	0.5
14.5	1.025	0.4	0.5
15	1.061	0.4	0.5
15.5	1.096	0.4	0.5
16	1.132	0.4	0.5
16.5	1.167	0.4	0.5
17	1.202	0.4	0.5
17.5	1.238	0.4	0.5
18	1.273	0.4	0.5
18.5	1.308	0.4	0.5
19	1.344	0.4	0.5

Table E.8: BDM3Y interaction at $E = 16\ MeV$

R (fm)	**interaction**(MeV)	**R (fm)**	**interaction**(MeV)	**R (fm)**	**interaction**(MeV)
0.100	-315.6296081543	0.200	-315.3959960938	0.300	-315.0062866211
0.400	-314.4595031738	0.500	-313.7546997070	0.600	-312.8905029297
0.700	-311.8652038574	0.800	-310.6770935059	0.900	-309.3240051270
1.000	-307.8037109375	1.100	-306.1138000488	1.200	-304.2517089844
1.300	-302.2149047852	1.400	-300.0008850098	1.500	-297.6069946289
1.600	-295.0307922363	1.700	-292.2699890137	1.800	-289.3226928711
1.900	-286.1868896484	2.000	-282.8613891602	2.100	-279.3450927734
2.200	-275.6375122070	2.300	-271.7387084961	2.400	-267.6494140625
2.500	-263.3707885742	2.600	-258.9049072266	2.700	-254.2545013428
2.800	-249.4232025146	2.900	-244.4154052734	3.000	-239.2362976074
3.100	-233.8919982910	3.200	-228.3894042969	3.300	-222.7362976074
3.400	-216.9411926270	3.500	-211.0137939453	3.600	-204.9640045166
3.700	-198.8031005859	3.800	-192.5426940918	3.900	-186.1954040527

4.000	-179.7743072510	4.100	-173.2931976318	4.200	-166.7664947510
4.300	-160.2089996338	4.400	-153.6361999512	4.500	-147.0635986328
4.600	-140.5072937012	4.700	-133.9835968018	4.800	-127.5087966919
4.900	-121.0992965698	5.000	-114.7713012695	5.100	-108.5409011841
5.200	-102.4238967896	5.300	-96.4354476929	5.400	-90.5901794434
5.500	-84.9019622803	5.600	-79.3837432861	5.700	-74.0473937988
5.800	-68.9036102295	5.900	-63.9617691040	6.000	-59.2298011780
6.100	-54.7140808105	6.200	-50.4194107056	6.300	-46.3489608765
6.400	-42.5042190552	6.500	-38.8850708008	6.600	-35.4898109436
6.700	-32.3152694702	6.800	-29.3568992615	6.900	-26.6089191437
7.000	-24.0644798279	7.100	-21.7158107758	7.200	-19.5544109344
7.300	-17.5712108612	7.400	-15.7567396164	7.500	-14.1012496948
7.600	-12.5949001312	7.700	-11.2278604507	7.800	-9.9904117584
7.900	-8.8730487823	8.000	-7.8665518761	8.100	-6.9620490074
8.200	-6.1510591507	8.300	-5.4255290031	8.400	-4.7778568268
8.500	-4.2009029388	8.600	-3.6879959106	8.700	-3.2329308987
8.800	-2.8299639225	8.900	-2.4737980366	9.000	-2.1595690250
9.100	-1.8828259706	9.200	-1.6395089626	9.300	-1.4259330034
9.400	-1.2387590408	9.500	-1.0749720335	9.600	-0.9318603277
9.700	-0.8069903255	9.800	-0.6981835961	9.900	-0.6034963727
10.000	-0.5211985111	10.100	-0.4497534037	10.200	-0.3877997100
10.300	-0.3341343105	10.400	-0.2876959145	10.500	-0.2475502044
10.600	-0.2128763944	10.700	-0.1829549968	10.800	-0.1571556926
10.900	-0.1349280030	11.000	-0.1157914996	11.100	-0.0993276015
11.200	-0.0851722434	11.300	-0.0730090588	11.400	-0.0625635609
11.500	-0.0535978787	11.600	-0.0459060818	11.700	-0.0393101312
11.800	-0.0336562097	11.900	-0.0288115907	12.000	-0.0246618297
12.100	-0.0211083498	12.200	-0.0180662796	12.300	-0.0154626397
12.400	-0.0132346898	12.500	-0.0113285296	12.600	-0.0096979085
12.700	-0.0083031403	12.800	-0.0071101920	12.900	-0.0060899020
13.000	-0.0052172849	13.100	-0.0044709472	13.200	-0.0038325749
13.300	-0.0032864979	13.400	-0.0028193130	13.500	-0.0024195570
13.600	-0.0020774330	13.700	-0.0017845650	13.800	-0.0015337979
13.900	-0.0013190140	14.000	-0.0011349890	14.100	-0.0009772592
14.200	-0.0008420116	14.300	-0.0007259902	14.400	-0.0006264145
14.500	-0.0005409103	14.600	-0.0004674489	14.700	-0.0004042972
14.800	-0.0003499737	14.900	-0.0003032125	15.000	-0.0002629321
15.100	-0.0002282087	15.200	-0.0001982530	15.300	-0.0001723901
15.400	-0.0001500426	15.500	-0.0001307159	15.600	-0.0001139860
15.700	-0.0000994900	15.800	-0.0000869171	15.900	-0.0000760014
16.000	-0.0000665156	16.100	-0.0000582645	16.200	-0.0000510804
16.300	-0.0000448187	16.400	-0.0000393548	16.500	-0.0000345815
16.600	-0.0000304068	16.700	-0.0000267519	16.800	-0.0000235493
16.900	-0.0000207408	17.000	-0.0000182757	17.100	-0.0000161098
17.200	-0.0000142047	17.300	-0.0000125270	17.400	-0.0000110481

17.500	-0.0000097437	17.600	-0.0000085927	17.700	-0.0000075771
17.800	-0.0000066806	17.900	-0.0000058887	18.000	-0.0000051886
18.100	-0.0000045689	18.200	-0.0000040203	18.300	-0.0000035347
18.400	-0.0000031054	18.500	-0.0000027264	18.600	-0.0000023920
18.700	-0.0000020969	18.800	-0.0000018362	18.900	-0.0000016058
19.000	-0.0000014021	19.100	-0.0000012224	19.200	-0.0000010645
19.300	-0.0000009263	19.400	-0.0000008054	19.500	-0.0000006997
19.600	-0.0000006070	19.700	-0.0000005254	19.800	-0.0000004536
19.900	-0.0000003908	20.000	-0.0000003363	20.100	-0.0000002894
20.200	-0.0000002491	20.300	-0.0000002143	20.400	-0.0000001839
20.500	-0.0000001572	20.600	-0.0000001337	20.700	-0.0000001133
20.800	-0.0000000960	20.900	-0.0000000816	21.000	-0.0000000696
21.100	-0.0000000594	21.200	-0.0000000505	21.300	-0.0000000425
21.400	-0.0000000352	21.500	-0.0000000290	21.600	-0.0000000239
21.700	-0.0000000200	21.800	-0.0000000171	21.900	-0.0000000147
22.000	-0.0000000124				

E.5 Potential for the system $^{6}Li +^{120} Sn$

Table E.9: Normalization factors of the real and imaginary potential

E	**E/V$_{bar}$**	**N$_{real}$**	**N$_{imag}$**
12	0.562	1.072	0.859
12.5	0.585	1.032	0.898
13	0.608	0.984	0.936
13.5	0.632	0.936	0.967
14	0.655	0.844	0.992
14.5	0.679	0.772	0.967
15	0.702	0.729	0.947
15.5	0.725	0.685	0.922
16	0.749	0.648	0.897
16.5	0.772	0.623	0.877
17	0.796	0.595	0.852
17.5	0.819	0.571	0.827
18	0.842	0.555	0.807
18.5	0.866	0.538	0.782
19	0.889	0.524	0.757
19.5	0.912	0.515	0.737
20	0.936	0.508	0.712
20.5	0.959	0.504	0.687
21	0.983	0.508	0.662
21.5	1.006	0.522	0.647
22	1.029	0.531	0.645
22.5	1.053	0.534	0.643
23	1.076	0.534	0.642
23.5	1.100	0.533	0.640
24	1.123	0.531	0.639
24.5	1.146	0.529	0.637
25	1.170	0.526	0.635
25.5	1.193	0.523	0.634
26	1.219	0.519	0.632

Table E.10: BDM3Y interaction at $E = 20\ MeV$

R (fm)	**interaction**(MeV)	**R (fm)**	**interaction**(MeV)	**R (fm)**	**interaction**(MeV)
0.100	-296.6950073242	0.200	-296.6202087402	0.300	-296.4949951172
0.400	-296.3186950684	0.500	-296.0900878906	0.600	-295.8078918457
0.700	-295.4703979492	0.800	-295.0755920410	0.900	-294.6210937500
1.000	-294.1044006348	1.100	-293.5227050781	1.200	-292.8727111816
1.300	-292.1512145996	1.400	-291.3544921875	1.500	-290.4786071777
1.600	-289.5195007324	1.700	-288.4729003906	1.800	-287.3341979980
1.900	-286.0989074707	2.000	-284.7622070312	2.100	-283.3190917969
2.200	-281.7648010254	2.300	-280.0940856934	2.400	-278.3020019531
2.500	-276.3836059570	2.600	-274.3338928223	2.700	-272.1480102539
2.800	-269.8212890625	2.900	-267.3493041992	3.000	-264.7276916504
3.100	-261.9526977539	3.200	-259.0205078125	3.300	-255.9281005859
3.400	-252.6726989746	3.500	-249.2521057129	3.600	-245.6645965576
3.700	-241.9091949463	3.800	-237.9855957031	3.900	-233.8941955566
4.000	-229.6360015869	4.100	-225.2129974365	4.200	-220.6280059814
4.300	-215.8845977783	4.400	-210.9873962402	4.500	-205.9418945312
4.600	-200.7543945312	4.700	-195.4322967529	4.800	-189.9839935303
4.900	-184.4185943604	5.000	-178.7463989258	5.100	-172.9783935547
5.200	-167.1266021729	5.300	-161.2037963867	5.400	-155.2236022949
5.500	-149.2003021240	5.600	-143.1488952637	5.700	-137.0848999023
5.800	-131.0245056152	5.900	-124.9840011597	6.000	-118.9800033569
6.100	-113.0294036865	6.200	-107.1489028931	6.300	-101.3548965454
6.400	-95.6637115479	6.500	-90.0908584595	6.600	-84.6512374878
6.700	-79.3588180542	6.800	-74.2265090942	6.900	-69.2659683228
7.000	-64.4875183105	7.100	-59.9000015259	7.200	-55.5106811523
7.300	-51.3251991272	7.400	-47.3475608826	7.500	-43.5801086426
7.600	-40.0235710144	7.700	-36.6771583557	7.800	-33.5386009216
7.900	-30.6043090820	8.000	-27.8694801331	8.100	-25.3282604218
8.200	-22.9738903046	8.300	-20.7988605499	8.400	-18.7950897217
8.500	-16.9540405273	8.600	-15.2668695450	8.700	-13.7245903015
8.800	-12.3181495667	8.900	-11.0385599136	9.000	-9.8769769669
9.100	-8.8247728348	9.200	-7.8736100197	9.300	-7.0154838562
9.400	-6.2427601814	9.500	-5.5482029915	9.600	-4.9249911308
9.700	-4.3667278290	9.800	-3.8674418926	9.900	-3.4215829372
10.000	-3.0240170956	10.100	-2.6700060368	10.200	-2.3552000523
10.300	-2.0756130219	10.400	-1.8276070356	10.500	-1.6078699827
10.600	-1.4133969545	10.700	-1.2414629459	10.800	-1.0896110535
10.900	-0.9556248784	11.000	-0.8375110030	11.100	-0.7334814072
11.200	-0.6419342160	11.300	-0.5614368916	11.400	-0.4907110929
11.500	-0.4286175966	11.600	-0.3741422892	11.700	-0.3263845146
11.800	-0.2845444977	11.900	-0.2479137033	12.000	-0.2158645988
12.100	-0.1878423989	12.200	-0.1633566022	12.300	-0.1419744939
12.400	-0.1233145967	12.500	-0.1070403010	12.600	-0.0928556919
12.700	-0.0805001110	12.800	-0.0697445124	12.900	-0.0603876412

13.000	-0.0522527695	13.100	-0.0451848395	13.200	-0.0390478782
13.300	-0.0337227508	13.400	-0.0291050691	13.500	-0.0251035094
13.600	-0.0216381699	13.700	-0.0186391901	13.800	-0.0160455704
13.900	-0.0138040204	14.000	-0.0118680596	14.100	-0.0101971701
14.200	-0.0087560359	14.300	-0.0075139022	14.400	-0.0064440141
14.500	-0.0055231079	14.600	-0.0047309678	14.700	-0.0040500420
14.800	-0.0034651021	14.900	-0.0029629469	15.000	-0.0025321390
15.100	-0.0021627760	15.200	-0.0018462930	15.300	-0.0015752880
15.400	-0.0013433660	15.500	-0.0011450100	15.600	-0.0009754605
15.700	-0.0008306182	15.800	-0.0007069523	15.900	-0.0006014244
16.000	-0.0005114223	16.100	-0.0004347013	16.200	-0.0003693347
16.300	-0.0003136695	16.400	-0.0002662887	16.500	-0.0002259785
16.600	-0.0001916994	16.700	-0.0001625617	16.800	-0.0001378045
16.900	-0.0001167777	17.000	-0.0000989260	17.100	-0.0000837759
17.200	-0.0000709235	17.300	-0.0000600245	17.400	-0.0000507853
17.500	-0.0000429557	17.600	-0.0000363226	17.700	-0.0000307047
17.800	-0.0000259480	17.900	-0.0000219217	18.000	-0.0000185148
18.100	-0.0000156331	18.200	-0.0000131963	18.300	-0.0000111363
18.400	-0.0000093951	18.500	-0.0000079235	18.600	-0.0000066800
18.700	-0.0000056296	18.800	-0.0000047428	18.900	-0.0000039944
19.000	-0.0000033630	19.100	-0.0000028305	19.200	-0.0000023813
19.300	-0.0000020022	19.400	-0.0000016824	19.500	-0.0000014128
19.600	-0.0000011858	19.700	-0.0000009947	19.800	-0.0000008341
19.900	-0.0000006990	20.000	-0.0000005853	20.100	-0.0000004895
20.200	-0.0000004087	20.300	-0.0000003407	20.400	-0.0000002838
20.500	-0.0000002362	20.600	-0.0000001964	20.700	-0.0000001632
20.800	-0.0000001352	20.900	-0.0000001116	21.000	-0.0000000917
21.100	-0.0000000751	21.200	-0.0000000613	21.300	-0.0000000499
21.400	-0.0000000407	21.500	-0.0000000331	21.600	-0.0000000266
21.700	-0.0000000211	21.800	-0.0000000164	21.900	-0.0000000124
22.000	-0.0000000093				

E.6 Potential for the system $^{7}Li + ^{120}Sn$

Table E.11: Normalization factors of the real and imaginary potential

E	**E/V$_{bar}$**	**N$_{real}$**	**N$_{imag}$**
12	0.563	0.5	0.5
12.5	0.586	0.5	0.5
13	0.609	0.5	0.5
13.5	0.633	0.5	0.5
14	0.656	0.5	0.5
14.5	0.680	0.5	0.5
15	0.703	0.5	0.5
15.5	0.727	0.5	0.5
16	0.750	0.5	0.5
16.5	0.774	0.5	0.5
17	0.797	0.5	0.5
17.5	0.820	0.5	0.5
18	0.844	0.5	0.5
18.5	0.867	0.5	0.5
19	0.891	0.5	0.5
19.5	0.914	0.5	0.5
20	0.938	0.5	0.5
20.5	0.961	0.5	0.5
21	0.985	0.5	0.5
21.5	1.008	0.5	0.5
22	1.031	0.5	0.5
22.5	1.055	0.5	0.5
23	1.078	0.5	0.5
23.5	1.102	0.5	0.5
24	1.125	0.5	0.5
24.5	1.149	0.5	0.5
25	1.172	0.5	0.5
25.5	1.195	0.5	0.5
26	1.220	0.5	0.5

Table E.12: BDM3Y interaction at $E = 19\ MeV$

R (fm)	**interaction**(MeV)	**R (fm)**	**interaction**(MeV)	**R (fm)**	**interaction**(MeV)
0.100	-348.9292907715	0.200	-348.8398132324	0.300	-348.6900024414
0.400	-348.4787902832	0.500	-348.2049865723	0.600	-347.8666076660
0.700	-347.4616088867	0.800	-346.9873046875	0.900	-346.4411010742
1.000	-345.8194885254	1.100	-345.1189880371	1.200	-344.3356933594
1.300	-343.4655151367	1.400	-342.5038146973	1.500	-341.4458923340
1.600	-340.2867126465	1.700	-339.0213012695	1.800	-337.6440124512
1.900	-336.1495056152	2.000	-334.5320129395	2.100	-332.7858886719
2.200	-330.9052124023	2.300	-328.8843078613	2.400	-326.7174072266
2.500	-324.3985900879	2.600	-321.9226074219	2.700	-319.2838134766
2.800	-316.4771118164	2.900	-313.4978027344	3.000	-310.3411865234
3.100	-307.0032958984	3.200	-303.4805908203	3.300	-299.7699890137
3.400	-295.8689880371	3.500	-291.7759094238	3.600	-287.4896850586
3.700	-283.0101013184	3.800	-278.3375854492	3.900	-273.4736938477
4.000	-268.4205932617	4.100	-263.1816101074	4.200	-257.7608032227
4.300	-252.1634063721	4.400	-246.3954010010	4.500	-240.4640960693
4.600	-234.3773040771	4.700	-228.1441955566	4.800	-221.7747955322
4.900	-215.2799072266	5.000	-208.6712951660	5.100	-201.9617004395
5.200	-195.1645050049	5.300	-188.2940063477	5.400	-181.3650054932
5.500	-174.3930969238	5.600	-167.3946075439	5.700	-160.3860015869
5.800	-153.3843994141	5.900	-146.4073028564	6.000	-139.4721984863
6.100	-132.5968017578	6.200	-125.7990036011	6.300	-119.0960998535
6.400	-112.5055007935	6.500	-106.0438995361	6.600	-99.7276306152
6.700	-93.5720672607	6.800	-87.5917282104	6.900	-81.8000335693
7.000	-76.2091293335	7.100	-70.8298034668	7.200	-65.6712799072
7.300	-60.7411689758	7.400	-56.0453681946	7.500	-51.5879898071
7.600	-47.3713684082	7.700	-43.3960609436	7.800	-39.6609191895
7.900	-36.1631507874	8.000	-32.8984489441	8.100	-29.8611602783
8.200	-27.0443992615	8.300	-24.4402408600	8.400	-22.0399208069
8.500	-19.8339900970	8.600	-17.8125095367	8.700	-15.9652204514
8.800	-14.2816600800	8.900	-12.7513599396	9.000	-11.3639001846
9.100	-10.1090602875	9.200	-8.9769086838	9.300	-7.9578270912
9.400	-7.0426077843	9.500	-6.2224822044	9.600	-5.4891448021
9.700	-4.8347778320	9.800	-4.2520608902	9.900	-3.7336559296
10.000	-3.2736260891	10.100	-2.8665349483	10.200	-2.5068960190
10.300	-2.1896970272	10.400	-1.9103770256	10.500	-1.6647900343
10.600	-1.4491859674	10.700	-1.2601790428	10.800	-1.0947179794
10.900	-0.9500651956	11.000	-0.8237668276	11.100	-0.7136309743
11.200	-0.6177036762	11.300	-0.5342469811	11.400	-0.4617187083
11.500	-0.3987531960	11.600	-0.3441435993	11.700	-0.2968255877
11.800	-0.2558620870	11.900	-0.2204297930	12.000	-0.1897902936
12.100	-0.1633313000	12.200	-0.1404989064	12.300	-0.1208090037
12.400	-0.1038398966	12.500	-0.0892242566	12.600	-0.0766425207
12.700	-0.0658171922	12.800	-0.0565074906	12.900	-0.0485047102

13.000	-0.0416281410	13.100	-0.0357214585	13.200	-0.0306495503
13.300	-0.0262957606	13.400	-0.0225593895	13.500	-0.0193536505
13.600	-0.0166037306	13.700	-0.0142452205	13.800	-0.0122227101
13.900	-0.0104884999	14.000	-0.0090016341	14.100	-0.0077268891
14.200	-0.0066340282	14.300	-0.0056970888	14.400	-0.0048937942
14.500	-0.0042050309	14.600	-0.0036144101	14.700	-0.0031078809
14.800	-0.0026734001	14.900	-0.0023006490	15.000	-0.0019807860
15.100	-0.0017062380	15.200	-0.0014705150	15.300	-0.0012680630
15.400	-0.0010941240	15.500	-0.0009446242	15.600	-0.0008160775
15.700	-0.0007054978	15.800	-0.0006103284	15.900	-0.0005283793
16.000	-0.0004577748	16.100	-0.0003969086	16.200	-0.0003444047
16.300	-0.0002990850	16.400	-0.0002599403	16.500	-0.0002261059
16.600	-0.0001968399	16.700	-0.0001715059	16.800	-0.0001495579
16.900	-0.0001305270	17.000	-0.0001140113	17.100	-0.0000996661
17.200	-0.0000871954	17.300	-0.0000763450	17.400	-0.0000668958
17.500	-0.0000586592	17.600	-0.0000514723	17.700	-0.0000451951
17.800	-0.0000397071	17.900	-0.0000349047	18.000	-0.0000306988
18.100	-0.0000270124	18.200	-0.0000237786	18.300	-0.0000209393
18.400	-0.0000184438	18.500	-0.0000162484	18.600	-0.0000143155
18.700	-0.0000126127	18.800	-0.0000111120	18.900	-0.0000097891
19.000	-0.0000086225	19.100	-0.0000075929	19.200	-0.0000066837
19.300	-0.0000058803	19.400	-0.0000051702	19.500	-0.0000045428
19.600	-0.0000039888	19.700	-0.0000035001	19.800	-0.0000030691
19.900	-0.0000026889	20.000	-0.0000023535	20.100	-0.0000020574
20.200	-0.0000017962	20.300	-0.0000015663	20.400	-0.0000013643
20.500	-0.0000011874	20.600	-0.0000010325	20.700	-0.0000008969
20.800	-0.0000007780	20.900	-0.0000006736	21.000	-0.0000005821
21.100	-0.0000005022	21.200	-0.0000004328	21.300	-0.0000003728
21.400	-0.0000003210	21.500	-0.0000002761	21.600	-0.0000002370
21.700	-0.0000002028	21.800	-0.0000001729	21.900	-0.0000001471
22.000	-0.0000001251				

E.7 Potential for the system $^{6}Li + ^{208}Pb$

Table E.13: Normalization factors of the real and imaginary potential

E	**E/V$_{bar}$**	**N$_{real}$**	**N$_{imag}$**
20	0.641	0.852	1.386
20.5	0.657	0.828	1.368
21	0.673	0.798	1.343
21.5	0.689	0.776	1.325
22	0.705	0.756	1.306
22.5	0.721	0.737	1.288
23	0.737	0.719	1.270
23.5	0.753	0.697	1.245
24	0.769	0.681	1.227
24.5	0.785	0.666	1.208
25	0.801	0.652	1.190
25.5	0.817	0.639	1.171
26	0.833	0.623	1.147
26.5	0.849	0.613	1.128
27	0.865	0.603	1.11
27.5	0.881	0.593	1.091
28	0.897	0.585	1.073
28.5	0.913	0.576	1.048
29	0.929	0.570	1.030
29.5	0.945	0.565	1.012
30	0.961	0.561	0.993
30.5	0.977	0.558	0.975
31	0.993	0.556	0.950
31.5	1.009	0.556	0.932
32	1.025	0.557	0.913
32.5	1.041	0.560	0.895
33	1.057	0.566	0.876
33.5	1.073	0.580	0.852
34	1.089	0.600	0.849
34.5	1.105	0.610	0.848
35	1.121	0.617	0.847
35.5	1.137	0.623	0.846
36	1.153	0.628	0.845

Table E.14: BDM3Y interaction at $E = 25\ MeV$

R (fm)	**interaction**(MeV)	**R (fm)**	**interaction**(MeV)	**R (fm)**	**interaction**(MeV)
0.100	-300.4150085449	0.200	-300.3945922852	0.300	-300.3605041504
0.400	-300.3122863770	0.500	-300.2496948242	0.600	-300.1720886230
0.700	-300.0787963867	0.800	-299.9690856934	0.900	-299.8421020508
1.000	-299.6965942383	1.100	-299.5314941406	1.200	-299.3453979492
1.300	-299.1368103027	1.400	-298.9039001465	1.500	-298.6448974609
1.600	-298.3576965332	1.700	-298.0401000977	1.800	-297.6893920898
1.900	-297.3031005859	2.000	-296.8782043457	2.100	-296.4117126465
2.200	-295.9000854492	2.300	-295.3398132324	2.400	-294.7269897461
2.500	-294.0577087402	2.600	-293.3275146484	2.700	-292.5320129395
2.800	-291.6664123535	2.900	-290.7257995605	3.000	-289.7049865723
3.100	-288.5987854004	3.200	-287.4014892578	3.300	-286.1076965332
3.400	-284.7116088867	3.500	-283.2073974609	3.600	-281.5892028809
3.700	-279.8511962891	3.800	-277.9873962402	3.900	-275.9920959473
4.000	-273.8595886230	4.100	-271.5844116211	4.200	-269.1611022949
4.300	-266.5848083496	4.400	-263.8505859375	4.500	-260.9541931152
4.600	-257.8918151855	4.700	-254.6598968506	4.800	-251.2557067871
4.900	-247.6768951416	5.000	-243.9221038818	5.100	-239.9904937744
5.200	-235.8820037842	5.300	-231.5975036621	5.400	-227.1387939453
5.500	-222.5084991455	5.600	-217.7102966309	5.700	-212.7487945557
5.800	-207.6298065186	5.900	-202.3598022461	6.000	-196.9465942383
6.100	-191.3990936279	6.200	-185.7270965576	6.300	-179.9414062500
6.400	-174.0538024902	6.500	-168.0771026611	6.600	-162.0251007080
6.700	-155.9120941162	6.800	-149.7536926270	6.900	-143.5657958984
7.000	-137.3648986816	7.100	-131.1683959961	7.200	-124.9936981201
7.300	-118.8585968018	7.400	-112.7808990479	7.500	-106.7785034180
7.600	-100.8687973022	7.700	-95.0690307617	7.800	-89.3955383301
7.900	-83.8639984131	8.000	-78.4889831543	8.100	-73.2838973999
8.200	-68.2607727051	8.300	-63.4301109314	8.400	-58.8007812500
8.500	-54.3799514771	8.600	-50.1730003357	8.700	-46.1835289001
8.800	-42.4133605957	8.900	-38.8626213074	9.000	-35.5297584534
9.100	-32.4117698669	9.200	-29.5042190552	9.300	-26.8014698029
9.400	-24.2968101501	9.500	-21.9826698303	9.600	-19.8507308960
9.700	-17.8921604156	9.800	-16.0977191925	9.900	-14.4579496384
10.000	-12.9632797241	10.100	-11.6041698456	10.200	-10.3697700500
10.300	-9.2447624207	10.400	-8.2310237885	10.500	-7.3191151619
10.600	-6.5001797676	10.700	-5.7659401894	10.800	-5.1086788177
10.900	-4.5212321281	11.000	-3.9969680309	11.100	-3.5297670364
11.200	-3.1139979362	11.300	-2.7444980145	11.400	-2.4165420532
11.500	-2.1258230209	11.600	-1.8684220314	11.700	-1.6407819986
11.800	-1.4396840334	11.900	-1.2622209787	12.000	-1.1057729721
12.100	-0.9679852724	12.200	-0.8467447162	12.300	-0.7401587963
12.400	-0.6465359926	12.500	-0.5643671155	12.600	-0.4923076928
12.700	-0.4291619062	12.800	-0.3738679886	12.900	-0.3254843056

13.000	-0.2831766009	13.100	-0.2462072968	13.200	-0.2139243037
13.300	-0.1857521981	13.400	-0.1611838043	13.500	-0.1397719979
13.600	-0.1211232990	13.700	-0.1048919037	13.800	-0.0907737091
13.900	-0.0785016492	14.000	-0.0678414777	14.100	-0.0585877188
14.200	-0.0505603217	14.300	-0.0436015800	14.400	-0.0375734605
14.500	-0.0323552303	14.600	-0.0278409906	14.700	-0.0239361897
14.800	-0.0205639694	14.900	-0.0176538508	15.000	-0.0151443901
15.100	-0.0129820602	15.200	-0.0111202803	15.300	-0.0095184958
15.400	-0.0081414683	15.500	-0.0069585769	15.600	-0.0059432429
15.700	-0.0050724060	15.800	-0.0043260818	15.900	-0.0036869640
16.000	-0.0031400730	16.100	-0.0026724611	16.200	-0.0022729391
16.300	-0.0019318520	16.400	-0.0016408680	16.500	-0.0013928120
16.600	-0.0011815029	16.700	-0.0010016280	16.800	-0.0008486180
16.900	-0.0007185525	17.000	-0.0006080664	17.100	-0.0005142753
17.200	-0.0004347084	17.300	-0.0003672511	17.400	-0.0003100960
17.500	-0.0002616992	17.600	-0.0002207433	17.700	-0.0001861050
17.800	-0.0001568267	17.900	-0.0001320926	18.000	-0.0001112083
18.100	-0.0000935833	18.200	-0.0000787162	18.300	-0.0000661816
18.400	-0.0000556190	18.500	-0.0000467226	18.600	-0.0000392333
18.700	-0.0000329313	18.800	-0.0000276303	18.900	-0.0000231727
19.000	-0.0000194257	19.100	-0.0000162773	19.200	-0.0000136332
19.300	-0.0000114139	19.400	-0.0000095521	19.500	-0.0000079906
19.600	-0.0000066812	19.700	-0.0000055833	19.800	-0.0000046629
19.900	-0.0000038917	20.000	-0.0000032460	20.100	-0.0000027059
20.200	-0.0000022546	20.300	-0.0000018774	20.400	-0.0000015621
20.500	-0.0000012983	20.600	-0.0000010775	20.700	-0.0000008930
20.800	-0.0000007392	20.900	-0.0000006113	21.000	-0.0000005052
21.100	-0.0000004170	21.200	-0.0000003435	21.300	-0.0000002821
21.400	-0.0000002306	21.500	-0.0000001878	21.600	-0.0000001524
21.700	-0.0000001235	21.800	-0.0000000999	21.900	-0.0000000806
22.000	-0.0000000645				

E.8 Potential for the system $^{7}Li + ^{208}Pb$

Table E.15: Normalization factors of the real and imaginary potential

E	**E/V$_{bar}$**	**N$_{real}$**	**N$_{imag}$**
20	0.643	0.75	0.280
20.5	0.659	0.75	0.291
21	0.675	0.75	0.300
21.5	0.691	0.75	0.315
22	0.707	0.75	0.330
22.5	0.723	0.75	0.348
23	0.740	0.75	0.363
23.5	0.756	0.75	0.380
24	0.772	0.75	0.39
24.5	0.788	0.75	0.408
25	0.804	0.75	0.419
25.5	0.820	0.75	0.435
26	0.836	0.75	0.449
26.5	0.852	0.75	0.462
27	0.868	0.75	0.480
27.5	0.884	0.75	0.493
28	0.900	0.75	0.498
28.5	0.916	0.75	0.498
29	0.932	0.75	0.498
29.5	0.949	0.75	0.498
30	0.965	0.75	0.498
30.5	0.981	0.75	0.498
31	0.997	0.75	0.498
31.5	1.013	0.75	0.498
32	1.029	0.75	0.498
32.5	1.045	0.75	0.498
33	1.061	0.75	0.498
33.5	1.077	0.75	0.498
34	1.093	0.75	0.498
34.5	1.109	0.75	0.498
35	1.125	0.75	0.498
35.5	1.141	0.75	0.498
36	1.158	0.75	0.498

Table E.16: BDM3Y interaction at $E = 31\ MeV$

R (fm)	**interaction**(MeV)	**R (fm)**	**interaction**(MeV)	**R (fm)**	**interaction**(MeV)
0.100	-430.9419860840	0.200	-430.9096069336	0.300	-430.8551940918
0.400	-430.7784118652	0.500	-430.6783142090	0.600	-430.5541992188
0.700	-430.4049072266	0.800	-430.2290039062	0.900	-430.0249023438
1.000	-429.7907104492	1.100	-429.5244140625	1.200	-429.2236022949
1.300	-428.8857116699	1.400	-428.5076904297	1.500	-428.0863952637
1.600	-427.6181945801	1.700	-427.0993957520	1.800	-426.5255126953
1.900	-425.8922119141	2.000	-425.1944885254	2.100	-424.4270935059
2.200	-423.5844116211	2.300	-422.6604919434	2.400	-421.6489868164
2.500	-420.5432128906	2.600	-419.3362121582	2.700	-418.0206909180
2.800	-416.5889892578	2.900	-415.0332946777	3.000	-413.3456115723
3.100	-411.5174865723	3.200	-409.5405883789	3.300	-407.4064941406
3.400	-405.1065063477	3.500	-402.6319885254	3.600	-399.9746093750
3.700	-397.1258850098	3.800	-394.0776062012	3.900	-390.8216857910
4.000	-387.3507080078	4.100	-383.6572875977	4.200	-379.7344970703
4.300	-375.5762023926	4.400	-371.1766052246	4.500	-366.5307922363
4.600	-361.6343078613	4.700	-356.4837951660	4.800	-351.0766906738
4.900	-345.4114074707	5.000	-339.4873962402	5.100	-333.3053894043
5.200	-326.8673095703	5.300	-320.1762084961	5.400	-313.2367858887
5.500	-306.0549926758	5.600	-298.6384887695	5.700	-290.9963989258
5.800	-283.1391906738	5.900	-275.0793151855	6.000	-266.8308105469
6.100	-258.4092102051	6.200	-249.8316955566	6.300	-241.1174011230
6.400	-232.2864990234	6.500	-223.3609008789	6.600	-214.3639068604
6.700	-205.3200073242	6.800	-196.2546997070	6.900	-187.1945037842
7.000	-178.1665039062	7.100	-169.1981964111	7.200	-160.3173980713
7.300	-151.5516967773	7.400	-142.9281005859	7.500	-134.4732055664
7.600	-126.2120971680	7.700	-118.1688003540	7.800	-110.3654022217
7.900	-102.8220977783	8.000	-95.5565719604	8.100	-88.5842895508
8.200	-81.9178771973	8.300	-75.5672302246	8.400	-69.5393981934
8.500	-63.8386116028	8.600	-58.4663085938	8.700	-53.4213485718
8.800	-48.7000885010	8.900	-44.2966308594	9.000	-40.2030906677
9.100	-36.4098281860	9.200	-32.9057502747	9.300	-29.6785507202
9.400	-26.7150402069	9.500	-24.0013504028	9.600	-21.5232105255
9.700	-19.2661209106	9.800	-17.2155990601	9.900	-15.3573198318
10.000	-13.6772298813	10.100	-12.1617202759	10.200	-10.7976799011
10.300	-9.5725536346	10.400	-8.4744567871	10.500	-7.4921460152
10.600	-6.6150741577	10.700	-5.8333888054	10.800	-5.1379342079
10.900	-4.5202322006	11.000	-3.9724709988	11.100	-3.4874789715
11.200	-3.0586929321	11.300	-2.6801319122	11.400	-2.3463590145
11.500	-2.0524508953	11.600	-1.7939590216	11.700	-1.5668770075
11.800	-1.3676029444	11.900	-1.1929130554	12.000	-1.0399219990
12.100	-0.9060559273	12.200	-0.7890242934	12.300	-0.6867918968
12.400	-0.5975537896	12.500	-0.5197125077	12.600	-0.4518561065
12.700	-0.3927389979	12.800	-0.3412638903	12.900	-0.2964653075

13.000	-0.2574951947	13.100	-0.2236092985	13.200	-0.1941553056
13.300	-0.1685620993	13.400	-0.1463302970	13.500	-0.1270233989
13.600	-0.1102603003	13.700	-0.0957086310	13.800	-0.0830787271
13.900	-0.0721181929	14.000	-0.0626073107	14.100	-0.0543549284
14.200	-0.0471948385	14.300	-0.0409826003	14.400	-0.0355927013
14.500	-0.0309161600	14.600	-0.0268583708	14.700	-0.0233372208
14.800	-0.0202814601	14.900	-0.0176292993	15.000	-0.0153271398
15.100	-0.0133285196	15.200	-0.0115931397	15.300	-0.0100860801
15.400	-0.0087770531	15.500	-0.0076398239	15.600	-0.0066516371
15.700	-0.0057927701	15.800	-0.0050461269	15.900	-0.0043968922
16.000	-0.0038322201	16.100	-0.0033409731	16.200	-0.0029134969
16.300	-0.0025414131	16.400	-0.0022174539	16.500	-0.0019353169
16.600	-0.0016895330	16.700	-0.0014753570	16.800	-0.0012886730
16.900	-0.0011259069	17.000	-0.0009839537	17.100	-0.0008601167
17.200	-0.0007520506	17.300	-0.0006577180	17.400	-0.0005753486
17.500	-0.0005034049	17.600	-0.0004405507	17.700	-0.0003856237
17.800	-0.0003376113	17.900	-0.0002956310	18.000	-0.0002589135
18.100	-0.0002267889	18.200	-0.0001986746	18.300	-0.0001740642
18.400	-0.0001525171	18.500	-0.0001336488	18.600	-0.0001171231
18.700	-0.0001026453	18.800	-0.0000899576	18.900	-0.0000788352
19.000	-0.0000690828	19.100	-0.0000605308	19.200	-0.0000530317
19.300	-0.0000464562	19.400	-0.0000406903	19.500	-0.0000356331
19.600	-0.0000311960	19.700	-0.0000273018	19.800	-0.0000238837
19.900	-0.0000208845	20.000	-0.0000182541	20.100	-0.0000159484
20.200	-0.0000139280	20.300	-0.0000121570	20.400	-0.0000106040
20.500	-0.0000092416	20.600	-0.0000080467	20.700	-0.0000070001
20.800	-0.0000060848	20.900	-0.0000052857	21.000	-0.0000045885
21.100	-0.0000039799	21.200	-0.0000034480	21.300	-0.0000029828
21.400	-0.0000025762	21.500	-0.0000022220	21.600	-0.0000019148
21.700	-0.0000016494	21.800	-0.0000014202	21.900	-0.0000012218
22.000	-0.0000010492				

Appendix F

Computer codes

F.1 Code for Dispersion Relation

```
/* This program calculates the Threshold anomalies of the potential
by using 3 lines. The user inputs the values from the keyboard and
the output is saved to file dispersion.dat
Date: 5-08-2009*/

#include<stdio.h>
#include<math.h>

int main(void){
float W0, W1, D, D1, Dm, E, Ea, Eb, Ec, Em, h;
float ea, eb, e1b, e1c, e2c, e2m, DV, V;
int i;

FILE *output_file;

printf("\ Dose\ tin\ timi\ tou\ Ea:\n");
scanf("%f" ,&Ea);
printf("Dose\ tin\ timi\ tou\ Eb:\n");
scanf("%f" ,&Eb);
printf("Dose\ tin\ timi\ tou\ Ec:\n");
scanf("%f" ,&Ec);
printf("Dose\ tin\ timi\ tou\ Em:\n");
scanf("%f" ,&Em);
printf("Dose\ tin\ timi\ tou\ W0:\n");
scanf("%f" ,&W0);
printf("Dose\ tin\ timi\ tou\ W1:\n");
scanf("%f" ,&W1);

D=Eb-Ea;
```

```
D1=Ec-Eb;
Dm=Em-Ec;
h=(D1/Dm);

output_file=fopen("dispersion.dat", "w");

for(i=0;i<1000;i++){
E=0.005*i;
ea=(0.005*i-Ea)/D;
eb=(0.005*i-Eb)/D;
e1b=(0.005*i-Eb)/D1;
e1c=(0.005*i-Ec)/D1;
e2c=(0.005*i-Ec)/Dm;
e2m=(0.005*i-Em)/Dm;

DV=-(W0*(ea*log(fabs(ea))-eb*log(fabs(eb)))+
    (W1-W0)*(e1b*log(fabs(e1b))-e1c*log(fabs(e1c)))-
    W1*(e2c*log(fabs(e2c))-e2m*log(fabs(e2m)))+
    W1*(h*log(h)-(h+1)*log(h+1)))/3.14;
V=DV+1.7;

fprintf(output_file, "%8.3f  %f\n",E,V);
}

printf("Ta dedomena einai sto arxeio dispersion.dat\n");
return 0;
}
```

F.2 Codes for generating the imaginary potential

Change x:

```
#include<stdio.h>
#include<math.h>

int main(void){
float x0, x1, x2, x3, y0, y1, y2, y3, xmin, xmax;
float a1, a2, a3, b1, b2, b3;
float Y1, Y2, Y3;
float E, i, j, step, step_x, step_num;
int file_index;

FILE *output_file;
char filename[20];
```

```
printf("      x1,y1\n");
printf("      /'.\n");
printf("     /   '.\n");
printf("    /      '.\n");
printf("   /         '.\n");
printf("  /            ''''''''''''''''''''''''''''''''''''''''''''''''''''\n");
printf("x0,y0         x2,y2                                              x3,y3\n");

printf(" Dose tin timi tou x0:\n");
scanf("%f" ,&x0);
printf("Dose tin timi tou xmin:\n");
scanf("%f" ,&xmin);
printf("Dose tin timi tou xmax:\n");
scanf("%f" ,&xmax);
printf("Dose tin timi tou x2:\n");
scanf("%f" ,&x2);
printf("Dose tin timi tou x3:\n");
scanf("%f" ,&x3);
printf("Dose tin timi tou y0:\n");
scanf("%f" ,&y0);
printf("Dose tin timi tou y1:\n");
scanf("%f" ,&y1);
printf("Dose tin timi tou y2:\n");
scanf("%f" ,&y2);
printf("Dose tin timi tou y3:\n");
scanf("%f" ,&y3);
printf("Dose tin timi tou step_x:\n");
scanf("%f" ,&step_x);

step=0.05;

step_num=(xmax-xmin)/step_x+1;
printf("The number of steps_x is %8.0f \n",step_num);

a3=(y3-y2)/(x3-x2);
b3=y3-a3*x3;

file_index=0;
for(j=xmin;j<xmax;j=j+step_x){
        file_index=file_index+1;
        sprintf(filename, "file%d.txt", file_index);
        //printf("%s\n",filename);
        output_file=fopen(filename, "w");
        x1=j;
```

```
        a1=(y1-y0)/(x1-x0);
        a2=(y2-y1)/(x2-x1);
        b1=y1-a1*x1;
        b2=y2-a2*x2;

        for(i=x0;i<x1;i=i+step){
                E=i;
                Y1=a1*i+b1;
                fprintf(output_file, "%8.3f %8.3f \n",E,Y1);
        }

        for(i=x1;i<x2-step_x;i=i+step){
                E=i;
                Y2=a2*i+b2;
                fprintf(output_file, "%8.3f %8.3f \n",E,Y2);
        }

        for(i=x2;i<x3;i=i+step){
                E=i;
                Y3=a3*i+b3;
                fprintf(output_file, "%8.3f %8.3f \n",E,Y3);
        }
fclose(output_file);
}

printf("Ta dedomena einai sta arxeia file___.txt\n");
return 0;
}
```

Change y:

```
#include<stdio.h>
#include<math.h>

int main(void){
float x0, x1, x2, x3, y0, y1, y2, y3, ymin, ymax;
float a1, a2, a3, b1, b2, b3;
float Y1, Y2, Y3;
float E, i, j, step, step_y, step_num;
int file_index;

FILE *output_file;
char filename[20];

printf("       x1,y1\n");
printf("       /'.\n");
```

```
printf("      /   '.\n");
printf("     /       '.\n");
printf("    /         '.\n");
printf("   /           ````````````````````````````````````````\n");
printf("x0,y0         x2,y2                                    x3,y3\n");

printf(" Dose tin timi tou x0:\n");
scanf("%f" ,&x0);
printf("Dose tin timi tou x1:\n");
scanf("%f" ,&x1);
printf("Dose tin timi tou x2:\n");
scanf("%f" ,&x2);
printf("Dose tin timi tou x3:\n");
scanf("%f" ,&x3);
printf("Dose tin timi tou y0:\n");
scanf("%f" ,&y0);
printf("Dose tin timi tou y2:\n");
scanf("%f" ,&y2);
printf("Dose tin timi tou y3:\n");
scanf("%f" ,&y3);
printf("Dose tin timi tou ymin:\n");
scanf("%f" ,&ymin);
printf("Dose tin timi tou ymax:\n");
scanf("%f" ,&ymax);
printf("Dose tin timi tou step_y:\n");
scanf("%f" ,&step_y);

step=0.05;

step_num=((ymax-ymin)/step_y+1);
printf("The number of steps_y is: %8.0f \n",step_num);

a3=(y3-y2)/(x3-x2);
b3=y3-a3*x3;

file_index=0;
for(j=ymin;j<ymax;j=j+step_y){
        file_index=file_index+1;
        sprintf(filename, "file%d.txt", file_index);
        //printf("%s\n",filename);
        output_file=fopen(filename, "w");
        y1=j;
        a1=(y1-y0)/(x1-x0);
        a2=(y2-y1)/(x2-x1);
        b1=y1-a1*x1;
```

```
        b2=y2-a2*x2;

        for(i=x0;i<x1;i=i+step){
                E=i;
                Y1=a1*i+b1;
                fprintf(output_file, "%8.3f %8.3f \n",E,Y1);
        }

        for(i=x1;i<x2-step;i=i+step){
                E=i;
                Y2=a2*i+b2;
                fprintf(output_file, "%8.3f %8.3f \n",E,Y2);
        }

        for(i=x2;i<x3;i=i+step){
                E=i;
                Y3=a3*i+b3;
                fprintf(output_file, "%8.3f %8.3f \n",E,Y3);
        }
fclose(output_file);
}

printf("Ta dedomena einai sta arxeia file___.txt\n");
return 0;
}
```